UNIVERSITY OF SOUTHAMPTON

FACULTY OF PHYSICAL AND APPLIED SCIENCE

Department of Electronics and Computer Science

Wireless Power Supply for Ambient Assisted Living

by

Yi Li

A thesis submitted in partial fulfilment for the degree of Doctor of Philosophy

February 2015

UNIVERSITY OF SOUTHAMPTON

ABSTRACT

FACULTY OF PHYSICAL AND APPLIED SCIENCE

Discipline (underlined)

Thesis for the degree of Doctor of Philosophy

Wireless Power Supply for Ambient Assisted Living

Yi Li

This thesis focuses on the development of the wireless applications for Ambient Assisted Living (AAL) system, the energy harvesting technique for powering the passive sensors in the building environment, and the flexible screen printed coils for Wireless Power Transfer (WPT) system to provide the power for a body-area sensor network in an AAL system. The AAL provides safe environments around assisted peoples and help them maintain independent living. The applications in AAL include the fixed monitor sensor in building environment and the wearable sensor on users body area. For supplying power for the applications of AAL wireless power supply provides the power without cables while offers a more environmentally friendly solution. Compared with energy harvesting technology, WPT is capable of supplying more power without increasing the size of the device. In this work, a solar powered PIR sensor demonstrates that the energy harvesting technique for a passive sensor application for the fixed monitor sensor in building environment, which can work for up to 16 hours without ambient energy input. For the on-body area application, the flexible coils are employed in the WPT system because of the comfort requirement. The coils are printed on 65/35 polyester/cotton textile with a Fabink-UV-IF1 interface layer coating. The interface layer provides a relatively flat and smooth surface to prevent the permeation of the conductive paste into the textile and allows the printing of finer profile coils, and the flexibility and breathability of textile can be remained. The measured inductances of the printed flexible coils are 3.9 μH for single layer. The design of the printed coil minimises the coil's parasitic capacitance, which is less than 25 pF, and consequently increase the self-resonant frequency of the printed coil. A 5 V 1.51 W DC output has been achieved by a wireless power transfer system using the printed flexible coils with Qi standard circuitry; a DC-DC efficiency of 38% has been measured. It has been compared with the system employed with Qi standard wound copper coils which has the recorded 52% DC-DC efficiency.

Acknowledgements

I would like to thank Prof. Steve Beeby and Dr Neil Grabham for all the guidance and support they have kindly given me over the course of my PhD. This thesis would never have been possible without all the work they put in to, include teaching me how to do a research and write professionally. I would also like to thank Dr John Tudor for his help and advice.

Thanks to Dr Russel Torah, Dr Dibin Zhu, Dr Kai Yang, and Dr Alex Weddell for their time, and for providing expertise on the chemistry and electronics in this thesis respectively. Thanks also to Fan Pei for assisting in the investigation of wireless EMG system, and thanks to Wenhan Jin for assisting in the fabrication and testing of the curvature-adjustable support.

odical><pages>215</pages><volume>20</volume><numor their kindly help and advice about the general issues of daily life and study, and for their camaraderie. Thanks to fellow students in Bay 4 and 5 for their friendliness and companionship. Thanks also to Zihao, Ahmed, Joseph, Huihui, Nur, Marc, Komolafe, Ivo, Zhuo and everyone else who made the research group an enjoyable place to work.

Thanks to Eric Cooke and David Oakley for offering me the opportunity to be a demonstrator and teaching undergraduates in labs. Thanks to all the technic staff in the labs who made lab equipment keeping work.

I would like to dedicate this thesis to the people closest to me. My gratitude and love to my parents for everything they have done for me, I could never be in UK without their kindly help and support. I am really lucky to have my wife Shuo Liu in my life, and great thanks to her for making me happy.

Contents

List of figures

List of tables

DECLARATION OF AUTHORSHIP

I, Yi Li

declare that the thesis entitled

Wireless Power Supply for Ambient Assisted Living

and the work presented in the thesis are both my own, and have been generated by me as the result of my own original research. I confirm that:

- this work was done wholly or mainly while in candidature for a research degree at this University;
- where any part of this thesis has previously been submitted for a degree or any other qualification at this University or any other institution, this has been clearly stated;
- where I have consulted the published work of others, this is always clearly attributed;
- where I have quoted from the work of others, the source is always given. With the exception of such quotations, this thesis is entirely my own work;
- I have acknowledged all main sources of help;
- where the thesis is based on work done by myself jointly with others, I have made clear exactly what was done by others and what I have contributed myself;
- parts of this work have been published as:
    - Y. Li, N. J. Grabham, S. P. Beeby, and J. Tudor, "Energy harvesting from solar cells under typical illumination conditions in buildings," presented at the Nano Energy 2013, Perugia, IT, 2013.
    - Y. Li, N. J. Grabham, R. N. Torah, M. J. Tudor, and S. P. Beeby, "Screen Printed Flexible Coils for Wearable Wireless Power Transfer Systems," presented at Manufacturing for Printed Electronics, Cambridge, UK, 2014.
    - Y. Li, N. J. Grabham, S. P. Beeby, and M. J. Tudor, "The effect of the type of illumination on the energy harvesting performance of solar cells," Solar Energy, vol. 111, pp. 21-29, 1/ 2015.
    - Y. Li, N. J. Grabham, R. N. Torah, M. J. Tudor, and S. P. Beeby, "Smart Textile Based Flexible Coils for Wireless Inductive Power Transmission," in preparation to submit to IEEE Transactions on Consumer Electronics.

Signed: …………………………………………………………………..

Date:…………………………………………………………………….

Abbreviations

AAL	Ambient Assisted Living
AC	Alternating Current
ADC	Analogue-to-digital converter
AM	Air Mass
CAD	Computer-Aided Drafting
CCT	Colour Temperature
CFL	Compact Fluorescent Lamp
DC	Direct Current
DSSC	Dye-sensitized solar cell
ECG	Electrocardiography
EEG	Electroencephalography
EMF	Electromagnetic field
EMG	Electromyography
EOG	Electrooculography
GUI	Graphical user interface
GSM	Global System for Mobile Communications
HVAC	Heating, Ventilation, and Air Conditioning
IC	Integrated chip
ISR	Interrupt Service Routine
LED	Light-Emitting Diode
LPM	Low Power Mode
MCU	Microcontroller Unit

MPP	Maximum Power Point
MOSFET	Metal-oxide-semiconductor field-effect transistor
PCB	Printed Circuit Board
PIR	Passive Infrared Sensor
PN	P-type and N-type Junction
RF	Radio Frequency
RFID	Radio-frequency identification
RGB	Red, Green and Blue
RX	Receiver
SAR	Specific Absorption Rate
SEM	Scanning Electron Microscope
SRF	Self-resonant Frequency
TX	Transmitter
UoS-IF-UV4	University of Southampton made UV cured interface paste for screen printing
UV	Ultraviolet
WPT	Wireless Power Transfer

List of symbols

A	The area of the cross section of the conductor
a_m	The power density of *m*
D_C	The duty cycle
d	The diameter of the coil
F_m	The driving term for *m*
Δf	The band between two operating frequency
f_{min}	The minimum operating frequency
f_{max}	The maximum operating frequency
f_r	The resonant frequency
I_M	The amplitude of the current
i	The instantaneous current
J	The current density
k_{mn}	The coupling coefficients between *m* and *n*
K_N	The Nagaoka coefficient
L	The inductance
l	The length of the track of the coil
M_{TR}	The mutual inductance between the TX coil and RX coil
N	The turns of the coil
P_{active}	The active mode power consumption
P_{sleep}	The sleep mode power consumption
P	The power
Q	The quality factor

R_{sheet}	The sheet resistivity
r_T	The radius of the TX coil
r_R	The radius of the RX coil
S	The space between the tracks of the coil
S_Z	The spacing between the TX and RX coils
t	The thickness of the layer of the printed coil
U	The energy contained in the coil
V_I	The DC voltage
v	The instantaneous voltage
W	The width of the tracks of the coil
Z	The impedance
α	The lateral misalignment between the TX and RX coils
$\mathit{\Gamma}_m$	The intrinsic decay rate of m
η	The efficiency of the power transmission
δ	The skin depth of the conductor
ε_0	The absolute permittivity
ε_r	The relative permittivity
μ_0	The absolute permeability
μ_r	The relative permeability
ρ	The resistivity of the conductor
ϕ	The initial phase
ω	The angular frequency
ω_m	The resonant angular frequency of m

1 Introduction

1.1 Introduction

This thesis presents a practical investigation of methods of supplying power to sensors in an Ambient Assisted Living (AAL) environment. Both solar cell powered fixed passive sensors in a building environment and Wireless Power Transfer (WPT) techniques for activity monitoring sensors on body are examined. For passive sensors in a building, energy harvesting techniques could provide an environmentally friendly method of supplying power to the system. For on-body area sensors, more power is required by the system than a passive sensor. For user comfort, there are also greater constraints on the size and weight of the system. This work focuses on the use of WPT to supply power to the body area sensors. Screen printing is employed to fabricate the flexible coils for the WPT system because it allows the electronics to be integrated into textiles. The Q-factor of printed coils and coupling factor between coupled printed coils in WPT are examined as key parameters in this work.

1.1.1 Ambient Assisted Living System

In 2013, 15.6% of the total population were aged over 65 in the UK [1], and 40% of them (over five million) require assistance with everyday living [2]. AAL aims to promote independence in old age with the support of advanced technologies that minimise the risks of living alone. In the EU's Ambient Assisted Living Joint Programme (AALJP), £500 million has been invested in AAL system research over six years [3]. This field has been increasingly attracting the attention of academic and commercial research teams.

An AAL system is designed for people who enjoy living independently but require assistance for their daily living. The facilities of an AAL system offer assistance with activities such as eating, bathing, dressing, laundry, housekeeping, and medication. AAL system is an intermediate level caring system for many senior citizens, but it is not an alternative to a nursing home, it provides a cost-effective and reliable option for healthcare in the home.

AAL systems have the capability to gather data from the user, analyse the information about the activity and state of the user, and determine users' wellbeing based on this information. AAL system also supplies context-aware services for healthcare and daily living [4], and is simplified by numerous technological devices and innovations.

1.1.2 Wireless Power Transfer

Wireless Power Transfer (WPT) refers to the transmission of electrical power in space without wired connections [5]. The amount of power transferred will be determined by the consumption of the remote systems. WPT was invented in 1899 by Nikola Tesla [6], who planned to broadcast energy from a central station into the ionosphere to be collected by receivers around the world. WPT received a certain amount of attention within academia at the time, but its implementation was limited because of a lack of resources. Stielau [7] has presented a design methodology for inductive power transfer system with loosely coupling in 2000, this methodology has showed the capability of transferring the power to movable objects across air gaps efficiently. In 2007, a Massachusetts Institute of Technology (MIT) research team demonstrated their latest research: a WPT system that can transfer 60 W over several metres; by using the resonant frequency of the coils [8] this work achieved a remarkable increase of energy efficiency in the link between coupled coils (around 40%). Recently, WPT for charging portable devices has attracted a significant amount of interest in both academic and commercial research.

In this thesis, Wireless Power Transfer is specified as:

> Electrical energy transmission using magnetically coupled coils that have been tuned and operate in a resonant frequency oscillated current, capable of delivering power from a transmitter coil to a receiver coil in a way that is safe for human body [9].

Recently, a range of WPT devices have become commercially available, which are mainly used to change portable devices, such as a mobile phone or an electric toothbrush. Most transfer power by coils fabricated with wound copper or a PCB [10].

1.2 Research Motivation and Aims

An AAL system employs various sensors and devices for its functionality, and these sensors and devices require sufficient power to operate. Four power supply methods for these applications can be considered: wired mains, batteries, energy harvesting and WPT. Using mains powered devices incurs installation costs associated with power supply cables, while battery powered devices require periodic battery changes, which causes pollution, high maintenance costs and may interrupt the service of a device. The energy harvesting technique can provide a certain amount of energy for some applications that employ passive sensors, which avoids the waste of cables and batteries. Periodic maintenance is not required since long lifetimes can be achieved, making energy harvesting an environmentally friendly option.

For fixed passive sensors in a building environment, energy harvesting techniques are widely used. For instance, the energy from ambient environment is sufficient for Passive Infrared (PIR) sensors, which can be used to provide occupational information for a human tracking system. Consequently, the use of energy harvesting techniques in a building environment is investigated. Artificial light is the most common stable ambient energy source in a quiet residential building, and the nature of light sources has changed over time from incandescent sources, through fluorescent lights, with LED lights currently attracting significant interest due to their energy saving properties.

For on-body area applications, the power requirements are greater than building monitoring because active rather than passive sensors are used. The power that energy harvesting provides is limited by the ambient energy sources and the efficiency of the harvester. For instance, in a dark environment, there is almost no output power from a solar cell. The energy harvested by an on-body area kinetic energy harvester is limited by the activity of the user. The relationship between the amount of the energy that harvesters can collect and the size of the devices shows that a harvester capable of powering a body area sensor system would be prohibitively large or heavy. A number of studies [11-13] have focused on making the sensors flexible and wearable to achieve the requirements for comfort, however, if the system is powered by a battery, this is inflexible and bulky, and needs to be replaced or recharged frequently. Consequently, there is novelty in improving the power supply system in terms of its weight and flexibility. A wireless power supply with flexible flat coils could allow the power supply to become fully integrated into clothing. Screen printing is a developed technique in electronics, in which flat coils can be produced. Normally screen printing technique requires a rigid substrate and curing at high temperature (>200 °C). There are many challenges involved in employing this technique in the fabrication of wearable devices to achieve desired results, but it has advantages in terms of the integration of the progress of manufacturing.

The main objective of this research is to construct wireless power supply subsystems for AAL system. In the building environment, a range of different types of solar cells is investigated under different light sources to achieve an optimum power supply solution, and a demonstrator solar-cell-powered PIR sensor tested in a real world application. In the on-body applications of AAL system, a wearable WPT system is built to supply the energy required by active sensors without wires or batteries, and to achieve the requirement of the comfort. As reviewed, the energy harvester, such as printed flexible solar cells, has the limitation on harvested power density. Consequently, for the systems with active sensors, it requires a considerable large area to provide the sufficient power that does not meet the requirement of comfort for wearable applications. The main part of the WPT is the coils of the transmitter and receiver, printing the coils on textiles can make them flexible and wearable, and the printing technique can be integrated into the clothing production process. The transmitter can be integrated into a chair, and the power for the on-body applications can be supplied automatically when the user sits on it.

The aims of this research include:

- Investigation and design of suitable power supply methods for the applications of AAL in a building environment with passive sensors.
- Design and building of flexible printed coils on textiles for the WPT system to supply the power for an on-body AAL application.

1.3 Statement of Novelty

The novelty in this work originates from the investigation of the application and the fabrication method. Firstly, a thorough investigation into the effect of illumination types on the performance of photovoltaic energy harvesting is presented for the first time in this thesis. Secondly, the fabrication of a flexible functional printed coil on a textile for WPT by screen printing is realised for the first time. Fabricating the flexible coils by screen printing on fabric for a WPT is a new research area. Previous related publications involve research either in other methods to provide power for on-body application of AAL, or other techniques to fabricate the coils for different applications. The specific novelty claims in this work are given as follows:

- A detailed analysis of the effect of three illumination types on four models of solar cells.
- A flexible solar cell powered PIR sensor with a radio transceiver.
- An analysis of the curing time for large area screen printing conductive paste.
- Screen printing coils on interface-coated textiles for wireless power transfers.

1.4 Publications arising from this work

Four publications have arisen from this work, three of these are already published, with one further publication awaiting peer review. The published articles are one conference paper, one poster session, and one journal paper. The publications are listed here in chronological order.

- Y. Li, N. J. Grabham, S. P. Beeby, and J. Tudor, "Energy harvesting from solar cells under typical illumination conditions in buildings," presented at the Nano Energy 2013, Perugia, IT, 2013.
- Y. Li, N. J. Grabham, R. N. Torah, M. J. Tudor, and S. P. Beeby, "Screen Printed Flexible Coils for Wearable Wireless Power Transfer Systems," presented at Manufacturing for Printed Electronics, Cambridge, UK, 2014.
- Y. Li, N. J. Grabham, S. P. Beeby, and M. J. Tudor, "The effect of the type of illumination on the energy harvesting performance of solar cells," Solar Energy, vol. 111, pp. 21-29, 1/ 2015.

- Y. Li, N. J. Grabham, R. N. Torah, M. J. Tudor, and S. P. Beeby, "Smart Textile Based Flexible Coils for Wireless Inductive Power Transmission," in preparation to submit to IEEE Transactions on Consumer Electronics.

1.5 Thesis Outline

Chapter 2 presents a literature review of the AAL, with a focus on the power supply for AAL systems, the WPT technique and screen printing fabrication. The current research in these areas provides the background for this thesis.

Chapter 3 describes the design and tests of a demonstrator occupancy detector powered by a commercially available solar cell. This self-powered sensor can be used in the AAL human tracking system.

Chapter 4 explains the theory of the WPT, including the coupled system in general, the coils for WPT and the circuitry for the coils.

Chapter 5 describes the investigation and design of the printed coil.

Chapter 6 presents the results of the experiments on the printed coils and the performance of the WPT system with printed flexible coils. Finally, Chapter 7 concludes this thesis, evaluating the objectives and providing recommendations for further work.

2 Background and Literature Review of Wireless Power Supply

2.1 Introduction

In this chapter, related works on the applications of Ambient Assisted Living (AAL) systems, sensors for AAL applications and power supply technologies for the systems are reviewed in the context of AAL. WPT techniques are reviewed from both research and commercial standards. Finally, the research and development of smart fabrics is reviewed to identify the role that smart fabrics play in WPT applications.

2.2 Ambient Assisted Living

AAL systems can be used to monitor and assist elderly, disabled, or chronically ill individuals in their homes to improve their quality of life and their health outcomes [14]. By helping control healthcare, an AAL system can reduce consumption, maintenance and labour costs [15]. To achieve this, the AAL system comprises sub-systems in the building environment and on the body area as classified in Figure 2-1.

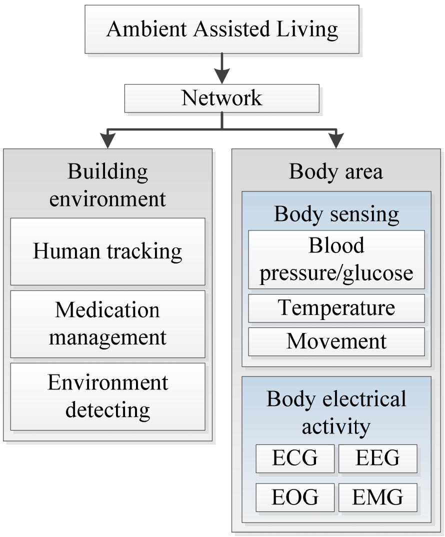

Figure 2-1 Framework of the AAL system

The sub-systems in the building include human tracking, medication management and environment detection. Human tracking is the record of the user's position information, analysis of this information and eventual use of it to determine the state of the user [16]. AAL provides medical management and generation of appointment reminders for the patient [17].

Environment detection collects environmental information, allowing the AAL system to give the user suitable suggestions regarding the weather or activities [4, 18].

The on-body-system monitors the health state of the user and this data can be made available to doctors remotely without intrusion [19], allowing doctors to analyse biometric information either in real-time or long term [20-22]. At the same time, users can process their self-health checks and identify potential health risks by comparing their monitoring data with database and receiving the helps from a remote medical system, the patterns of these health risks could be complicated such as neurodegenerative disease [23] or cancer [24].

With omnidirectional information monitored by the AAL system, it links the elderly person or patient to the doctor who can observe them directly and efficiently, this has the advantage of enabling the issue of medical prescriptions more promptly, as well as the patient being able to receive help quickly. If any emergency situation, such as a fall, occurs, rapid notification is sent out in real time.

Within the realms of technology and ageing, this has resulted in a focus upon the issues facing frail and disabled elderly people living at home by themselves. A range of research projects funded by the European Union between 2009 and 2013 is shown in Table 2-1 [25].

Table 2-1 The AAL projects and the sensors involved

Project name	Application	Sensors involved
ALADDIN	Detection of decline symptoms	Blood pressure sensor Blood glucose sensor
AMICA	Disease management Medical care Early detection of exacerbations	Spirometer Ad-hoc sensor Body temperature sensor
CAPMOUS	Multi-sensor headset for AAL	Electroencephalography (EEG) Electrooculography (EOG) Eye Tracking
eCAALYX	Wearable body sensor	Electrocardiography (ECG)
HELP	Continuous drug delivery	PIR occupancy sensor
HMFM	Medication management	Radio-frequency identification(RFID)
SOFTCARE	Daily activity record	3D-accelerometer

In project ALADDIN, efficient sensors are used to measure the blood pressure and glucose, the monitoring system requires dozens watts of power, since the decline symptoms need to be detected, a long term continued morning is required for months and years. AMICA provides a multidimensional disease management system, body area sensors, i.e. spirometer which to measure the volume of air inspired and expired by the lungs and body temperature sensor are deployed in this system to allow early detection of exacerbations. CAPMOUS focus on the measuring and monitoring on human head, the head mounted sensors are developed and can be used as an input for a human machine interface. The similar electrode is used in project eCAALYX for a wearable ECG, a more convenient dry electrode is developed by Paul*, et al.* [26]. In project HELP, PIR sensors are employed in the automatic continuous drug delivery system, this system can improve the quality of life of Parkinson patients. The medication management system is developed in project HMFM, a haptic and audio user interface enables the management of medication accessing and consuming. The project SOFTCARE employs a set of devises on body area to record daily activities of senior citizen that will help to detect potential problems. These projects show a high demand of different types of sensors for different applications in AAL, these sensors are deployed either in building environment or on body area. The medical professors can give the advises based on the information which collected from the users by employing the sensors, the feedback can be given much quicker and more accurate compare with that based on the regular healthy check.

2.2.1 Building Environment

AAL makes buildings smart and friendly for people, as it provides information such as the weather, environmental temperature and agenda reminders. Human tracking collects the position and state of the elderly person, for instance, a lying down state in a bedroom is normal, but in a kitchen it could mean the person has fallen and is in danger, in addition, other sensors could be employed for complicated situation, such as the accelerometer can measure the changing of speed to determinate that whether one person having a bath (low rate) or falling in a bathroom (high rate). Medication management allows consistent ordering of medications even if they have been forgotten to be taken or over-used.

To operate the system, controllers integrating the communication model and sensors provide internal environmental control [27], for instance controlling the temperature by turning the heating on or off with local controls, limiting carbon dioxide levels and humidity using fans and dampers, mixing in fresh air, and even opening or closing doors and windows. By measuring the lighting levels in certain zones, such as near a window, they can adjust the brightness by controlling light units or blinds. Inferred information about an activity and the state of activities is used in the human tracking system, it requires a reliable communication model, and all the PIR occupancy sensors are connected for analysing human motion information. The medication management monitors the quantity of drug by weight, the location by RFID, and then confirms the prescription with the doctor.

Therefore, sensors are installed in buildings to collect information and to improve occupant comfort in reconfigured spaces; various sensors [28] are classified in Figure 2-2 .

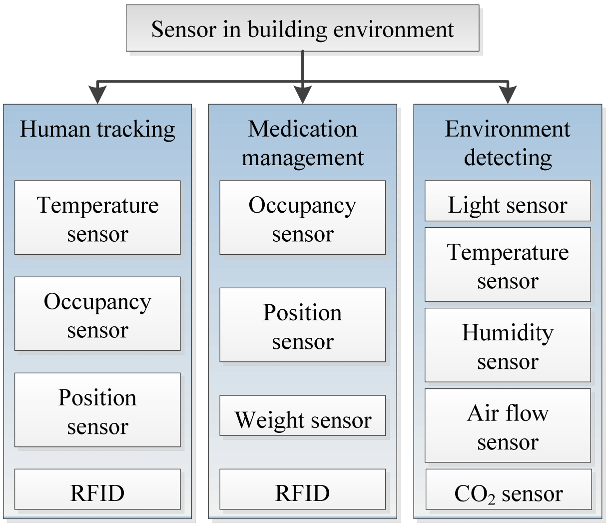

Figure 2-2 Sensors in the building environment

Jara*, et al.* [3] presented a methodology to give healthcare support at patients' homes. It provides a set of services including home automation, security, ambient intelligence and tele-medicine that can operate autonomously. Temperature, occupancy and position sensors are used in the system and the system is flexible in that the end user can define a solution fixed to their needs. These sensors and devices are commonly used in an AAL sub-system in the building environment, which include wired and wireless ones as shown in Figure 2-3 with the description listed in Table 2-2.

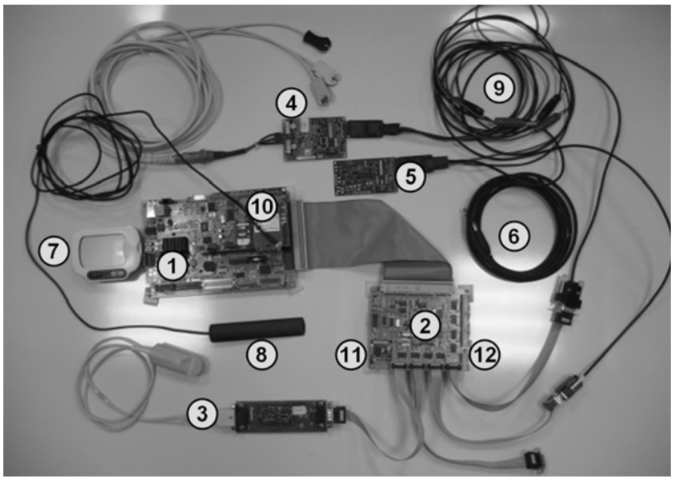

Figure 2-3 The architecture elements of an AAL sub-system for telemedicine, taken from [3]

Table 2-2 The devices used in an AAL sub-system [3]

Number	Description
1	Control unit with GPRS and Ethernet communication interfaces
2	Medical extension with serial and Bluetooth communication interfaces
3	Test Kit Mini Pulse-meter OEM board. EG0352 of Medlab
4	Test Kit EKG OEM board, EG01000 of Medlab
5	Test Kit Temperature OEM EG00700 (2 channel YSI 401 input) of Medlab
6	YSI Temperature Sensor 401 of Medlab for core and peripheral temperature
7	Bluetooth glucometer of OMRON
8	GPRS antenna
9	Wires which need to connected to power supply
10	GPRS modem
11	Bluetooth modem
12	Serial ports

It can be seen that the wireless communication interfaces of GPRS and Bluetooth and the wired communication interfaces of Ethernet and Serial are used which require batteries and mains as power supplies with considerable volume and cables. The user experience has not been considered in this research, relatively, a wireless system with same capability may be considerate for senior citizens.

Jiang*, et al.* [29] presented a PIR sensor system used for a human tracking system. It employs 16 sensors to provide plenty of information for a 9 × 9 m room, mains power, adaptors, and batteries are required to supply the power for these PIR sensors. Peter*, et al.* [30] presented an assisted living system related to the effects on the behaviour of users in a home environment. The behaviour of the user is investigated by human tracking, and then combined with contextual information such as lighting and ambient temperature to provide suitable suggestions. The system delivers a connection between the users and their families using advanced electronic communication based on the Internet via an easy to use interface whose accessibility is appreciated by senior citizens, alternative methods which could be more convenient for the user who has no access to the Internet can be also involved in the project. It shows the structure of an AAL system and the main support it provides. Although feedback from users about the comfort level of this system is not discussed in the paper, general trends in the developments of consumer electronics are towards making these systems light, wireless and unobtrusive.

A wide range of sensors is available to perform these measurements for AAL applications from many manufacturers. Honeywell [31] produces a wide range of wired devices catalogued in several systems, such as lighting and HVAC with control via bus, HTTP or other Ethernet LAN protocol. Another company, Johnson Controls [48], produces a wide range of sensors including: humidity; temperature; pressure; carbon dioxide; and occupancy sensors. The WRS series Many-to-One Wireless sensing system allows multiple WRS sensors to communicate wirelessly with a Metasys network through a single receiver.

2.2.2 Body Area Sensors and Network

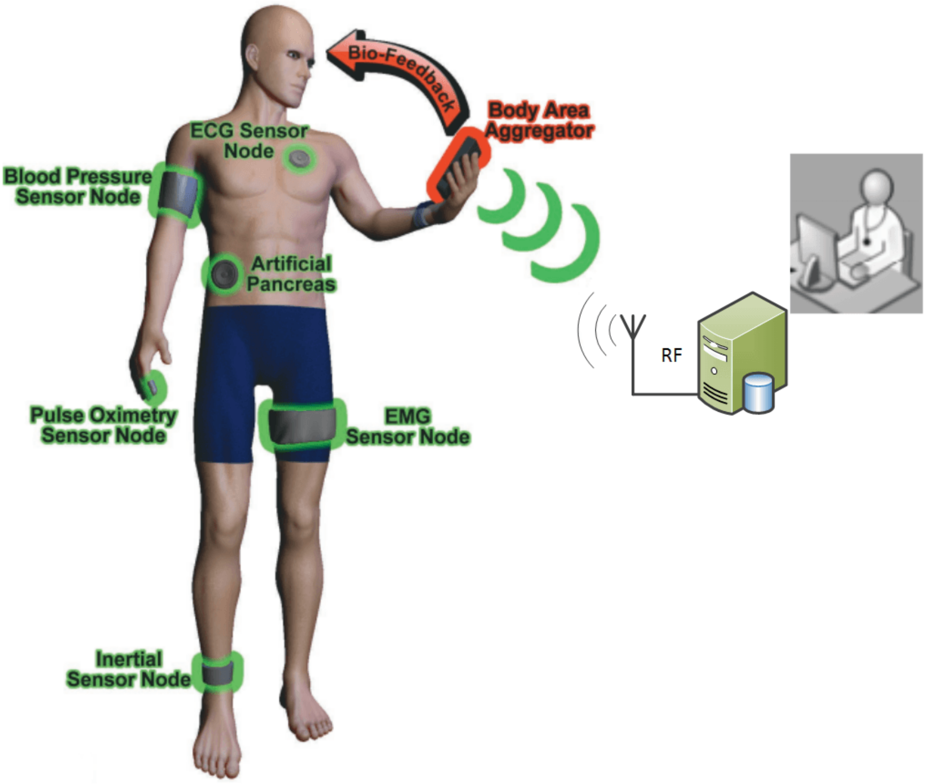

Figure 2-4 Body area sensor and network, taken from [32]

As shown in Figure 2-4, an on-body sensor network of health monitoring systems for detecting health risks comprises sensors, electronics for processing the sensor output, and a wireless transceiver for radio transmission [32, 33]. The system allows remote monitoring of biological parameters, there parameters are heart rate, respiration, blood pressure, blood glucose level, body temperature, body movement activity, and electrical activity from the brain, eyes and other muscles.

Table 2-3 Articles about different types of body area sensors deployed in various applications

Author	Application	Sensor	Useful information
Calvert, *et al.* [34]	Respiration Monitoring	Strain	Effect of Deformations
Bielska, *et al.* [35]	Temperature Monitoring	Thermistor	30-42 °C Detection Range
Jie, *et al.* [36]	Movement Monitoring	Radio Frequency (RF) Antenna	Wearable Antenna in Monitoring
Paul, *et al.* [26]	Human-Computer Interface	EOG, EMG	Screen Printing Fabrication
Yuce [37]	Healthcare Monitoring	ECG	Noise in ECG Signal with Wearable Sensor

The research of on-body sensor networks is presented by many articles relevant to printed health monitoring applications [25, 33-36] are listed in Table 2-3. These sensors are classified into two main sections; The body state, such as blood pressure level and glucose level, body temperature state, and body activity or movement state; And the electrical potential detected from tissues including ECG measuring the electrical activity of the heart, EEG measuring voltage within the neurons of the brain, EOG measuring the resting potential of the retina for recording eye movements, and electromyography (EMG) measuring the electrical potential generated by muscle cells [33]. It shows that these sensors are widely used for on-body area monitoring applications, and the design of the power supply for the entire system should consider the requirements of these sensors. These active monitoring systems are generally power-hungry, an average consumption level is approximately 500 mW, which includes ECG and the circuitry for the signal processing [38].

Rius, *et al.*, [39] presented an on-body sensor strategy for integration on textiles, and it focuses on the use of sheets of conducting layers instead of tracks, making the on-body sensors flexible and comfortable. It shows the screen printing technique for e-textile manufacture that will be discussed in section 2.5. It still employs a battery to power the sensor, and the battery increases the weight of the entire system and requires frequent recharging.

2.2.3 Energy Requirements

A large number of sensors within the network require a power supply, for instance, Baheti and Garudadri [40] presented a system with 3D accelerometers to monitor heart rate and blood pressure using 5 mW for the low power design of the entire system. Yoo, *et al.* [11] presented a wearable body sensor network using a total of 5.2 mW by using the lowest power consumption components in the market, and employing an advanced design ECG analogue signal processor. Ng*, et al.* [41] presented a system requiring less than 45 mW for an electrode array with 1000 passive electrodes, which is a massive array for a retinal prosthesis in original research, relatively, this power is plenty for the passive electrodes of monitoring on a body area. Passive sensors, like passive electrodes and PIRs, consume an ignorable low power comparing with their measuring system, the power the system with passive sensors consumed is depended on the measuring circuit which extracts the single from these passive sensors [42], Rahimi*, et al.* [43] presented a high efficiency circuit for common passive sensor which consumes power approximately of 1 μW. Consequently, energy harvesting technology can be employed to achieve a self-powered system and make such system environmentally friendly which will be discussed in Section 2.3.2.

A ZigBee network requires on average 10 mW for the wireless communication in a typical body-area-network application, which generally has about 20 nodes deployed over the body and has an average of 50 kbps data rate communication between the nodes [44, 45]. The Berkeley Wireless Research Centre developed a System-on-Chip based sensor node with a radio transmitter that uses less than 400 μW for each node [46]. For a typical active sensor with the network to monitor on a body area, the average power it consumes is approximately 100 mW [47]. Comparing with active sensors and communication networks, the passive sensors used in building environments for an AAL system consume much less power in the scale of micro watt [48].

By reducing the duty cycle of active sensors and the communication for long term monitoring applications, the entire power requirement can be limited [44]. The duty cycle depends on the sampling rate and the wake up time the circuit takes, so a 20 Hz sampling rate for monitoring normal human activity is presented which gives a reliable result [49] that can keep the duty cycle at a low level. For example, with a supply voltage of 2.0 V, a microcontroller with a radio transceiver ez430-rf2500 will draw 2.3 μA when sleeping, and around 22 mA when active and communicating [50]. The maximum current of the system required in active mode is around 10,000 times higher than when it is sleeping. If the sleeping time is around 100 times longer than the active mode time and it samples the data every 0.05s in an entire day, it works at a 1% duty cycle, and the entire system consumes an average power of approximately 3 mW. The proportion of energy saved by using duty-cycled operation is given by equation 2.1 [51].

$$\text{Energy Reduction} = (1 - D_C)\left(1 - \frac{P_{sleep}}{P_{active}}\right) \qquad (2.1)$$

where D_C is the proportion of the duty cycle, P_{sleep} is the power consumption when the system operates in a sleep mode that consumes the lowest power and can wake up immediately, and P_{active} is the power consumption when the system operates in the active mode - ‘on duty’ in this context. Overall, the average power consumed by a typically sensor network deployed in an AAL system can be limited into a range from 10 mW to 1 W in building environments or on body area, it is strongly relative with applications.

2.3 Power Supply

All the sensors and networks, either in the building environment or the on-body area, need a power supply for operation. The power consumption can be used as a guideline for choosing the method of power supply as a certain quantity of energy can supply a passive sensor for months but only several hours for an active sensor. A system which consuming an average power less than 50 mW can be supplied by one or few dry cell batteries without battery replacement or recharging for few month, or can be supplied by an energy harvester with limited size and weight while without maintenance for its lifetime. Relatively, a system which consuming an average power in the range of 50 mW to 5 W can be supplied by WPT or wired power line to avoid frequently battery changing or maintenance, while a system which consuming an average power over 5 W should be supplied by wired power line to ensure that the system has a stable power supply. The different types of power supply used in AAL systems will be discussed in the following sections.

2.3.1 Wired and Battery Power Supplies

Many systems employ batteries or wired mains to supply power for the sensors and networks in a building environment [3, 15, 52] or the on-body area [53-55] because of their simplicity of use. Wired sensors have stable power and signal lines, but the high cost of wiring, along with the support infrastructure, are major issues for their use. In a commercial building, the average cost of installing wiring for a single node is estimated at least £160 [56]. Relatively, a wireless sensor has a big advantage in deployment, as that one sensor can be installed anywhere without having to consider the signal line and power supply.

A range of wireless devices use batteries to power the sensor and on-board radio, but the lifetime of these devices is limited by the amount of energy that the batteries can store within the packaging volume of the application. Consequently, batteries need monitoring in case they run down, and then they need to be replaced or charged to keep the system running, necessitating on-going maintenance. Normally this system needs to be changed every few months. This decreases the value of wireless sensing solutions and limits their use, particularly for sensors which are power-hungry or for applications using high data rates, such as real-time monitoring and analysing [55], in these cases, the interruption caused by the runing down of batteries is not acceptable.

For a network, the current systems either requires quantities of copper for signalling and power lines for wired sensors, or it will generate many waste batteries from the wireless sensors powered by batteries. Furthermore, the cost of maintenance is extremely high and may interrupt the applications, which increases the cost and is noisy. Senior users easily forget to exchange or recharge the battery in their sensors, and then this causes a monitoring fault. It is inconsiderate to force a user to do things they may forget, something which is at odds with the usual philosophy of AAL systems.

2.3.2 Energy Harvesting Power Supplies

Energy harvesting technology is a better option for low power systems than wired mains or batteries in a certain environment, for instant, in the case that a wireless smart sensor network deployed in a ferry that a constant vibratory energy from the engine can be harvested to supply the power for the entire network without the installation of the power line or batteries [57]. On the other hand, in an environment without sufficient ambient energy, such as a dark and quite room, the energy harvester has the limitation on the deployment. The alternative use of harvesters for mains powered devices avoids the installation costs associated with power supply cables. There is a considerable amount of energy been wasted during the processes of voltage conversion, which is in the transformer or the DC to DC voltage regulator[58], that a designed energy harvesting power management can avoid such energy wastes by providing the electric energy in the required form. Energy harvesters offer a more environmentally friendly solution for battery-powered installations and do not need periodic replacement since long lifetimes can be achieved. Dokania*, et al.* [59] compared the lifetime of a radio transceiver, which is usually the main power consuming part of the system, to body area networks powered by battery and energy harvesting and showed that an energy harvesting power supply is a better option for a low power system.

Toit [60] reviewed the level of energy harvested from various sources, including an axial flow generator in water or air, various types of vibration generator, thermo-electric from PN junctions and solar cells in various lighting conditions. The outdoor solar cell has the highest output power density in the reviewed harvesters, followed by the axial flow generator, they have strict environment conditions such as the direct sun or a minimal flow speed to achieve this high output power density. The energy harvested from vibrations by piezoelectric harvesters has certain conditions such as a self-resonant frequency is required to be met, and a typical vibration source generates noise within a zone. The thermoelectric energy harvester requires a face with difference of temperature around it. Paradiso [61] has reviewed the energy harvesting researches by 2015, the review has detailed performances of different types of energy harvesters considering about each working condition and environment as listed in Table 2-4.

Table 2-4 Energy-harvesting opportunities and demonstrated capabilities [61]

Energy Source	Performance	Notes
Ambient Radio Frequency	$< 1\ \mu W/cm^2$	Unless near a transmitter.
Ambient Light	$100\ mW/cm^2$ (directed toward bright sun) $100\ \mu W/cm^2$ (illuminated office)	Common polycrystalline solar cells are 16%-17% efficient, while standard monocrystalline cells approach 20%. Although the numbers at left could vary widely with a given environment's light level, they're typical for the garden-variety solar cell Radio Shack sells.
Thermoelectric	$60\ \mu W/cm^2$	Quoted for a Thermo Life generator at $\Delta T = 5$ °C; typical thermoelectric generators ≤ 1 efficient for $\Delta T <$ 40 °C.
Vibrational Micro-generators	$4\ \mu W/cm^3$ (human motion – Hz) $800\ \mu W/cm^3$ (machines – kHz)	Predictions for 1 cm3 generators. Highly dependent on excitation, and larger structures can achieve higher power densities.
Ambient Airflow	$1\ mW/cm^2$	Demonstrated in microelectromechanical turbine at 30 liters/min.
Push Buttons	50 µJ/N	Quoted at 3 V DC for the MIT Media Lab Device.
Hand Generators	30 W/kg	Quoted for Nissho Engineering's Tug Power.
Heel Strike	7 W potentially available (1 cm deflection at 70 kg per 1 Hz walk)	Demonstrated systems: 800 mW with dielectric elastomer heel, 250-700 mW with hydraulic piezoelectric actuator shoes, 10 mW with piezoelectric insole.

In the building environment, Matiko, *et al.* [62] reviewed the potential energy sources available in both residential and commercial buildings, and conclude that light is the most practical energy harvesting source due to its widespread availability. The luminous intensity of illumination systems within a building is designed or adjusted to achieve a satisfactory level for the occupants; the illumination level is commonly measured in lux. Lux levels represent a measure of light luminous intensity as perceived by the human eye. In office environments, the lux level at a desktop should be around 300 to 500 lx, this level allows the human eye to work in a comfortable and relaxed state for typical office-based tasks [63].

In buildings, the illumination system accounts for approximately 9% of residential electricity use and 40% of commercial electricity use [64]. Incandescent light bulbs waste over 90% of their input energy as heat [65], by upgrading incandescent lamps to CFL or LED, an average 70% or 85%, respectively, of the previous energy consumption can be saved [66], therefore, in many situations lighting installations are being upgraded from incandescent lamps to save both energy and money.

Many different solar cell technologies have been developed [67] and optimised for energy harvesting from either natural or artificial light [68]. One of the parameters influencing the output power density of a solar cell is the spectral composition of incidental light, therefore, for example, the output power density of an outdoor type solar cell can decrease dramatically when the light source is changed from natural to artificial due to the differing spectra. Energy harvesting powered devices will not operate if the solar cell cannot harvest sufficient energy [69], which may occur if the solar cell used is optimised for a different light source.

Since the spectral distribution of natural light changes greatly as the path length of solar light radiation through the atmosphere changes, the Air Mass (AM) is represented relative to the local zenith (normal) path length to the sun at sea level, as path lengths vary with latitude and time of day. The standard AM-1.5 test conditions (solar elevation angle of 41.8 °) represents a widely accepted consensus reference condition for the evaluation of solar cells.

Missaoui, *et al.* [70] presented an application example of an integrated solar cell energy management system in a real-time simulation that yields various benefits such as maximising user comfort, minimising energy costs, and reducing unnecessary pollution by employing a human tracking system. This simulation evaluates the applications powered by energy harvesting technology.

EnOcean provides a wireless standard and it has a multi-company alliance develops on its interchangeable self-powered wireless monitoring and control systems for sustainable buildings under this standard [71]. The use of energy harvesting brings benefits such as cost savings in installation, maintenance, renovation, operation and energy use. For a single building that has 55 floors and 4,200 lights, using self-powered devices can save 42,000 batteries over 25 years [72].

On the body area, Masotti, *et al.* [73] designed a jacket for collecting GSM or WiFi power from a communication network that can supply power for passive sensors, a maximum 1.9 mW of power can be collected from a 100 mW 900 MHz radio-frequency source at a distance of 30 cm by using two of 49 cm^2 patch antennas , however, it increases the burden of the base station which is designed for communication. Fan, *et al.* [74] invented a SoC sensor node which harvests hybrid energy from RF and thermoelectric power sources, this SoC has four sensing channels to measure ECG, EMG, and EEG signals. This sensor node requires a 600 mV boost voltage to initialise the energy harvesting function which means an additional initialisation progress is required to be done by the user.

2.3.3 Wireless Power Transfer

Wireless Power Transfer (WPT) aims to supply sufficient power for high power consumption applications without physical electrical connections compared to a wired power supply or the waste compared with batteries, different methodologies of WPT are discussed in this section, and the distance the WPT system can transfer depends on the methodology and also the design for different applications, while a typically requirement of an AAL application is in centimetre scale [75]. It does exactly the same job which a power cable or a battery does in the applications of the AAL system in the building or on the body area, but improves the convenience and user-friendliness of portable electronic products [76] without the issues of the previous two. Wireless power can supply the system directly or charge the energy storage for continued operation of the system [77] when wireless power is temporarily unavailable.

Wireless power supply has seen an increasing number of research studies [78] developing over issues such as inefficiencies and lack of control, which may cause safety issues. Several researchers have recently presented solutions to the challenges such as the high power consumptions on circuity for high power and high frequency switching, the large physical volume of circuits and coils, and the low efficiency of conversions between AC and DC, which have delayed the introduction of efficient wireless power for mass adoption. The different technologies are pushed toward the solutions as shown in Figure 2-5.

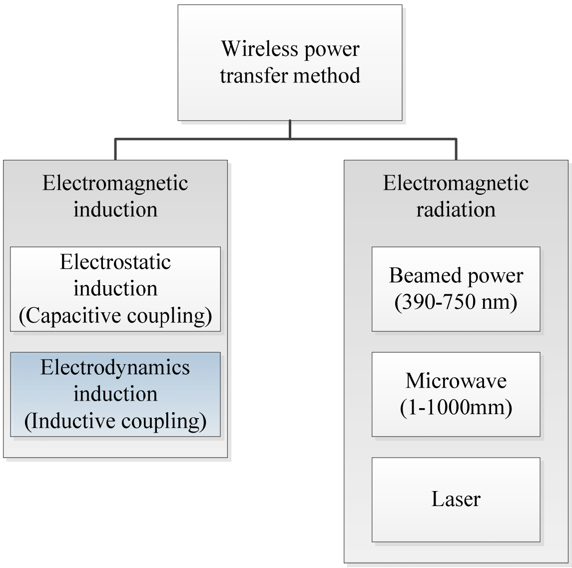

Figure 2-5 Wireless power supply methodology

These methods are classified into two main sections, electromagnetic induction methods build a coupled link between the transmitter (TX) and the receiver (RX); the use of electromagnetic radiation requires that the receiver is exposed to the emissive energy from the transmitter. The electromagnetic radiation in wavelengths from 1 to 1000 mm causes unacceptable energy loss from omnidirectional radiation. The electromagnetic radiation in wavelengths from 390 to 750 nm can deliver high density energy with directional radiation, such as laser, but it requires an unimpeded route, which means the energy will be received by unexpected item that interrupting the route and causing a safety issue. Consequently, the electromagnetic radiation is unsuitable to supply the power for the wearable applications in an AAL system.

The capacitive coupling method relies on a high voltage electrical field, the high voltage requires a strong isolation between the human body and such devices, a fault on the isolation of the voltage over 50 V can cause serious safety problems to human, i.e. electric shock, and increase the potential fire risk, relatively, a low voltage power (<50 V [79]) is commonly considered as a safe electric power. This fact of a high voltage employed in the capacitive coupling power transfer increases the risk to users, so the isolation on the devices, which employing the capacitive coupling power transfer, is required to be examined carefully. The capacitive coupling system is very limited by coupling distance and geometric size, Jingook and Bien [80] presented a capacitive coupling wireless power transfer system employing a pair of 2000 cm^2 plates, which is larger than a typical area on human back, to achieve a maximum 160 pF of coupling capacitance without the capability of transferred power mentioned, the maximum transfer distance is limited to 15 mm. Kline*, et al.* [81] presented a capacitive coupled charging system with 3.7 W of output power with 60 V oscillating electrical field between plates, but the transfer distance is limited to 0.13 mm. The coupling capacitance is strongly relative with coupling distance and geometric size, which means a frequently changed transfer distance and limited plate size, which is commonly occurred in the wearable applications, increase the variation on the coupling capacitance, and then rise the challenge on the driver circuitry to match the coupling capacitance. Capacitive coupling wireless power transfer has the challenges on the isolation, coupling distance, geometric size and driver circuitry, these factors cause the limitation of the development on this mothed, especially comparing with the inductive coupling wireless power transfer that has the advantages on these factors.

Electrodynamics induction relies on a high frequency magnetic field that is the safest method to transfer power which is why it is deployed in many research studies of implanted medical applications [82-84]. It has the advantages of small size, light weight and being comfortable to wear. Therefore, the inductive coupling method is selected for WPT in this thesis. Inductive wireless power transmission is a common near field power coupling technique [85]. The system has two coils resonant in a magnetic field which then transfers the power. The distance between the coils essentially determines their minimum geometric size, because with respect to the efficiency of the power transfer, the coupling coefficient between the coils has to be sufficiently high. If the coupling is too low, a higher current in the primary coil has to be used to provide the same output from the secondary coil, leading to more power being wasted in the primary coil due to copper (I^2R) losses.

Different methods of wireless power transfer can delivery power in different distances, a general illustration of the wireless transferred power against the distance transferred by different types of wireless power transfer method have been shown in Figure 2-6.

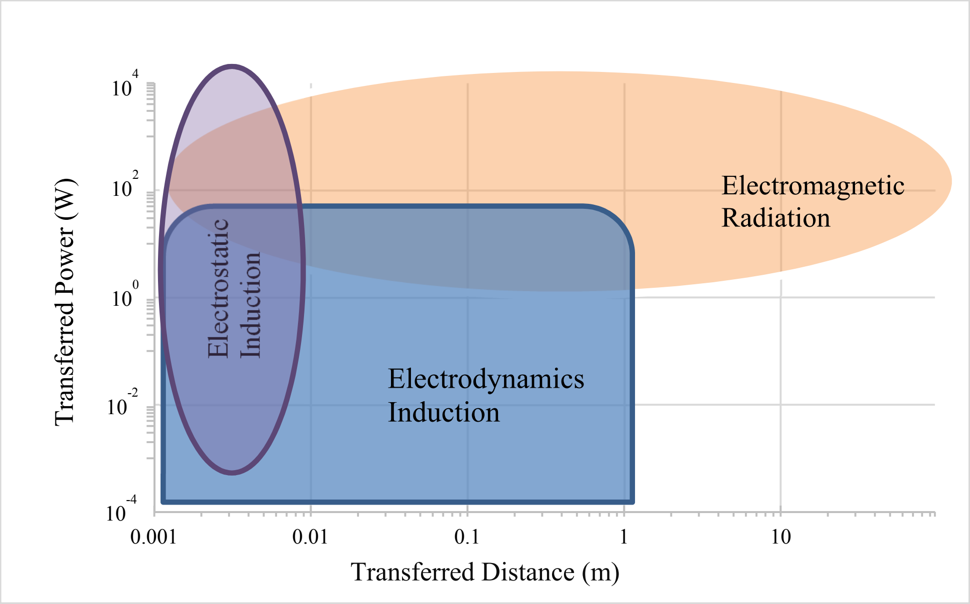

Figure 2-6 Wireless transferred power against transferred distance for different methods of wireless power transfer

Wu*, et al.* [86] presented the usage of a flexible and thin flat spiral coil for medical sensors and implantable devices that allows the structure to conform to the shape of the biological profile, the WPT system in this work provides 5.2 mW power. The energy required by the AAL system is typically more than 20 times larger than for medical usage, as reviewed in section 2.2.3. The large amount of energy requires bigger coils for power transmission, but the printing of the coils on fabrics is limited by the high costs of printable conductive paste, the requirement of comfort factor for wearable device, and the practical printed area the target user has in wearable applications, at the same time, the varied electrical characteristics of the coils limit their function in the WPT system. There is no research that shows WPT has been integrated into textiles by screen printing to supply power for the active devices in AAL applications.

2.4 Inductive Coupled Wireless Power Transfer System

2.4.1 System Structure

For the WPT system, coupled-mode theory for a general physical system is applied, the general physical system can be acoustic, electromagnetic, magnetic, or nuclear [8]. The system requires coils as the resonators operate in a strongly coupled mode, which the coils have same resonant frequency individually, but this resonance can be turned by compensating circuits which does not require the operating at the physical self-resonate frequencies of these coils. The simplest additional sub-system to turn the coils is constructed by resonant tank capacitors with both transmitter and receiver coils in parallel or in series respectively, which is widely employed in both academic research [87, 88] and commercial product [89, 90].

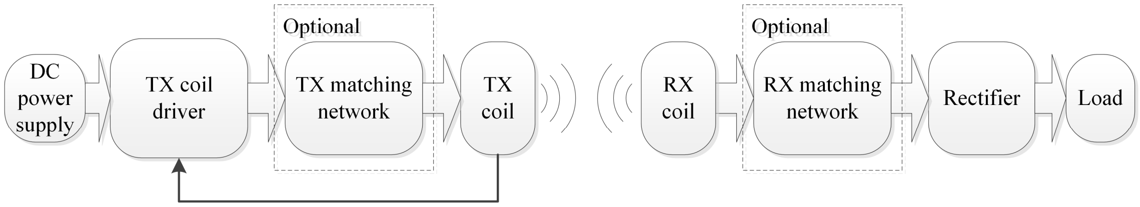

Figure 2-7 General structure of the WPT system

The general structure of a WPT system is shown in Figure 2-7, and shows that the coupled coils are essential elements. Progressing from left to right, the DC input power of the system is converted into an RF AC current by a transmitter (TX) coil driver, typically a high efficiency switching amplifier. An impedance matching network is used to couple the amplifier output to the source resonator efficiently while enabling efficient TX coil driver operation [91]. The coil connected to the AC source (transmitter) is called the TX coil. The AC current flowing through the primary winding sets up an alternating magnetic flux and thereby induces an AC voltage in the other coil, called the receiver (RX) coil. The induced power is then conditioned by the receiver to provide the desired voltage or current to the load. Due to the large leakage inductance and low coupling coefficient between the coils, resonant tank capacitors are formed by adding external capacitors, in order to improve its performance [92], and they are formed as a matching network on both the TX and RX sides. The feedback of the current in the RX coil and the current the load is consuming is provided by current detection on the TX coil and fed back to the TX coil driver to adjust the frequency and duty cycle [93].

2.4.2 Safety of Wireless Power Transfer

The safety of any electromagnetic field (EMF) is the most important factor of WPT when it is employed in wearable applications, and it follows published EU and international standards. The UK government recommends a guide line of exposure limits for EMF that are designed to prevent all known effects of fields on the human body, that will be legally enforceable from 2016 [94]. Table 2-5 lists the limits for EMF from organisations worldwide.

Table 2-5 Limits for EMF from organizations

Organisation	Document/Year	Magnetic fields (T)	Electric fields (V/m)
UK Department of Health	SAGE /2004 [95]	0.18×10^{-3}	460
International Commission on Non-Ionizing Radiation Protection	A Guidelines on Limiting Exposure to Non-ionizing Radiation /2010 [96]	0.3/f (in Hz) (300Hz – 3kHz) 0.1×10^{-3} (3kHz – 10MHz)	50×10^{3}/f (in Hz) (300Hz – 3kHz) 170 (3kHz – 10MHz)
European Commission	Directive of The European Parliament and of the Council on the minimum health and safety requirements regarding the exposure of workers to the risks arising from physical agents /2011 [97]	0.3/f (in Hz) (300Hz – 3kHz) 0.22×10^{-3} (3kHz – 10MHz)	800 (400Hz – 3kHz) 0.27f (3kHz – 10MHz)
Institute of Electrical and Electronics Engineers	IEEE C95.1 /2010 [98]	0.205×10^{-3} (3kHz – 5MHz)	614 (3kHz – 10MHz)

Both IEEE and ICNIRP have concluded that there is no established evidence showing that human exposure to RF EMFs causes cancer, this is because that radiation damages the human body because it has enough energy to break chemical bonds, but the quantum energy of RF EMFs are too small to break chemical bonds directly [99], and RF EMFs do not cause ionisation in body tissues. IEEE C95.1 gives the details of the limits for the tissues of the human body as shown in Table 2-6.

Table 2-6 EMF limits applying to various regions of the body [98]

Exposed tissue	Frequency (Hz)	Action level	Persons in controlled environments
		Electric fields (V/m)	Electric fields (V/m)
Brain	20	5.89×10^{-3}	17.7×10^{-3}
Heart	167	0.943	0.943
Extremities	3350	2.10	2.10
Other tissues	3350	0.701	2.10

RF EMFs may increase the temperature of human body tissues and stimulate nerve and muscle as established evidence shown in the investigation by World Health Organisation (WHO). The

IEEE and ICNIRP recommend limiting the specific absorption rate (SAR) less than 4 W/kg for the whole-body averaged level.

WiTricity from MIT [89] uses a technique for single hop wireless power transfer, it employs the precisely turned coils, which have high unloaded and loaded Q factors, to achieve a relatively high efficiency (> 50%) with different wireless transfer distances range from millimetre to metres for different designs [91]. In the different designs, it has the capability of transferring power levels from milliwatts to kilowatts for different applications. A demonstration kit shows a high efficiency of up to 68% can be achieved [100], low loss rates on high loaded Q factor coupled system keep the stray EMFs below the human safety limitaion. The large operating frequency range for the WiTricity system from 100 kHz – 10 MHz gives a wide range of the TX and RX coils that can be used with the system. The system follows the human exposure guidelines determined by the IEEE and ICNIRP, simulations on nerve, muscle, and tissue heating have been taken using the sophisticated modelling tools developed by this company, and the results of simulations show a safe value well below the guideline recommended by IEEE and ICNIRP [91].

The Wireless Power Consortium presents Qi, which is the open standard for WPT [101]; it has strict safety controls defined in its protocol and over 100 companies are working together on this standard to ensure safety and compatibility. It transfers power in a contactless way based on near field magnetic induction between coils. The power it transfers is around 5 W and is mainly used to charge portable devices. The operating frequency is defined in the range from 100 kHz to 205 kHz. A WPT system can be fabricated into a surface, and the target device can be provided with power through any location on that surface. To achieve a very low energy consumption in a standby state, this standard defines a simple communications protocol enabling the receiver to take full control of the power transfer and increase or decrease the rate as required.

2.4.3 Driver and Receiver

The converters using for driving the TX coils and receiving energy from RX coils are composed of an inverter and a rectifier, respectively. The inverter of the driver in the WPT system converts DC power to AC, then provides current at the operating frequency in the TX coil, causing the TX coil to generate an oscillating magnetic field, the TX and RX coils resonate in this magnetic field, and this induces an AC voltage at the output of the RX coil. The rectifier converts this AC back to DC to supply power to the application.

The driver consumes power when it converts DC to AC, especially in the switch components [102]. The desired output power level is an obvious design consideration, relatively, the desired load impedance is the key factor of the driver and receiver circuitry design. In a WPT system, the energy loss caused by the transferred distance between coils is the largest fraction but unavoidable, so it is very important to decrease the loss in the power amplifier, which takes the second largest fraction.

Classic linear power regulators require low-frequency transformers and filters; the efficiency is limited when the frequency of AC is higher than 50 kHz [103], in comparison resonant switching power converters allow for efficient operation at frequencies above 100 kHz [104]. Most resonant power converters require frequency-modulated control when the load or the input voltage is changing. A narrow operating frequency band $(\Delta f / f_{min} < 15\%)$ is required to control the system as the load resistance varies from full load to open circuit. Kaczmarczyk [105] improves the efficiency of the driver and receiver to 97% in theory by using a resonant amplifier structure.

The zero-voltage and zero-current switching inverters are the most efficient inverters known so far for coil drivers operating at high frequency (> 1 MHz) [106-108]. The component values of the resonant circuit are chosen so that switches turn on at the zero voltage point to force them to work in the mode that the transistors are fully switched on or off. When the transistor switches at low dv/dt point, switching losses are reduced since the switch current and voltage waveforms do not overlap during the switching time intervals, switching losses are virtually zero. Because of the high loaded quality factor of the resonant circuit, the range of frequencies required for output-voltage regulation is as narrow as 5% for load resistances from a full load to an open circuit [109]. A MOSFET is used due to its body diode acting as the antiparallel diode [110] for the switch as it is required to conduct current in both directions. The main power dissipation in the power amplifier is typically power lost in the active device; therefore, MOSFETs are selected with properties as close to an ideal switch as possible [111].

The issues of excessive power loss and circuit destruction are caused by the mismatch between the switching frequency of the driving device and the resonant frequency of the load network. It can be solved by using a feedback loop in the driver such as:

- Current feedback [112].
- Voltage feedback [113].
- Frequency feedback [114].
- Impedance matching network [110].

Current and voltage feedback methods have high efficiencies when the loads are varied in a narrow range. When the compensation for the load is fixed based on its electrical characteristics, frequency feedback reduces in efficiency because the effect of the compensation is changed by the operating frequency.

The Qi standard driver using single-stage full-bridge resonant topology, it has the advantage on the efficiency of DC to AC conversion in the frequency range between 100 kHz to 200 kHz. The standard driver is a flexible and high integrated platform, it is selected as the driver to test the coils used in this thesis.

2.4.4 Characteristics of Coils

Most research on WPT [115-117] utilise cylindrical coils formed using copper wire, which have advantages of low resistance and low parasitic capacitance than screen printed flexible coils, but they are rigid and take a considerable amount of space and supports for these coils. A flat coil is more applicable to application in a wearable device [118]. Zolog, *et al.* [119] review different shapes of flat coils with expressions involving dimensions, width of track, width of space between tracks, thickness of tracks, and inner as well as external diameter. The basic relationship between the physical dimensions and electrical characteristics is discussed, which gives a guide to the design of a flat coil to obtain the desired electrical characteristics. Zierhofer and Hochmair [11] present experimental work on the geometric approach for the enhancement of the Q factor and coupling coefficient of flat coils, the optimal diameters of a flat coil has been examined using simulations. For the commercially available WPT system, WPC recommends a Q factor of at least 77 for the coil with its compensating circuit [120]. The design of a flat coil for this thesis is discussed in Chapter 5.

2.5 Screen Printing

Smart fabrics and e-textiles are being developed for many applications including biomedical sensing, wearable computing, large area sensors and large area actuating devices [121-124]. An integrated system on a fabric provides new and unique services based on a flexible and wearable platform [39], such platforms enable the ability to enhance product performance. Thick-film screen printing technology is selected as the fabrication method for the coils of the WPT. Coils on a flexible dielectric substrate are accepted because they are comfortable or can be ignored [85].

2.5.1 Background of Screen Printing Technique

The screen printing technique is used in everyday products, as well as specifically targeted designs, electronic circuits and components can be printed on a fabric substrate [125]. Items that previously only existed as an assemblage of discrete components and partially integrated circuits are now being manufactured into fully integrated devices using conventional printing techniques [126].

Thick-film screen printing breaks into industrial applications, importantly the electronic field, such as in conductive track, resistors, inductors, capacitors transistors, photovoltaic panel, displays, lighting, sensors and mechanical actuators. Recently, these components have been integrated into textiles by screen printing, producing an e-textile. Zhu*, et al.* [117] integrated energy harvesting techniques into clothing and the energy harvester provides 2 μW by collecting the vibration energy from the flexing of the clothes, this can power many passive sensors but is not sufficient for many active devices. A battery is the most common option for power-hungry applications (>100 mW) [127]. WPT is not currently integrated into textiles, but it can provide a solution for power supplies to reduce the size and weight of e-textiles instead of using batteries to power them.

The screen printing technique uses the simple principle that, by adding pressure to the paste on the screen, the paste goes through an image carried by the screen which consists of a rigid frame, which then builds the pattern on the substrate. The essential items for making a screen print are as below:

- A screen, comprising a frame upon which a mesh is stretched.
- A photo stencil of the required design attached to the mesh.
- A squeegee, comprising a holder into which is fitted a flexible, resilient blade.
- A functional paste for printing.
- A secure base on which to position the component to be printed.
- A screen printing machine to operate these five items above.

An example structure of a screen is shown in Figure 2-8. The screen is a stretched mesh made from fine polyester or stainless steel wires. The mesh supports a stencil of the required image, the area without paste is covered by an emulsion, which is applied to both sides of the mesh with a thickness that will separate the mesh from the substrate. The open area of the screen controls the paste flow that is determined by the count and filament diameters of the mesh. At the same time, the count and filament diameters of the mesh determine the profile resolution. Mesh materials include stainless steel and nylon; stainless steel can achieve a large open area and good stability of print size, while nylon has better flexibility and resilience as well as improving the squeegee wear.

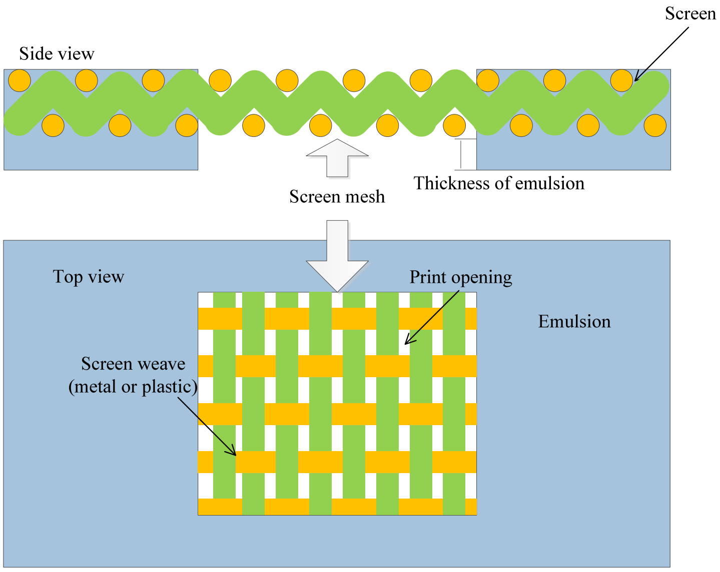

Figure 2-8 The structure of a screen

Thick-film screen printing can be deployed in a production line, by keeping the printing parameters the same, a rigid squeegee, and a constant pressure value, reproducible wet printing can be achieved for printing the same pattern in a large volume with the same result, making this printing process widespread in industrial production.

Thick-film screen printing can be applied to different types of paste, even powder [94], and different types of substrate [95], and wet print thicknesses between 10 - 100 µm can be achieved with an achievable resolution of 50 - 70 µm [96]. Table 2-7 shows the relationship between the key parameters of a common screen mesh and the typical wet print thickness.

Table 2-7 Screen mesh dimensions and wet print thicknesses [125]

Mesh type	Mesh count (per cm)	Filament diameter (μm)	Open area (%)	Typical wet print thickness (μm)
Stainless steel	59.1	50	46	57-117
	65.0	50	41	50-116
	78.7	50	36	45-115
	78.7	40	46	45-92
	128.0	27.5	41	27-62
Nylon	59.1	47.5	52	50-87
	47.2	35	47	32-75
	110.2	30	46	27-55
	129.6	30	37	25-50

Computer-Aided Drafting (CAD) software such as L-Edit or Autodesk Inventor can be employed to achieve accurate screen pattern design, and different layers can be designed at the same time with the advantages of easy operation and alignment. With the designed pattern on the screen, the functional paste is printed on the substrate, in practical fabrication processes, printing variables include the paste properties such as viscosity surface tension, evaporation rate, suspension stable and particle size; screen properties such as mesh type, mesh count, filament diameter and open area; machine settings such as speed and press applied on the squeegee, the distance between screen and substrate and the time delays between each printing step; drying and curing durations and temperatures.

2.5.2 Screen Printing Paste

Screen printing attracts significant interest due to its versatility in being able to print a wide range of materials on different types of substrate in a variety of shapes.

2.5.2.1 Surface Tension and Surface Energy

Obviously, the type of printing paste used must be compatible with the material of the substrate. The surface tension between the materials of the pastes for each layer must be matched. A high surface tension causes the paste to separate as individual drops, and gaps are occurred between drops of the paste which results a rough surface on the cured layer and disconnections within the printed pattern. A low surface tension causes the printed paste easily spread itself that cannot remain in the given profile by screen. This results larger and thinner prints than design without any pattern. The printed results of mismatching and matching are illustrated as shown in Figure 2-9.

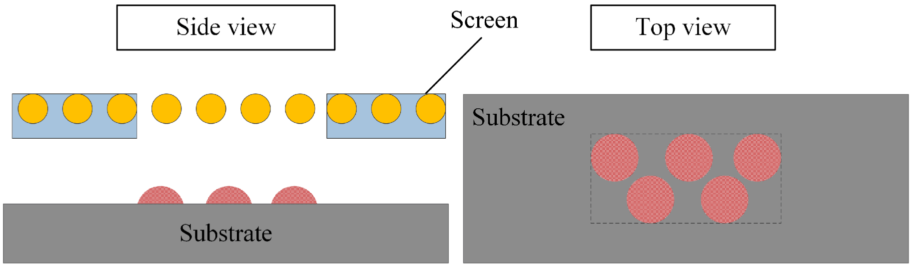

Mismatching (high surface tension)

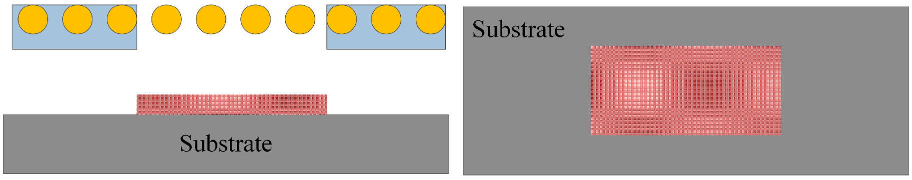

Matching

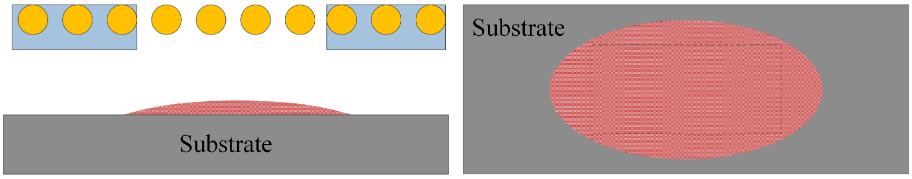

Mismatching (low surface tension)

Figure 2-9 Effect of matching the surface tension between two materials

In this thesis, three functional pastes are used: an interface layer; a conductive layer; and a crossover layer. These are selected to match the surface tension of the substrate.

2.5.2.2 Sheet Resistivity of Conductive Paste

The coil is composed of the conductive layer, and the sheet resistivity of the conductive paste determines one of the key parameters of the coil, DC resistance. The sheet resistivity has the unit $\mathrm{m\Omega/\square/mil}$, which presents the resistance of a square sheet conductor with a typical (specified) thickness. A common conductive silver paste from DuPont, DuPont 5000, has a sheet resistivity of $R_{sheet} = 15\ \mathrm{m\Omega/\square/mil}$ [128], and another one from Smart Fabric Inks Ltd, Fabink-TC-AG4002, has a value of $R_{sheet} = 15{\sim}17\ \mathrm{m\Omega/\square/mil}$ [129]. The values of these two conductive silver pastes are the lowest sheet resistivity commercial currently available for use with textiles. A copper tape made from the solid copper is used to compare with the printed paste in Chapter 6, the solid copper has a resistivity of 16.8 nΩ·m, which is equivalent as $0.66\ \mathrm{m\Omega/\square/mil}$. It means that the coil made from the copper tape will have approximately 4 % resistance of the resistance a printed coil with same design and thickness has.

2.5.2.3 Permittivity of Dielectric Paste and Surrounding Material

The surrounding material of the coils produces the parasitic capacitance for the coils. The permittivity ε_r of the dielectric or interface material can be obtained from the datasheet or found experimentally. For instance, DuPont provides a crossover material that has a low permittivity of $\varepsilon_r = 4.4$ [130]. This crossover paste provides isolation from the conductive layer and brings in little parasitic capacitance. The permittivity of interface material has been tested to examine the interface coated textile, and the results will be shown in Chapter 6.

2.5.3 Screen Printing Processing

In thick film fabrication, the screen printer has the capability of printing a given type of paste through a patterned screen, during this process, the speed, pressure and snap-off distance of the squeegee travelling can be adjusted. For multi-layer printing, the specified alignment should be achieved to assured a functional fabrication. A DEK 248 semi-automatic screen printer, which is shown in Figure 2-10, is more convenient than a manual printer as the pressure and speed of the squeegee are controlled by a computer and the pressure can be controlled to 0.1 psi.

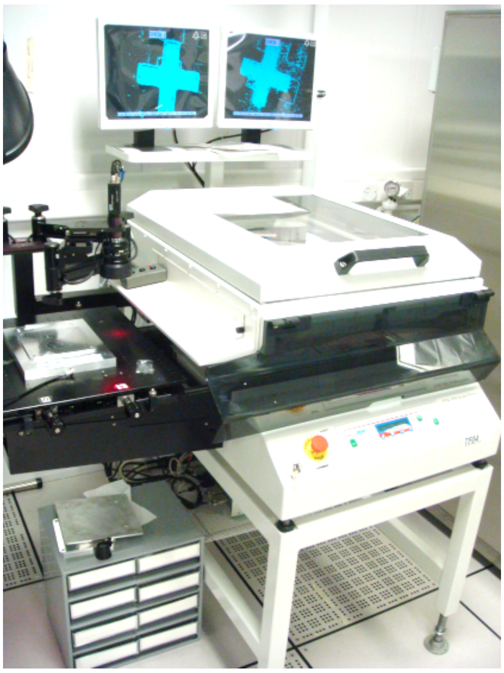

Figure 2-10 Semi-automatic screen printer DEK 248 from DEK

For multi-layer printing, cameras on the top of the tile holder for the substrate enable the required alignment for each layer to the previous layers and the substrate. The two monitors in Figure 2-10 show the alignment mark for multi-layer printing.

Figure 2-11 shows the thick-film printing processes including the following steps:

1. The preparation of substrate, the surface of the substrate must be clean and dry. The paste is mixed and prepared for printing, and a suitable quantity of paste is placed on the screen (I. Begin).
2. The flat blade pushes the paste, covering the pattern and making the paste even on the screen (II. Flood).
3. The squeegee travels back applying pressure to the pattern, the paste goes through the mesh due to thixotropic nature and surface tension effects, and then been printed on the substrate (III. Print).
4. The squeegee releases pressure, and the screen lifts off from the substrate (IV. Lift off).
5. Optional wet layers can be printed by repeating step 2 to 4.
6. Drying or curing process of the wet layer prior to printing another sub-layer with same pattern or a new layer can be printed on the dried or cured layer by repeating step 2 to 4.

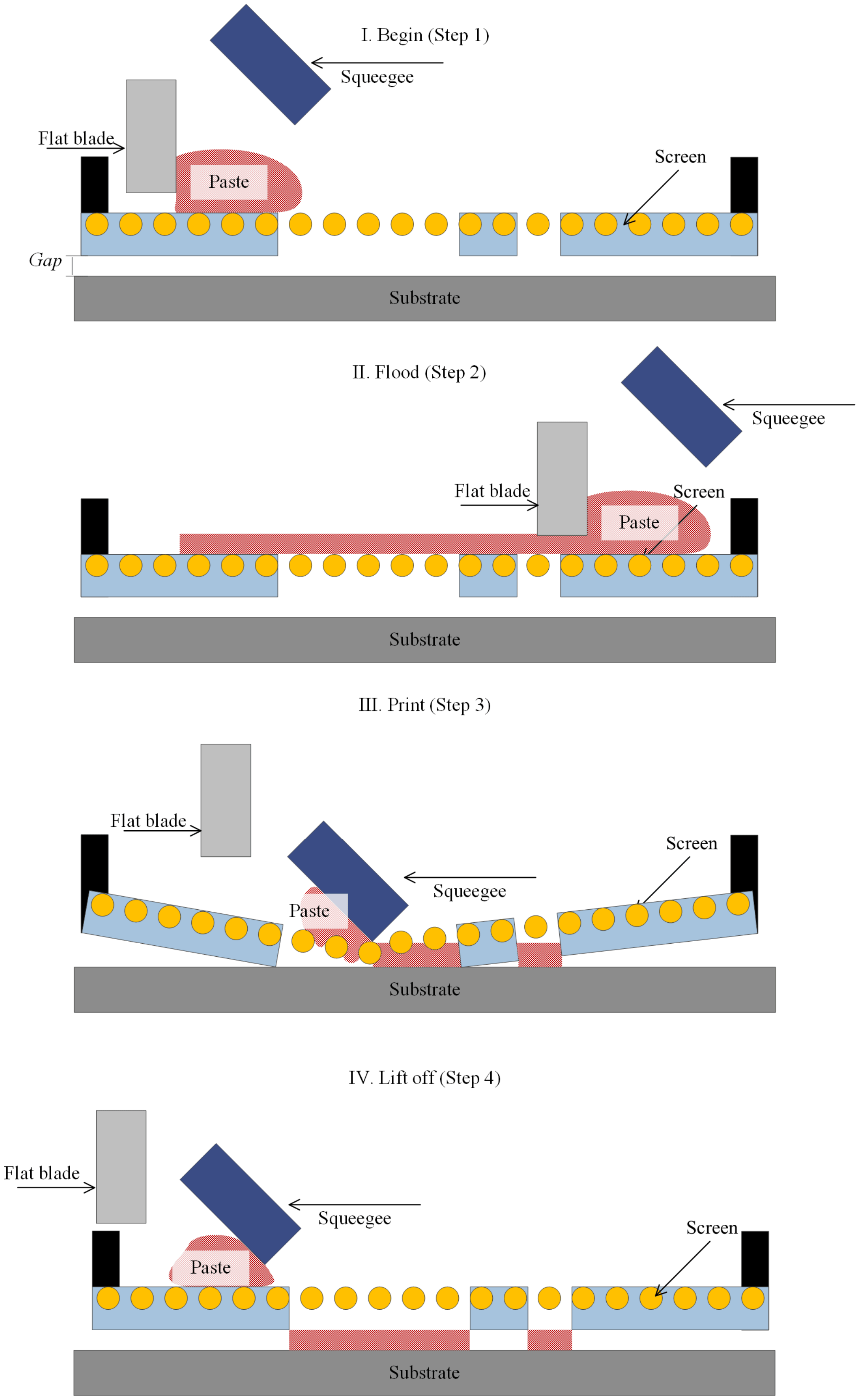

Figure 2-11 Screen printing process

The squeegee has the following functions: bringing the screen into intimate contact with the surface being printed; shearing and removing excess paste from the pattern on the screen; and controlling the rate of release of the screen. The blade of the squeegee has a flexible edge to follow the uneven surface of the screen rigidly, and it maintains a fixed angle and accurate cut-off of the paste [131]. The attack angle and the hardness of the squeegee control the filling quantity of paste printing and the clearance of excess paste, as well as the down pressure on the edge of the squeegee deforming and changing its attack angle. The higher the down pressure the more the blade deforms and during the squeegee traverse, the smaller the angle of attack becomes, which produces a heavier deposit. The speed of the squeegee controls the time of contact. A high speed of travel has the expense of increased squeegee and screen wear, and with possibly some loss of accuracy of paste metering, but low speed results in a long contact time and therefore obtains fine line printing [125].

2.5.4 Curing Process

A belt dryer, such as the DR92-5-60D from BTU shown in Figure 2-12, is widely used to dry and cure low temperature (lower than 300 °C) thermal cured layers. It has a moving belt that carries the components through several variable temperature zones.

Figure 2-12 Belt dryer from BTU

Over a fixed distance, the speed of the moving belt is adjusted to provide the desired temperature processing period, therefore the required drying or curing duration can be achieved. Temperature zones have a ramp of increasing and decreasing temperature gradients rather than immediate temperature changes. The ramp of increasing and decreasing temperature during the curing processing is preferable since it provides a relatively smooth surface on the cured layer. As the materials have different thermal stress coefficients, an unsuitable drying scheme causes the printed layer to peel off or have surface cracks due to the irreversible deformation between materials with different measures of the expansions or shrinkages.

Materials sensitive to high temperatures such as plastics have to be processed using ultraviolet (UV) curing systems since thermally cured systems show poor results when the curing temperature is below 100 °C [132]. A UV curing cabinet, as the one from SCH Technologies shown in Figure 2-13, can be used to cure UV curable layers. It can adjust the distance and the time of the layer exposed under the UV light, the distance controls the power density of UV light radiated on printed layers during the curing process, and the time controls the overall energy of UV light applied on printed layers.

Figure 2-13 The UV curing cabinet

When the paste is cured, the solvent is removed from the substrate. A proper curing process is required because the solvent affects the function of the paste, such as giving a high resistivity to the conductive paste. Bubbles can occur when one uncured layer has another layer printed on it, the upper layer seals the uncured layer and keeps the evaporated solvent between these two layers as bubbles when the condition of evaporation been met. These bubbles break the upper layer and invalidate the functions of such layer such as isolation and protection. In addition, especially for the conductive paste, the random curing status on the conductive layer will cause the unpredictable skin effect when it has been employed as the coil and has an AC flowing.

2.6 Summary

This chapter has introduced the applications of AAL systems in buildings and the on-body area, and gave an overview of the advantages of AAL systems. Sensors and networks for the operation of AAL systems have been reviewed both from academic research and the commercial market. Four types of power supply for AAL systems: mains wired; battery; energy harvesting; and WPT, have been explained in detail for the different applications with their respective advantages and disadvantages.

To supply the power wirelessly for an AAL system in this thesis, two methods are selected after reviewing. For passive sensors with buildings, ambient light energy is a more consistently available energy source for self-powered devices than other ambient energy sources such as vibration or thermal energy, as the majority of daytime activities require the presence of suitable illumination levels. For power-hungry devices in on-body applications, WPT can be deployed to provide sufficient power for the active sensors and networks, and the technique, the standard of safety, and researches on circuitry of the WPT system has been reviewed.

According to the reviewed relative research and systems in the market, the wireless power investigated in this thesis can proved the power for different AAL applications. For instant, the energy harvest technology can be deployed into the human tracking system in building area, and the WPT system can be deployed in on-body area monitoring system.

The application of the system on body area requires the WPT system with the wearable feature, a novel flexible WPT coil is demanded. To establish the effect of the flexible coil on the WPT system, the general WPT system structure has been reviewed. The safety for the user is always the priority in the design of the wearable system, the relative recommendation about the limitation on EMF has been reviewed. The driver and receiver circuit and the specification of the coil have been reviewed to investigate the compatibility of the flexible coil with the WPT system. Compare with the existed WPT system with wound copper coil, the flexible coil has the limitation on the resistance, this limitation will reduce the efficiency of the WPT system, consequently, a DC to DC efficiency approximately 40 % is expected for the WPT system employing the flexible WPT coils.

To produce flexible WPT coils suitable for fabrication on textiles, the thick-film screen printing technique has been reviewed including selected functional pastes, the screen printing process and the curing process. This chapter has given a literature review for the current state-of-the-art in AAL systems, their power supply, WPT, and thick-film screen printing for the following system design and experiments.

3 A Solar Powered PIR Sensor for Fixed Node in Ambient Assisted Living System

Occupancy detection is an essential piece of information in the contents of an AAL system. In this chapter, a solar powered PIR detector is designed for occupancy sensing. The functions and power consumption of its main components are investigated. Different types of solar cells are investigated under different light sources typically encountered within buildings. A power management subsystem is designed for a self-powered device, and the PIR sensor is powered from the same supply voltage as the Micro Control Unit (MCU) and transceiver. A shell for the PIR detector is designed and then fabricated by 3D printing to give the support curve for the flexible solar cell. An algorithm for energy-aware embedded wireless communication is designed. The system is examined in office environment and the feasibilities of design of both hardware and software are verified.

3.1 Introduction

In an indoor AAL scenario, light is the most prevalent ambient energy source for an energy harvesting device. The light energy from either natural or artificial sources can be harvested using photovoltaic devices. A range of different types of solar cell are available to suit differing light sources and intensities, these must be selected to suit the type of light and its intensity. The selection of solar cell is discussed in Section 3.2.

The PIR detection demonstrator device uses selected commercially available solar cells combined with custom energy management electronics to attain high efficiency wireless power supply solution. It has the capability of sensing movement and temperature, which can be used for occupancy sensing for individual room or human tracking with sensor network. Figure 3-1 shows the system overview of the device.

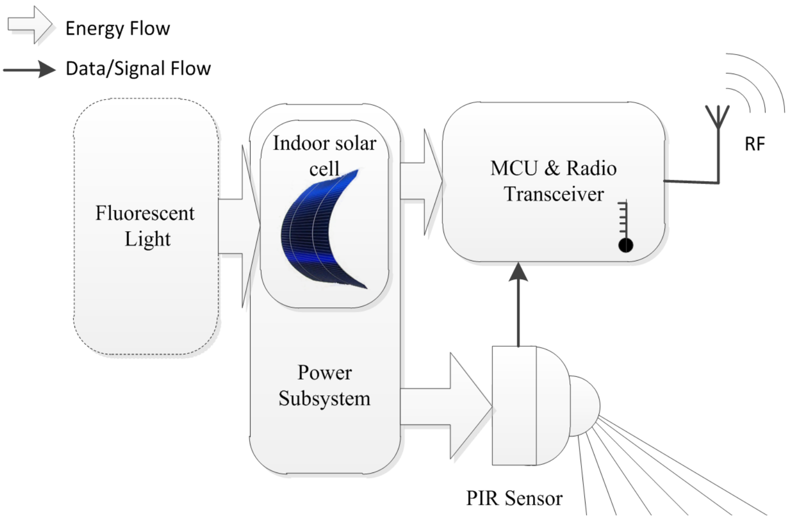

Figure 3-1 System overview of the solar powered PIR sensor

This device is typically installed on the wall of a typical office room. The lighting supplied by fluorescent fitting that range from 200 lx to 1000 lx on the surface of the device, and the ambient temperature is around 20 °C. A power subsystem within the device includes:

- A solar cell which converts the ambient solar energy to electrical energy.
- An energy extraction circuitry which makes the solar cell work around its Maximum Power Point (MPP).
- Energy storage which ensures that the system can continue to operate when there is no light energy available.
- A booster circuit which extends the range of the output voltage of the energy storage, it boosts the voltage of the MCU power supply.
- A latch circuit makes the voltage continuous at the MCU starting phase.
- A protective circuit which prevents the energy storage over charging and damaging the components, and also prevents the supply voltage from being erratic which results in the MCU being stuck in its starting phase.

Inside buildings, there is limited or no natural light in some locations or at some times. When natural solar energy is not available, photovoltaic devices must rely on artificial light sources and therefore the solar cell must operate efficiently under artificial lighting. The power sub subsystem is required to supply the power to the MCU, radio transceiver and Passive Infrared sensor (PIR) continuously as well as charge and store energy for the system operating at least 14 hours without any light energy input. The circuit design is discussed in Section 3.3.1, and the practical operation is exanimated in Section 3.4.

The sensing devices are the PIR and the temperature sensor integrated in the MCU. The PIR can detect 1 m/s movement of an object that has 4 °C temperature difference from ambient within 12 m which is caused by a human presence in this context. The temperature sensor has 0.5°C accuracy within the range from 0°C to 105°C with a typical error of ±0.3°C, it can measure ambient temperature when the system working normally, or alarm a system error if a rapid increase in temperature is sensed.

When a movement of human presence is detected, the MCU moves out of Low Power Mode (LPM) because an interrupt is sent from the PIR. The MCU measures the ambient temperature and forms a data packet that includes the energy storage voltage, supplied voltage of the MCU and the ambient temperature. After this system self-check, it transmits the packet via a 2.4 GHz wireless radio transceiver. The movement of human presence normally continues at least 5 s within the 12 m detection range, thus the MCU waits for the movement to pass for 5 s and will not measure or send anything during this term. After this 5 s interval, the MCU goes back to the LPM and waits for the next movement to occur. The algorithm design of software is discussed with communication protocol in Section 3.3.2.

3.2 Hardware Investigation

In this section, a range of commercial solar cells, MCUs, radio transceivers and PIRs are investigated and selected for the PIR detection system. The system is constructed from three part according to Figure 3-1:

- An indoor solar cell to convert the light energy to electric energy.
- An MCU with LPM, 10 I/O ports, ADC function to control the system.
- The radio transceiver that meets the ultra-low power requirement to save energy and works effectively for an entire day.

The speed of the MCU and radio transceiver is not a priority because there is no heavily arithmetic work to do. Since each movement event takes 5 s at least, the system does not send messages frequently.

3.2.1 Artificial illumination sources

The nature of artificial sources is changing over time from incandescent sources, through fluorescent lights, with LED lights currently attracting significant interest due to energy savings. This impacts on the selection of the solar cell to achieve an optimum solution since the spectrum and intensity of the light source depends on its type. The light level should be constant irrespective of the type of source used in a building illumination system, but the amount of energy harvested by a photovoltaic device will change depending on the light source type, even for an identical light intensity. Of major importance to energy harvesting powered devices is that the solar harvester selected will harvest sufficient energy when deployed irrespective of the light source providing the illumination. One danger is that a solar cell based energy harvester will work perfectly with a specific light source, upon installation, but, when the building occupant changes the type of light source, for example when the bulb expires, the harvester produces insufficient energy for operation. It is necessary to investigate the effect of different types of light source before the design of a power supply for an energy harvesting device to mitigate this risk.

This work investigates the output power achievable from four types of solar cell under three different artificial illumination sources typically encountered within buildings, for various illumination levels: incandescent (halogen), compact fluorescent lamp (CFL) and LED (white light LED and colour-controllable LED). Within the LED lighting category both a standard white light LED device and an RGB colour-controllable LED have been utilised. The use of the RGB source permits the analysis of the effect of varying the illumination spectra from a nominally white spectrum.

3.2.1.1 Static Characteristic of Different Light Sources

Examples of the typical illumination sources, a 20 W incandescent lamp which can be replaced by an 11 W CFL lamp or a 1 W white light LED lamp, are shown in Figure 3-2.

Figure 3-2 Typical illumination sources, from left to right: 20 W incandescent lamp, 11 W CFL lamp, 1 W white light LED lamp, 6 W RGB colour-controllable LED lamp

The energy saved by individual lamps used in this work is different to the quoted energy saving given in Section 2.3.2 for the upgrade of an entire illumination system; a 45% reduction with the CFL lamp used in this work compared to 70% for a full CFL upgrade, and a 98% reduction with the LED lamp used in this investigation compared to 85% for a full LED upgrade in literature review. This difference may arise because the upgrade of a full illumination system involves alterations in supply circuitry as well as installations of the lamps themselves. The different lenses in front of the lamps used in this work also cause the beam shapes of tested lamps to be different, which causes the lamps tested to have different, non-uniform, power density profiles on the illuminated surface. The lens on the CFL lamp creates a wide beam, with an illuminated area about four times larger than that provided by the incandescent lamp at the same distance from the source. The lens on the white light LED creates a narrow beam, with an illuminated area about half the size of that of the incandescent lamp. These illumination areas were measured with a 200 mm distance between tested lamp and the illuminated surface by a light meter (ISO-TECH Lux-1337). However, lux levels do not establish the power of the light in all wavelengths, instead a standardised model for human brightness perception is used which is wavelength weighted by a luminosity function [133].

Because the different lamp types used utilise different emission methods to produce their illumination, the spectral content of the emitted light varies between the lamp types. The 20 W incandescent dichroic reflector lamp has a colour temperature (CCT) of 2800 K, the 11 W CFL lamp has a CCT of 6400 K, and the 1 W white light LED lamp has a CCT of 3500 K. For comparison purposes in this work the natural solar light is measured indoors in an open plan office space with the light passing through double glazed windows with glass that is treated to reduce solar heating effects, the glazing in the area used for these tests is specified as T80 double glazing with BM TRADA Q-Mark 012/001-03 certificated glass (BM TRADA, 2012). The spectral distribution of each light source is measured by a spectrometer (Ocean Optics USB2000 with 10.0 nm resolution) as shown in [Figure] and using following procedure for the selected different type of lamps:

1. Mount the selected lamp into the opaque enclosure.
2. Turn the testing lamp on, and allow the output to stabilise.
3. Adjust the illumination level on surface of the sensor of the spectrometer to the desired lux level by changing the distance or filters between the solar cell and the lamp, using a light meter (ISO-TECH Lux-1337 with 0.01 lx resolution, overall accuracy of ± 3%, 5 digit readout) placed at the location the spectrometer is to be located at to measure the illumination level. Once the desired illumination level is obtained the light meter is replaced by the spectrometer.
4. Record the spectral distribution of testing lamp via USB.

For the natural light, the spectrometer is placed near an office window, where has same illumination level measured by the light meter, and then record the spectral distribution of the natural solar light.

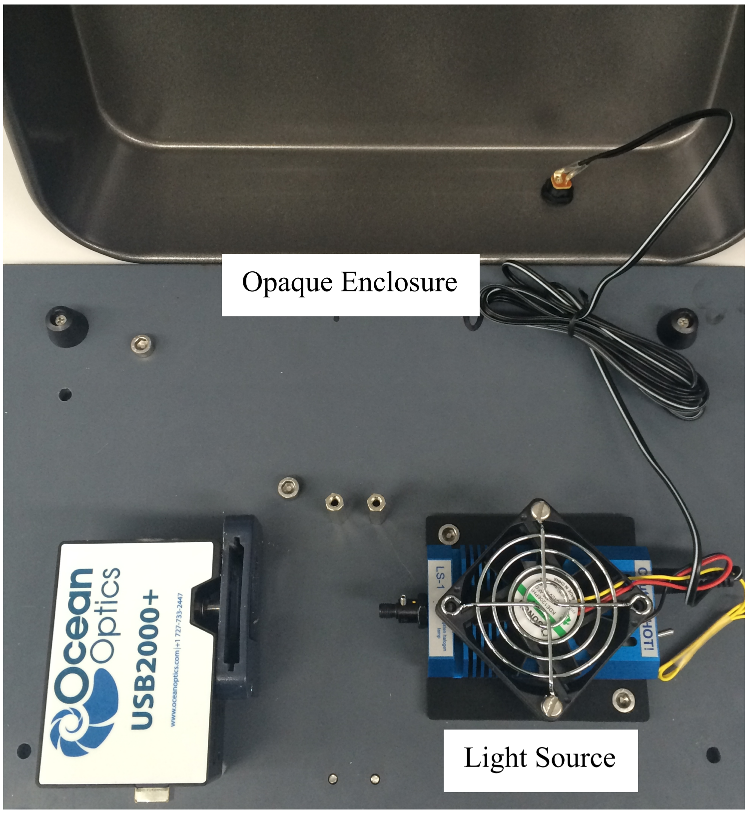

Figure 3-3 Deployment of the experiment for measuring the spectral distribution of different light sources

The measured results of spectral distributions are shown in Figure 3-4.

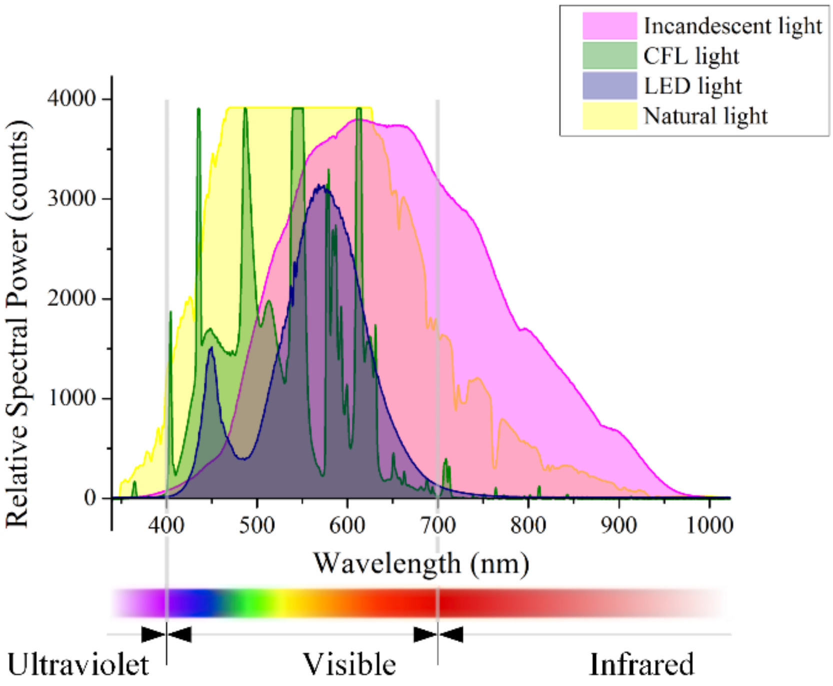

Figure 3-4 Wavelength spectra of typical indoor light sources compared with natural light

The spectrometer presents spectral data as raw counts detected by each of the sensor pixels, with the number of photons per count dependant on the response of the sensor, and the recorded spectra are therefore relative not absolute spectra. Due to a limitation in the illumination levels that can be measured by the spectral measurement device used, the output levels from natural light between 469 nm and 626 nm and from CFL light between 542 nm and 550 nm have saturated the sensor at its maximum level. However, it is clear from Figure 3-4 that the spectral distribution of light energy will change following a change of the type of illumination sources.

Colour-controllable LEDs in a directly interchangeable format are a recent addition to the lighting market. In addition to the basic lighting function they can also be used to change the colour of an environment for entertainment or recreational purposes such as changing the illumination colour to fit a particular mood or activity. These lamps are usually remotely controlled, either using a specific wireless remote controller or from a Wi-Fi or Bluetooth enabled device such as a smart phone or tablet. An example of a colour controllable LED lamp is included in Figure 3-2 on the right. The wavelength spectra of this device is shown in Figure 3-4 with the lamp in its red, green, blue modes and a white mode which is a composite of the RGB modes.

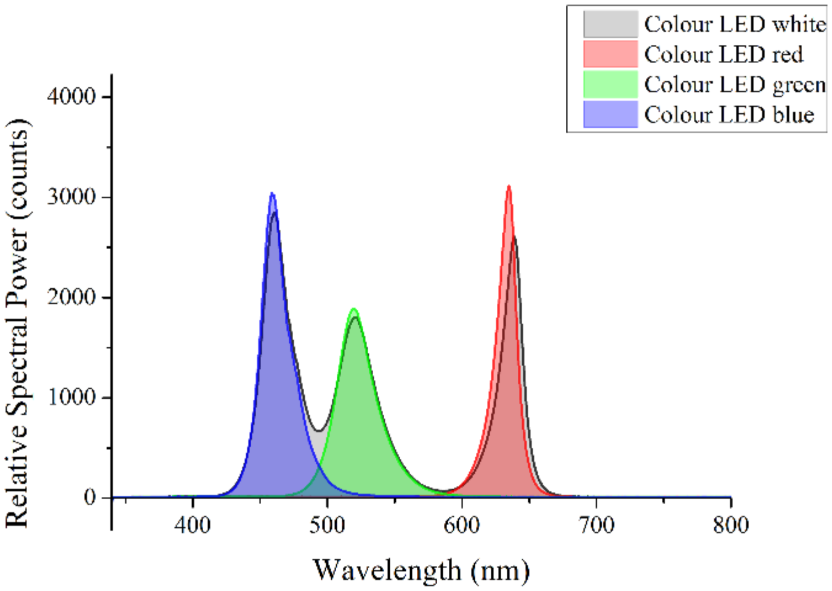

Figure 3-5 Wavelength spectra of RGB colour-controllable LED in red, green, blue and white modes

In the figure, relative spectral power peaks of three primary colours of light occur at different wavelengths, and the overlapping areas between each primary colour have relatively low spectral power compared to these peaks. The spectral power from the three primary colours are summed to form the spectral power characteristic of the white light mode from this lamp which is why it cannot be independently identified in Figure 3-5.

3.2.1.2 Warm up time for CFL and LED

In the design of solar energy harvesters the light source is often assumed to be stable, in reality, there is a longer warm-up time for CFL and LED lamps than for incandescent ones. Therefore to give a true indication of the longer term operation of the solar energy harvester it is necessary to ensure that these light sources are in the stable operating state prior to performing the measurements. The halogen incandescent lamp used in the test reaches its stable illuminating state in less than 10 seconds because the lamp filament quickly heats to the operating temperature. The CFL and white light LED lamps used require a relatively long settling time after their initial turn on for them to warm up and for their output illumination level to become stable. By mounting a solar cell and the CFL or LED lamp into the opaque enclosure and then turning the lamp on, these responses have been measured by recording the output voltage of the solar cell, which with a resistance load to force it working at its maximum power point recommended by the manufactory, during the warming up period. The responses are shown in Figure 3-6.

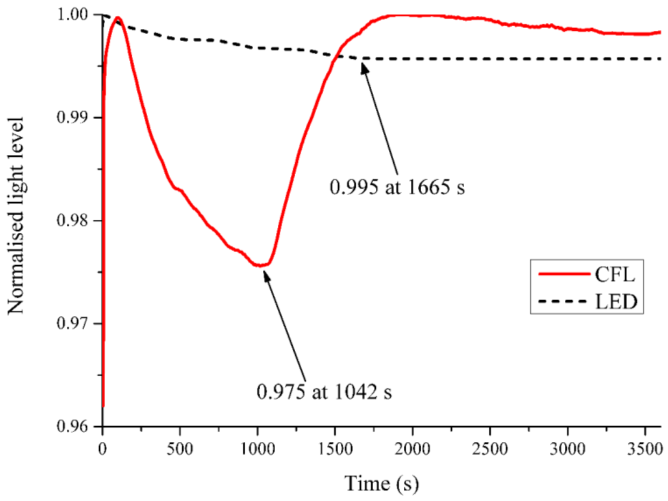

Figure 3-6 Output intensity variation after turn on for CFL and LED sources

In the figure it can be seen that the CFL lamp shows a drop down to 97.5% of the maximum output power density up to 1132 seconds before rising to back to its maximum output and becoming stable. Compared with the CFL lamp, the white light LED has a more stable performance. Both CFL and white light LED are stable after 1 hour in the test. For energy harvesting devices, the collected power therefore changes over time during the warm up phase and is different from the stable state.

For the RGB colour-controllable LED, the warm up time curves, shown in Figure 3-7, generally follow that of the white LED as shown in Figure 3-6. The differences of power density change between the red, blue and green are less than 1%.

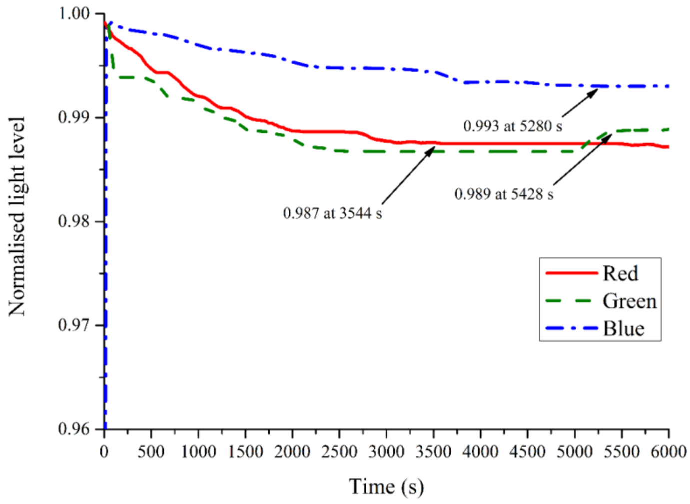

Figure 3-7 Output intensity variation after turn on for RGB colour changeable LED

For the purpose of our investigation all the light sources used were allowed to warm up for a sufficient time so that they had reached their stable operating condition. Therefore the given typical illumination levels of the devices under test do not take into account any initial short term variation in the output levels of the light sources.

3.2.2 Solar Cells Investigated

The four different types of solar cells used in this work were selected because they represent the main types available; they are made from different materials optimised for use either outdoors or indoors. The key details of these four solar cells are shown in Table 3-1.

Table 3-1 Details of the selected solar cells including the use that each one is optimised for

Model	Material	Use	Manufacturer	Appearance	Active Area
MC-SP0.8	Polycrystalline silicon	Outdoor	Multicomp		68.64 cm^2 (88 mm × 78 mm)
AM-5608	Amorphous silicon	Outdoor	Panasonic	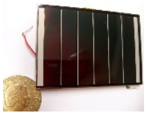	20.28 cm^2 (52 mm × 39 mm)
AM-1815	Amorphous silicon	Indoor	Panasonic	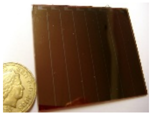	25.2 cm^2 (56 mm × 45 mm)
Indy4050	Dye-sensitized (flexible)	Indoor and outdoor	G24i	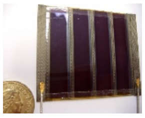	30.5 cm^2 (50 mm × 61 mm)

The different materials of solar cells have differing spectral sensitivities. A comparison between those of the amorphous silicon, poly-crystalline silicon, and dye-sensitized types is presented in Figure 3-8, this is based upon spectral performance data provided by Panasonic [68] and G24i [134].

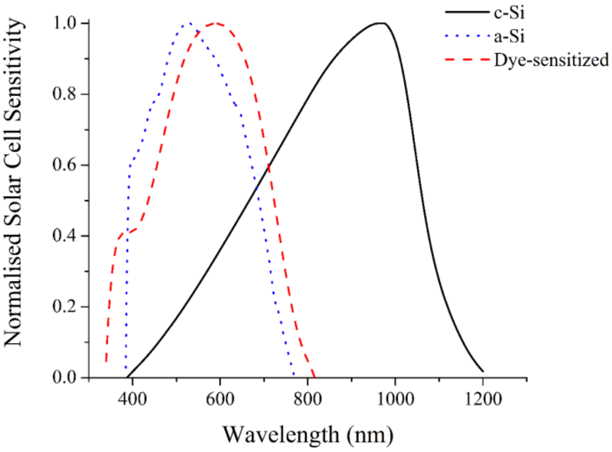

Figure 3-8 Spectral sensitivity of poly-crystalline silicon, amorphous silicon and dye-sensitised solar cell types

In this figure, a value of each plot is normalised to each own peak value, since the data is given by different manufactures without a unified measurement. Consequently, the solar cell sensitivities are not comparable between different types.

3.2.2.1 Multicomp MC-SP0.8

The MC-SP0.8 solar cell from Multicomp is made from polycrystalline silicon which is widely used in the production of solar cells and has a spectral sensitivity designed to match the wavelengths present in sunlight. It is therefore suited to providing power for outdoor applications where the typical illumination levels are in the range of 1000 to 100, 000 lx. This mature technology has a best achievable efficiency of 14% under standard Air Mass (AM)-1.5 test conditions [135]. Table 3-2 shows the main parameters of Multicomp solar cell MC-SP0.8 which from its datasheet.

Table 3-2 MC-SP0.8 solar cell parameters

Condition	V_{Max} (V)	I_{opr} (mA)	Thickness (mm)	Weight (g)
200 lx	1.56	0.04	4.9	20
1000 lx	3.85	0.21		

3.2.2.2 Panasonic Amorton AM1815 and AM5608

Amorton is a series of integrated amorphous silicon solar cells which have been developed by Panasonic. ‘Amorphous’ refers to objects having no definite shape and is defined as non-crystalline material. Unlike crystalline silicon, amorphous silicon features irregular atomic arrangements. As a result, the reciprocal action between photons and silicon atoms occurs more frequently in amorphous silicon than in crystal silicon, allowing much more light energy to be absorbed.

There is an enormous difference between the illumination levels outdoors and indoors. The Amorton AM-5608 solar cell from Panasonic, made from amorphous silicon (a-Si), is used for outdoor applications under illumination levels in the range of 1, 200 to 100, 000 lx. The best efficiency it can achieve under standard AM-1.5 test conditions is 13.4%. The efficiency can be higher when it is operating under the illumination levels for which it is optimised.

The Amorton AM-1815 solar cell from Panasonic is also made from a-Si but is designed for indoor applications under lower illumination levels in the range of 20 to 1000 lx. The best achievable efficiency for the AM-5608 is also 13.4% because the same material is used.

Table 3-3 shows the main parameters of Panasonic solar cells from their datasheets. The minimum power output of AM5608 in 50 klx is 64.35 mW and AM1815 in 200 lx is 0.126 mW.

Table 3-3 Panasonic solar cells parameters

Model	Type	Condition	V_{Max} (V)	I_{opr}(mA)	T_{opr}(°C)	L(mm)	W(mm)
AM5608	Outdoor	50 klx natural light	3.9	16.5	-10 to +60	41.3	60.1
AM1815	Indoor	200 lx fluorescent	3	0.042	-10 to +60	48.6	58.1

3.2.2.3 G24i Indy 4050

The Indy4050 is a flexible solar cell from G24i utilising dye-sensitized solar cell (DSSC) technology. The DSSC has a best achievable efficiency of 11.4% under standard AM-1.5 test conditions. It has high flexibility of up to 10,000 flexures around a 25 mm radius with no measurable drop in performance. Since no glass components are used, the panel has high durability to impact. Its working conditions range from 200 lx to 1000 lx, and it is designed for indoor applications and it is thin, lightweight and water resistant.

Table 3-4 shows the main parameters of Indy4050 solar cell from its datasheet [136]. The minimum power it output in 1000 lx is 1.344 mW and in 200 lx is 0.162 mW.

Table 3-4 Indy4050 solar cell parameters

Condition	V_{Max} (V)	I_{opr} (mA)	Thickness (mm)	Mass (g/cm^2)
200 lx	1.81	0.049	0.35	0.06
1000 lx	2.03	0.238		

3.2.2.4 Output Testing of Solar Cells

The output power densities of the four solar cells (polycrystalline silicon MC-SP0.8, amorphous silicon for outdoor applications AM5608, amorphous silicon for indoor applications AM1815 and dye-sensitized Indy 4050) are measured under three types of typical illumination source (incandescent, CFL and LED lights). The measurements are performed in an opaque enclosure to shield the solar cell from ambient light. The light source is mounted inside the enclosure, and the solar cells are situated at the centre point of the illumination as shown in Figure 3-9 (a).


(a) (b)

Figure 3-9 Deployment of the experiment (a) opaque enclosure and lamp holder; (b) filters to adjust the luminance level

The experimental method was as follows:

1. Mount the solar cell and light source into the opaque enclosure and allow the output from the light source to stabilise.
2. Adjust the illumination level on surface of solar cell to the desired lux level by changing the distance or filters between the solar cell and the lamp as shown in Figure 3-9 (b), using a light meter (ISO-TECH Lux-1337 with 0.01 lx resolution, overall accuracy of

± 3%, 5 digit readout) placed at the location the solar cell is to be located at to measure the illumination level. Once the desired illumination level is obtained the light meter is replaced by the solar cell under test.

3. Vary the load on the output of the solar cell and record the output voltage from the solar cell and the resistance of the load.
4. Use the load resistance and output voltage values to calculate the output power density of the solar cell.
5. Plot the output power density of the solar cell against its operating current.
6. From the output power density plot, locate the maximum power density point of the solar cell and the range of output currents at which solar cell can provide at least 90% of the maximum power density.

A maximum value of error of ± 4.2 % has been plotted based on the cumulative quoted errors of the light meter, A/D convertor and resistance box. This plotted error has been verified experimentally to be less than the spread of measured values which is ± 1 %. A multilayer filter was used in conjunction with varying the separation between the source and solar cell to enable the desired illumination levels to be achieved. The filter material was used to add additional attenuation in the case of sources which provided a higher illumination level than was required at the target with the source and solar cell at maximum separation. Relatively, the multilayer filter should only change the illumination levels without any alteration on the spectral distribution of the tested light source on the surface of the solar cell. The filter material used shows a uniform spectral response over the spectral range of 400 to 900 nm, Figure 3-10 shows the relative spectral power of the incandescent lamp when a number of different layers of filter were added between the incandescent lamp and the spectral measurement.

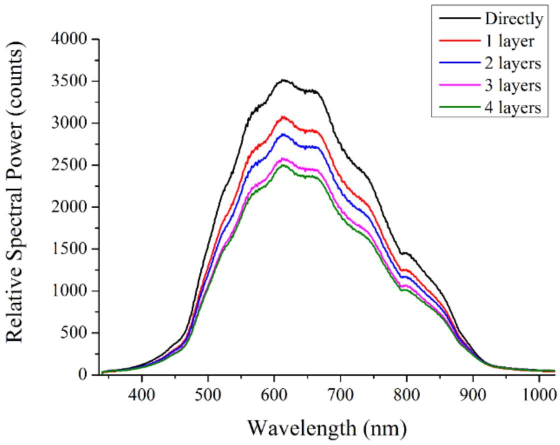

Figure 3-10 Wavelength spectra of incandescent lamp with various layer of filters

The solar cell power output is loaded using a resistance box (Cropico RM6-N decade box with 10 Ω resolution, ± 1% accuracy), the voltage across the load is measured by a 12-bit A/D convertor (NI USB-6008), and the output power density of each solar cell is then calculated as shown in equation 3.1.

$$E_d = \frac{V_{Cell}^2/R_{Load}}{A_{Active}} = \frac{V_{Cell}I_{Cell}}{A_{Active}} \text{ (μW·cm}^{-2}\text{)} \tag{3.1}$$

Where E_d is output power density of the tested solar cell, V_{Cell} is the voltage across the load, I_{Cell} is the output current of the solar cell, and A_{Active} is the active area of the solar cell. Varying the load resistance changes the output voltage of the solar cell. A series of power density values can therefore be measured and plotted to show the output power density against the operation current of measured solar cell. The Maximum Power Point (MPP) [137] of the solar cell is then found by reading the maximum output power density value on E_d/I_{Cell} curve. This maximum power density gives the maximum power per unit area that can be achieved by the corresponding illumination and solar cell combination.

The three white light sources (incandescent, CFL and white light LED) are investigated at three lux levels: 1000 lx representing well illuminated conditions; 500 lx as the normal lighting condition on a desk surface and 200 lx representing ambient lighting. The three primary colours of the colour-controllable LEDs are also investigated but only at 200 lx because of the limited output power of the lamps currently commercially available. The indoor solar cells are operating at the room temperature in the residential building environment in the scenario of human tracking, so all the tests are taken at the room temperature, which is around 25 °C. According to the datasheets, the room temperature is in the range of operation temperature of all the selected solar cell, the effect of the varying temperature within ± 10 °C in the environment is ignorable on the output power of the selected solar cell in these tests. Table 3-5 shows the maximum output power of selected solar cells under 6 different lighting conditions. Indoor artificial light and natural light which shine into the room through a window are both examined to compare the performance of solar cells in a typical office room and the testing conditions, the intensity of natural light is controlled by a blind and measured by ISO-TECH Lux-1337.

Table 3-5 Maximum output power of solar cells in various condition

Maximum output power (mW)	Fluorescent light			Natural light		
	1000 lx	500 lx	200 lx	1000 lx	500 lx	200 lx
MC-SP0.8	0.206	0.076	0.053	38.850	1.332	0.069
AM-5608	0.599	0.413	0.094	11.165	0.761	0.062
AM-1815	0.741	0.482	0.118	6.372	0.969	0.084
Indy4050	0.381	0.245	0.054	5.356	0.479	0.052

This table shows large differences between the amounts of the energy harvested from fluorescent light or natural light for all selected types of solar cells under the 1000 lx illumination level, but similar amounts of the energy under the 200 lx illumination level. The largest different was occurred on MC-SP0.8, when it harvesting energy from the daylight, it harvests approximately 190 times more than what it harvesting from the fluorescent light, according to its datasheet, the module is for the outdoor applications. Overall, all the tested solar cells have the drawback on the output power under an indoor 1000 lx fluorescent light compared with the output power under the same illumination level natural light source, but these gaps are smaller under 500 lx, which are approximately 2 times. For the indoor modules AM-1815, it can harvests approximately 1.4 times power under the fluorescent light than under the natural light.

3.2.2.5 Performances under Different Types of Light Sources

The output power density of each solar cell is measured in the first test under the three white light sources, incandescent, CFL and LED. As the load resistance is varied, the output power density versus the output current of the MC-SP0.8, AM-5608, AM-1815 and Indy4050 under three different illumination sources at 500 lx are shown in Figures 3-11 to 3-14, respectively.

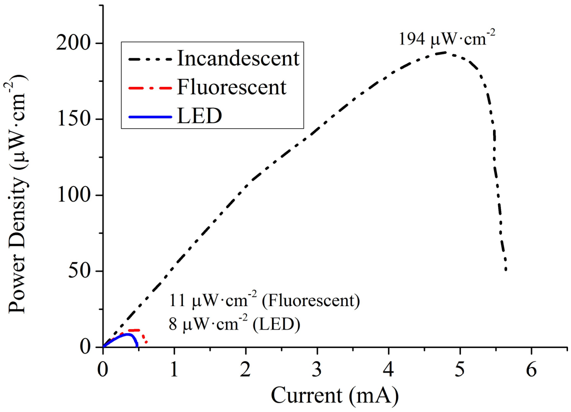

Figure 3-11 Harvested power density at 500 lx for MC-SP0.8

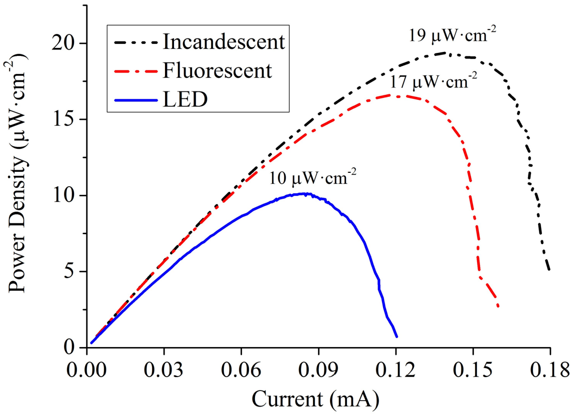

Figure 3-12 Harvested power density at 500 lx for AM-5608

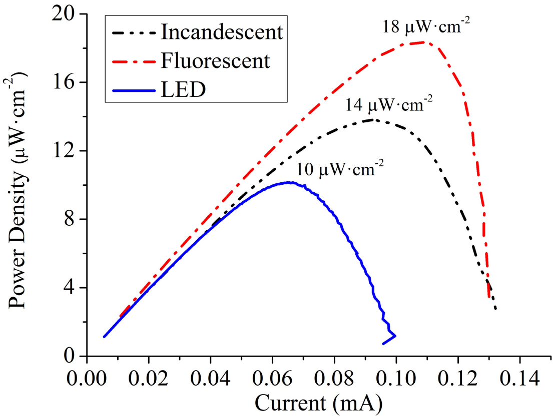

Figure 3-13 Harvested power density at 500 lx for AM-1815

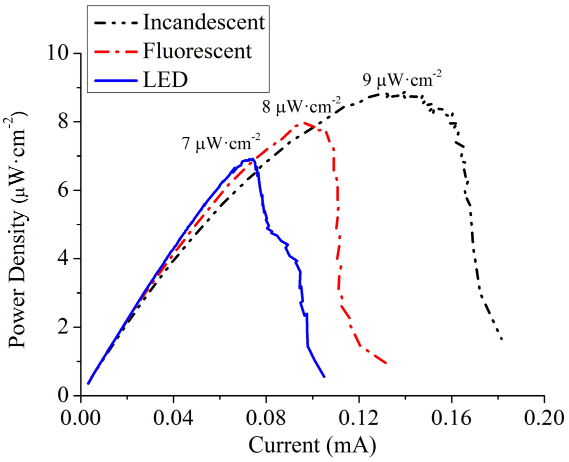

Figure 3-14 Harvested power density at 500 lx for Indy4050

To summarise the results from the tests of the solar cell types under the three white-light illumination sources: the devices exhibit their highest power density under illumination from an incandescent source, with the exception of the AM-1815 which exhibits its optimum performance under fluorescent lighting. These results indicate that the wavelengths at which the different solar cells are sensitive are most prevalent in incandescent light. This is as expected as incandescent light emission covers a wider spectral range than CFL or LED sources which emit over narrower ranges. Further, in the case of CFL, the emission is in a number of bands of wavelengths, as shown previously in Figure 3-4.

Comparing the results for each solar cell under the different illumination sources shows that the output power density of the MC-SP0.8 falls significantly when the illumination is changed from incandescent to CFL (95% reduction) and white light LED (96% reduction). This indicates that the key wavelengths from which the MC-SP0.8 converts the most energy lie outside of the range of emission of the CFL and LED sources. The AM5608 solar cell also shows a drop in power when changing to CFL or LED sources, but with less marked reductions of 10% and 47% respectively. Likewise for the AM1815 the reductions are less than for the MC-SP0.8, however the highest output density is achieved for the CFL illumination rather than incandescent; this is attributable to the spectral sensitivity of the AM1815 being optimised for operation under artificial lighting such as CFLs. Changing from CFL to incandescent and LED lighting causes reductions in maximum output power densities of 22% and 44% respectively. Finally the Indy4050 flexible solar cell has lower output power densities for each light source than all the other types tested, with an average power density 60% lower, although the difference in maximum output density is less than was experienced with the other types of solar cell. Changing to CFL and LED lighting sources causes corresponding reductions in power density of 11% and 22% from that seen with the incandescent source.

Energy harvesting devices do not operate at the MPP all the time since the variation of the environment, such as different illumination levels and types of the light sources for the solar cell. Circuits are available to tracking the MPP, such as simply tracking the output current of the solar cell. The solar cell MPP tracking circuits can operate solar modules at close to the MPP by actively modifying the load, but these circuits require power to operate and so reduce the overall efficiency of an energy harvesting system, for the system development, it is necessary to compare the energy wasted by the MMP tracking circuit and the energy gained by forcing the solar cell operated near the MPP, and then find an optimal solution. In some cases, such as indoor use with low levels of illumination, such system consumes milli-watt or micro-watt power, the available energy and the harvested energy may be constrained to the extent that it is not acceptable or practicable to accommodate the additional energy overhead associated with an MPP tracking circuit. Instead it may be necessary to fix the operational point such that the device is operating close to the MPP under the most commonly encountered operational conditions. In this case it is necessary to use a measure of how well the energy harvester performs when it is not at the ideal load. In this work the range of output currents at which the harvester provides at least 90% of the maximum power density, under the light source of interest, is used to gauge how robust a device is when deployed in different conditions. The output current from each solar module was measured from zero (open circuit) to the maximum current (low load resistance) at which the output power density of the solar cell is less than 10% of that at the MPP. Table 3-6 shows the range of output currents at which the solar cells can generate at least 90% of the power density at the MPP for the illumination source being tested at an illumination level of 500 lx.

Table 3-6 Range of output currents in which each solar cell can generate at least 90% of the MPP power density

Solar cell module	Range of output currents (%)		
	Incandescent	Fluorescent	LED
MC-SP0.8	25.4	28.1	28.8
AM-5608	29.2	28.9	25.1
AM-1815	27.6	20.3	25.8
Indy4050	29.3	22.6	15.2

All the solar cells tested can provide a range of more than 20% of the available output currents in which they harvest solar energy with an output power density of at least 90% of the power density at the MPP, except for the Indy4050 which only achieves 15.2% of the output currents under white light LED lighting. This shows that if the harvester is to operate under LED lighting sources, and it is not practicable to use a MPP tracking circuit, that the other types of solar cells tested should be chosen in preference to the dye-sensitised Indy4050 as they have a wider operating range around their MPP and would perform better in a fixed operating point situation.

The power densities of the solar cells at their MPP are shown in Table 3-7 for the incandescent light source, the fluorescent light source, and the white LED light source. The error bar shown in this table is the standard deviation calculated based on the multiple measurements for 3 times.

Table 3-7 Maximum output power densities of solar cells under various light sources

Power density (μW·cm^{-2})	Incandescent source			Fluorescent source			White LED source		
	200 lx	500 lx	1000 lx	200 lx	500 lx	1000 lx	200 lx	500 lx	1000 lx
MC-SP0.8	101 ±4.2	194 ±8.1	566 ±23.8	3 ±0.1	11 ±1.5	30 ±1.3	3 ±0.1	8 ±0.3	25 ±1.1
AM-5608	6 ±0.3	19 ±0.8	72 ±3.0	4 ±0.2	17 ±0.7	37 ±1.5	4 ±0.2	10 ±0.4	29 ±1.2
AM-1815	5 ±0.2	18 ±0.8	38 ±1.6	4 ±0.2	14 ±0.6	37 ±1.5	3 ±0.1	10 ±0.4	27 ±1.1
Indy4050	5 ±0.2	9 ±0.4	24 ±1.0	3 ±0.1	8 ±0.3	13 ±0.5	2 ±0.1	7 ±0.3	19 ±0.8

Under the incandescent light source, the MC-SP0.8 performs best at all illumination levels, with an output power density 8 to 23 times greater than the other three solar cells. The output power densities of the MC-SP0.8, AM-5608 and AM-1815 are similar under fluorescent and LED light sources. However the Indy4050 can only generate 35% of the output power density of the AM-5608 and AM-1815 under fluorescent lighting at 1000 lx, and 66% of the AM-1815's output power density under the white LED at 1000 lx. The Indy4050 does achieve similar performance to the other three devices under fluorescent and LED light sources at 200 lx so could be used at lower illumination levels without sacrificing efficiency compared to the other devices.

To illustrate the need to match the spectral sensitivity of the solar cell used to the spectral composition of the intended light source a measure of the overlap between the source spectra and solar cell sensitivities has been made.

A measure of the suitability of the three materials (poly-crystalline silicon, amorphous silicon and dye-sensitised) for use with each of the four light sources was obtained by the following steps:

1. The relative spectral power of the selected light source is measured with the spectrometer (Ocean Optics USB2000) to obtain the relative power at 0.38 nm increments and the resulting spectra is then normalised to the maximum value for the spectra in question. This is repeated for each of the light sources with the same lux level on the illuminated target surface.
2. Normalised sensitivity values for the crystalline and amorphous silicon solar cell are taken from the Panasonic datasheet (Panasonic. 2014). The values for the dye-sensitized solar cell sensitivity are taken from the datasheet of the Indy4050 from G24i (G24i. 2011). A line of best fit is made to these points and used to generate spot values at 0.38 nm intervals to match those from the illumination source spectral data.

3. The summation of the overlap area between the sensitivity plot for a given material and the relative spectral power plot for a given light source over the range 340 nm to 1023 nm is calculated using equation 3.2.

$$\sum_{\lambda=340\,nm}^{1023\,nm} P_{Light}(\lambda) \times S_{Cell}(\lambda) \times \Delta\lambda \tag{3.2}$$

Where P_{Light} is the normalised relative spectral power of the light source (measured as photon counts by the spectrometer), S_{Cell} is the normalised sensitivity of the material (from the manufacturer's data), and λ is the wavelength of the light.

Figure 3-15 shows an example of the overlapping area between the relative spectral power distribution of the incandescent light source and the sensitivity of the poly-crystalline silicon material. The size of the overlapping area provides a guide to the alignment between the source and solar cell's spectra with a larger overlapping area indicating a better match between source and receiver and a lower area indicating a poorer match. The more coincident the two spectra are, the larger the overlapping area size figure will be and therefore the more efficiently the solar cell will work.

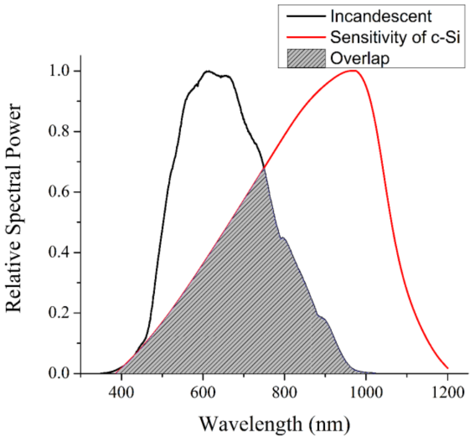

Figure 3-15 Overlapping area between incandescent spectral distribution and poly-crystalline silicon sensitivity

Using this process, the values of the overlap areas between three solar cell materials and four different light sources are calculated and shown in Table 3-8. The percentage of the area of the light source spectra which overlaps with the material sensitivity spectra area is shown in Table 3-9.

Table 3-8 Overlapping area between materials and light sources

Material	Source				Sensitivity Total Area
	Incandescent	CFL	LED	Natural Light	
Poly-crystalline silicon	164	26	33	104	427
Amorphous silicon	217	95	99	245	321
Dye-sensitized	182	100	94	236	283
Source Total Area	328	115	109	318	

Table 3-9 Proportion of light source area covered by material sensitivity area

Material	Source			
	Incandescent	CFL	LED	Natural Light
Poly-crystalline silicon	50.0%	22.6%	30.3%	32.7%
Amorphous silicon	66.2%	82.6%	90.8%	77.0%
Dye-sensitized	55.5%	87.0%	86.2%	74.2%

The data in these tables can be used to specify the optimum solar cell for use with a specific light source by selecting a solar cell type which covers the highest percentage of the light source spectral range.

From the data in Table 3-9 it can be seen that the solar cell type best matched to the source spectra of incandescent, white LED and natural light sources is amorphous silicon, whilst dye-sensitized is best matched to CFL. It should be noted that these values are based on normalised sensitivity spectra for each material. This information cannot be used to give absolute output power values as the conversion efficiency of the different materials needs to be taken into account. Also this indicative approach assumes equal energy weighting at each wavelength within the spectra, which is another topic beyond the scope of the work in this thesis.

3.2.2.6 Performances under Different Spectral Ranges

To assess the effects of the different source spectra provided by the colour controllable LED, the performance of the solar cells under illumination with a selection of different spectral ranges has been measured. These tests measured the output power densities from the solar cells under only the red, green or blue primary colours from the colour-controllable LED. As this new kind of light is designed to change the colour of an environment for entertainment or recreational purposes, it has limited power. Only 200 lx can be achieved by any one of the three primary colours in the lamp tested. To achieve illumination levels of 500 and 1000 lx, it would be necessary to use more than one such colour-controllable LED unit. Of course this will not change the spectral distribution of the LED light source, only the scale of the power density.

The outputs of the MC-SP0.8, AM-5608, AM-1815 and Indy4050 under each colour at 200 lx are shown in Figures 3-16 to 3-19, respectively.

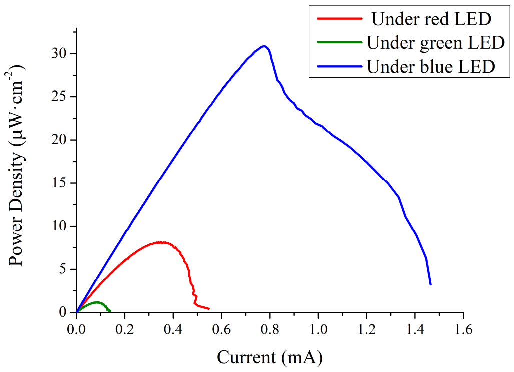

Figure 3-16 Harvested power density at 200 lx for MC-SP0.8

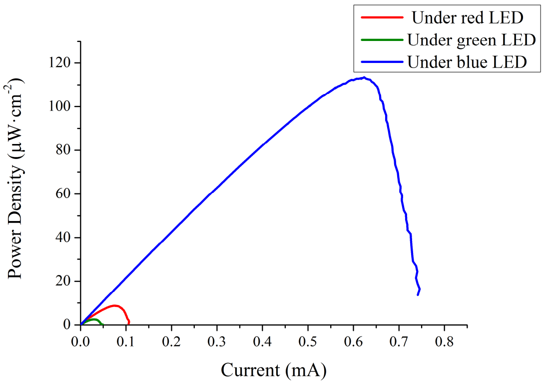

Figure 3-17 Harvested power density at 200 lx for AM-5608

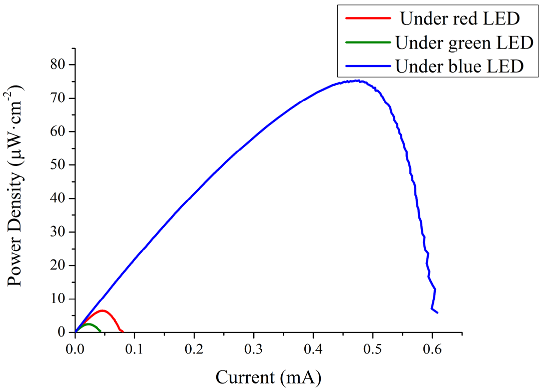

Figure 3-18 Harvested power density at 200 lx for AM-1815

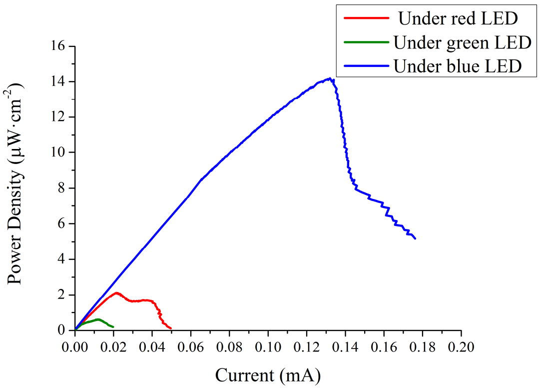

Figure 3-19 Harvested power density at 200 lx for Indy4050

Table 3-10 shows the output power densities of the solar cells at their MPP under the three primary colours from the colour-controllable LED compared with the same illumination level from the white LED.

Table 3-10 Maximum output power densities (μW·cm^{-2}) of solar cells under 3 colours of LED at 200 lx

Solar cell module	**Maximum output power densities** (μW·cm^{-2})			
	Red	**Green**	**Blue**	**White**
MC-SP0.8	8	1	31	3
AM-5608	9	3	113	3
AM-1815	6	2	75	4
Indy4050	2	1	14	2

Under the blue illumination, all the solar cells provide a higher output power density than green and red (7 – 38 times) at 200 lx. This is attributable to the lux levels used being referenced to the human eye's wavelength sensitivity and the corresponding lower sensitivity exhibited by the eye to wavelengths in the blue region. Therefore to give the same perceived illumination and lux level a greater level of light energy is needed.

3.2.2.7 Selection of solar cell

Indy4050 has a double size version of it named Indy4100. An Indy4100 has the same material and characteristic as Indy4050, it can output up to 108, 510 and 761 μW power under the fluorescent light at illumination levels of 200, 500 and 1000 lx, respectively. Under the natural light at same levels, the powers it can output are up to 120, 690, and 1020 μW, respectively. Indy4100 has three advantages compared with the AM1815, AM5608 and MC-SP0.8, even it has the lowest power density.

(1) The power output of Indy4100 is stable when the light source is switching between artificial and natural light. The indoor AM1815 power output is 4 mW less than the Indy4100 when they are operating under natural light conditions. The outdoor AM5608 power output is 0.2 mW less than the Indy4100 under fluorescent lighting. Therefore, in a daily office room which the light source is a mixture of natural and fluorescent light, the output power performance of Indy4100 is better than other solar cells tested in this section.

(2) The MPPs of the Indy4100 output voltages under various tested conditions are all around $1.95\,\mathrm{V} \pm 0.15\,\mathrm{V}$, whereas other solar cells have a larger range of MPP from 2 V to 4.39 V. Energy extraction circuitry remains the output voltage in the level of the MPP of the harvester that making it work efficiently, by switching on to allow the harvester charging the following circuit when the output voltage of the harvester is equal or higher than the MPP or switching off to regain the output voltage when it is lower than the MPP. So the energy extraction circuitry for the other solar cells tested in this section need a custom design that has a changeable threshold voltage base on the ambient lighting condition. This aim complicates the circuitry design and it also requires energy when it is changing the voltage. The extraction circuitry for the Indy4100 can set one threshold voltage at 2.1 V, that is around the MPP when the Indy4100 under all the tested lighting condition. Fixed threshold voltage extraction circuitry uses fewer components than changeable one that also cost less energy.

(3) The Indy4100 is flexible and suitable for a curved surface, so it can get a wide range of light sources from different angles.

There reasons cause the G24i dye sensitised indoor photovoltaic module Indy4100 to be selected as the light energy harvester in this system.

3.2.3 Micro Controller and Radio Transceiver

The selections of the Micro Controller Unit (MCU) and radio transceiver are very important since this block provides the processing, controlling and communicating in the system, and also consuming the most fraction of the power in the system which with a passive sensor. For an energy harvesting device, the low power consuming MCU and radio transceiver, which with the essential functionalities, are preferred as a low power output will be required from the energy harvester, which compared with a powerful MCU or a speedy transceiver with unnecessary high performance but consuming larger power than the preferred system. A low power requirement means that a small size of the energy harvester can be employed under the same ambient energy density. There are two options for the design of this block: Dual-Chip and System-on-Chip [138]. Dual-Chip consists of a separate MCU and radio transceiver, whereas System-on-Chip, also named as Single-Chip, integrates the radio transceiver with the MCU in a single IC. The function of the MCU and the transceiver are same in either design.

The operational requirements of the MCU in this system to control its operation are:

- 1 external interrupt input port is used to receive the signal from PIR sensor;
- 6 I/O ports are used to communicate with radio transceiver that sends a message after a movement has been detected;
- 2 I/O ports are used to control booster and latch circuits;
- Low Power Mode (LPM) that can wake up from sleep state by an external interrupt sending from PIR;
- An analogue input port is used to measure the voltage of supercapacitor which represents the energy storage level.

The radio transceiver consumes a large fraction of total energy dissipation. It is important that the radio transceiver has low (micro watt level or less) or zero power consumption in its sleep mode, and also low power consumption in its IDLE, transmit (TX) and receive (RX) modes. To minimize the power use of the MCU while the radio is starting up, it needs a minimal delay on wake up.

The radio transceiver applied in this research should be equipped in terms of admissible transmitting channel, suitable range and sufficient data rate. The 2.4 GHz channel frequency has been chosen as the international standard for wireless communication and especially used in low-power embedding applications worldwide. The communication scope of this demonstrator device is within 10 m, which is a normal distance between two nodes in one building. One 200-bit packet could be sent in 1ms when the data rate reaches 250 kbit/s. When the period for which the transceiver working in TX mode is minimised, it reduces the total energy consumption.

If the data rate is much higher than an ideal speed, it will require more power, and is unnecessary when a small packet is transmitted in this application. A 200-bit packet is sufficient to contain both the data packet frame and the measured data, including the voltage of supercapacitor, the voltage of MCU power supply and ambient temperature data. The data packet frame is required for the transmission protocol.

One difference between Single-Chip and Dual-Chip solutions is that the radio transceiver integrated in the Single-Chip solution can wake up more quickly than the Dual-Chip one. Assuming the System-on-Chip solution and the Dual-Chip solution have the same software processing in different hardware, the maximum power consumptions would greater in the Dual-Chip transceiver due to the extra turn-on time.

According to the datasheets [139-143], the maximum power consumption of TX mode is 10,000 times of the power of IDLE mode, so the power is mainly consumed by radio transmitting in each hardware solution, the power consumption in IDLE mode is negligible in the comparison of their power consumption. For the system design, the maximum power consumed by MCU and radio receiver is considered and compared, it is used to evaluate the system with different hardware but same programming, i.e. duty cycle, as the average power the system consumed can be established that the maximum power is the only major variable. Table 3-11 shows the datasheet power consumption of some commercial available solutions which have been investigated, in the Dual-Chip solution, the powers consumed by both MCU and radio transceiver have been added to compare with the SoC solution.

Table 3-11 Comparison of maximum power from commercially available solutions

Manufacturer	Type	MCU model	Transceiver model	Maximum Power (mW)
Texas Instruments	Dual-Chip	MSP430F2274	CC2500	38.65
	System-on-Chip	CC2430	N/A	48
MICROCHIP	Dual-Chip	PIC16LF1503	MRF24J40	55.2
ATMEL	Dual-Chip	ATtiny20	AT86RF231	28
	Single-Chip	ATmega128RFA1	N/A	29

MCUs details that are important to low power function in this context are listed in Table 3-12. PIC16LF1503 from MICROCHIP has the lowest active mode current, the lowest sleep mode current and the widest supply voltage range.

Table 3-12 Parameters of MCUs

MCU	MSP430F2274	PIC16LF1503	ATtiny20
Supply Voltage (V)	2.2-3.6	1.8-3.6	2.7-5.5
Active Mode Current (mA) @8MHz	2	0.7	3.2
Sleep Mode Current (µA)	0.1	0.02	0.15
Time to Wake Up from Sleep Mode (µs)	1	8	10
No. of I/O	32	12	12

Table 3-13 lists the details of radio transceivers that are considered to be important parameters for the system. The operating frequency of these transceivers is 2.4GHz. AT86RF231 from ATMEL has the lowest TX mode current, the lowest sleep mode current and he widest supply voltage range.

Table 3-13 Parameters of radio transceivers

Radio Transceiver	CC2500	MRF24J40	AT86RF231
Supply Voltage (V)	1.8-3.6	2.7-3.6	1.8-3.6
TX Current @0dBm output power (mA)	15	120	11.6
Sleep Mode Current (µA)	0.9	12	0.02
Delay time form Sleep to Active (ms)	0.24	2200	0.33
RX Sensitivity (dBm)	-87	-108	-101
Data Rate (k bps)	1.2-500	250	250-2000

Table 3-14 lists the details of the System-on-Chip solution.

Table 3-14 Parameters of System-on-Chip solution

System-on-Chip Solution	CC2430	ATmega128RFA1
Supply Voltage (V)	2.2-3.6	1.8-3.6
TX Mode Current @0dBm output power (mA)	26.9	10
Sleep Mode Current (µA)	0.2	0.25
Delay Time from Sleep to TX (ms)	0.5	0.24
RX Sensitivity (dBm)	-98	-100
No. of I/O	21	38

From the potential solutions investigated, the device from ATMEL requires the least power to operate.

If a MCU and transceiver from different companies can be used, the PIC16LF1503 working with an AT86RF231 will be the best choice based on the power consumption parameters from the datasheets. But by using an evaluation board, it saves the time from design and testing the PCB board for MCU and radio transceiver, therefore, within this demonstrator device the EZ430-RF2500 evaluation board has been selected as MCU and transceiver. This evaluation board is designed and tested by Texas Instruments company, and consist the MCU MSP430F2274 and transceiver CC2500. It is not the best solution for the system, but when using a better solution for the system than this evaluation board, the overall power consumption performance of this system will be improved.

3.2.4 PIR Sensor

There are two types of PIR sensor devices that are commercially available; One is a pyro electric sensor that converts the infrared signal to an analogue voltage signal, while the other has the necessary functions integrated with sensor in a single IC. These integrated functions include a band pass filter for noise reduction, amplification circuits, a signal adaptor and an ADC converter [144]. The advantages of an integrated signal conditioning circuit within the same package include small package size, excellent noise resistance and a reduction in development time by skipping signal conditioning circuitry design and testing.

Table 3-15 shows some commercially available PIR sensors along with their key parameters.

Table 3-15 commercial PIR sensors

Company	Panasonic EW		IR-TEC	MURATA
PIR Model	EKMB1103 series	AMN 41121	MS-112LP	IRS-B series
Type	Integrated	Integrated	PIR sensor with signal conditioning circuit	PIR sensor without signal conditioning circuit
Supply Voltage (V)	2.3-4.0	2.2-3.0	2.4-3.6	3.2
Sleep Mode Current (μA)	1	46-60	10	N/A
Maximum Output Current (μA)	100	100	50	N/A
Diameter (mm)	22 × Ø20	14 × Ø9.5	34 × 13.5 × 9.5	4.7 × 4.9 × 2.4
Appearance			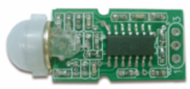	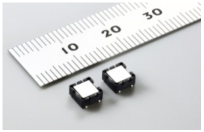

The power consumption of a PIR sensor without signal conditioning circuitry is close to zero because it converts directly from thermal energy to electric energy. The current consumption and stability of the output signal of this sensor depends on the conditioning circuitry design. Design considerations include components like a high gain operational amplifier and the design of a low noise PCB, the integrated PIR sensor has advantages on the noise reduction which is the most concerned. Overall, the EKMB1103 PIR sensor is selected as the movement detector in the system because of its low power consumption and digital signal output.

3.2.5 Summary

The Indy 4100 solar cell by G24i selected as the PV module because of its shell flexibility and output voltage stability. The MSP430 development kit ez430-rf2500, which consists of an MSP430F2274 and CC2500, is selected as the micro controller and transmitter system. An EKMB1103 PIR is selected as the sensor to detect the movement because it consumes the lowest power and has the signal conditioning circuit integrated.

The PIR sensor operates at 2.2 V and draws 1 µA when it is sleeping, and when a movement detected, it draws 100 µA for approximate 50 ms to generate a digital toggle signal. Assuming that movements are detected every 5 s in 24 hours, the PIR sensor will consume 2.3 µW on average. The overall power that the MCU, transmitter and PIR sensor requiring is less than 105 µW on average. When the efficiency of power subsystem is 70% [145], the 150 µW power is required in 24 hours. Since the light source is generally available over 10 hours from 7 am to 5 pm, the output of solar cell should be at least 360 µW. One Indy4100 solar cell can power the system when at least 500 lx is available from either natural or artificial lighting. If the light level is less than 500 lx, the system will require more than one solar cell to provide sufficient energy.

3.3 A PIR Wireless Sensor

This section presents the design details of the demonstrator device that consists of the hardware and software subsystems. The hardware part includes the circuitry design, PCB design and shell design. The software part is the programming of Micro-Controller Unit (MCU).

3.3.1 Hardware Design

The hardware design includes three blocks: power subsystem circuitry design, MCU and transmitter circuitry design and PIR output signal circuitry design, there are shown in Figure 3-1. As mentioned in section 3.2.5, the MCU and transceiver use an evaluation board ez430-rf2500, so the circuit design uses the interface ports based on the usage of ports in software. The PIR sensor is integrated with the signal conditioning circuit, so it can be connected to a digital input port of the MCU directly. Therefore the circuit design of the power subsystem is the main part of the hardware design process.

Figure 3-20 shows a block diagram of the power subsystem. The flexible solar cell converts the energy of light into electricity, which is less than 1 mW power in 900 lx when it operates near its MPP voltage. Connecting a solar cell directly to the system will force it to operate far from its maximum power point voltage. A voltage supervisor acts to maintain a constant voltage across the input terminals of the voltage supervisor in order to keep the solar cell at a voltage set by the integrated voltage reference, this voltage is maintained around the MPP by disconnecting the circuits between the solar cell and the supercapacitor when the voltage drops down under 2.0 V. This 1 mW power needs a buffer to store enough energy to charge the supercapacitor, while the switching frequency of the voltage supervisor can be reduced. The supercapacitor stores the energy for the requirements of 24-hour work a day, which involves working in the dark without any charge for 14 hours at least. To increase the range of the output voltage of the supercapacitor, a booster circuit used to boost the voltage to the 2.2 V required by the MCU, transmitter and PIR sensor.

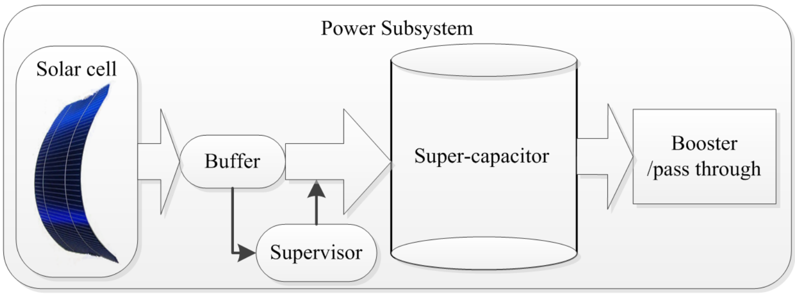

Figure 3-20 Power Subsystem block diagram

Figure 3-21 shows the schematic circuit diagram of the voltage supervisor and booster. The solar cell can connect to the PV_IN and PV_VSS ports to join up with the buffer capacitor C1, and is supervised by TC54VC voltage detector to keep its operation near its MPP voltage. A BAT54C diode inhibits the reverse flow of current from the supercapacitors when the solar cell is not exposed to sufficient light [146]. Within the circuit, C2 and C3 are the 10 F 2.5 V supercapacitors in series which give an overall capacitance of 5 F, and it can operate under 5 V to store the energy absorbed from the solar cell, which is high enough for the maximum output voltage of solar cell. R1 and R2 scale the voltage of the supercapacitor to the voltage of the range of MCU ADC function. Booster circuitry fixes the output voltage of energy store at 2.2 V to operate the micro processer [145].

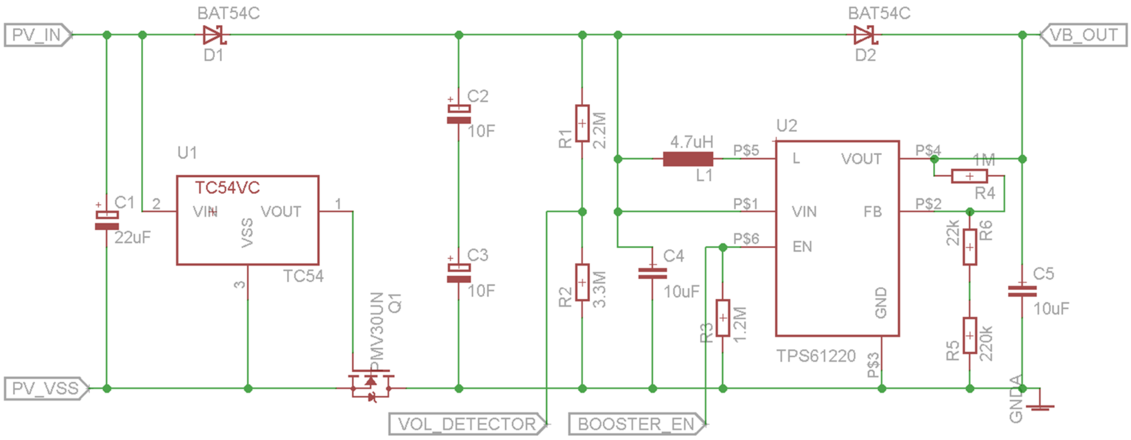

Figure 3-21 Circuitry design of power subsystem

Within the design, several ports can be connected or disconnected to allow the testing of each individual sub circuit, for instance, solar cell extraction circuit can be isolated from supercapacitors, and supercapacitors can be isolated from the boost circuit.

Figure 3-22 shows the waveform when the solar cell is charging supercapacitors. Channel 2 is the output voltage of the solar cell and buffer capacitor and channel 3 is the voltage of supercapacitors. When the output voltage of the solar cell reaches 2.1 V, the voltage supervisor connected it to supercapacitors, the voltage then falls down as the charge is transferred from the buffer capacitor to supercapacitors. When the voltage falls below 2.0 V, the supervisor opens the connection, then the solar cell charges the buffer capacitor again. The voltage hysteresis of from 2.0 V to 2.1 V can also reduce the switching frequency. When the voltage of supercapacitors increases above 2.2 V, the booster stops boosting the voltage, and a schottky diode D2 allows energy pass through with less than 340 mV forward voltage decrease.

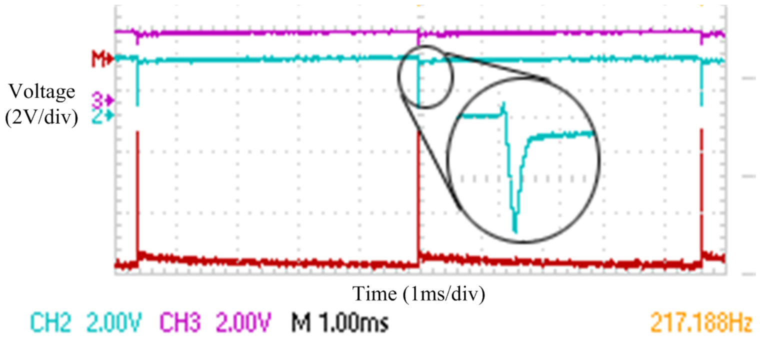

Figure 3-22 Waveform of solar cell charging process

The waveform of the output voltage of the booster is shown in Figure 3-23. The maximum voltage fluctuation is 104 mV observed and measured by the oscilloscope, this fluctuation is caused by the boosting IC and within the range claimed in its datasheet, according to the datasheet of the MCU, this fluctuation is acceptable to the MCU power supply [50]. The frequency of this noise is around 1.7 Hz that is safe to the 2.4 GHz wireless communication channels.

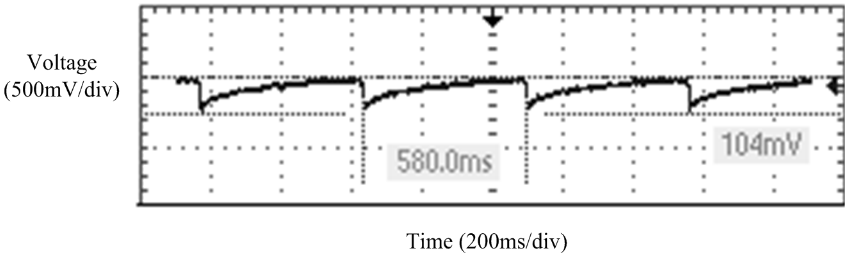

Figure 3-23 Waveform of boosting

Voltage protection circuitry is important in wireless sensor node applications for two reasons. Under-voltage events can cause the MCU to turn on erroneously in an undefined state and drain power from the store, and overvoltage situations can cause permanent damage to components in the system. The block diagram of the voltage protection is shown in Figure 3-24. The voltage of supercapacitors is monitored by both the MCU and the voltage detector. The voltage detector only connects the circuit from power supply to the MCU once the supercapacitors have sufficient energy to start up the MCU. After the MCU starts up, the voltage of supercapacitors is monitored by the MCU to determine the amount of energy stored, and this is used to estimate its remaining living time. The solar cell might harvest more energy than the capacity that the designed supercapacitor having, an extra supercapacitor for storage is not an option since the size of the device is limited, to prevent overvoltage events, the MCU will add more loads such as a blinking LED to consume the surplus energy.

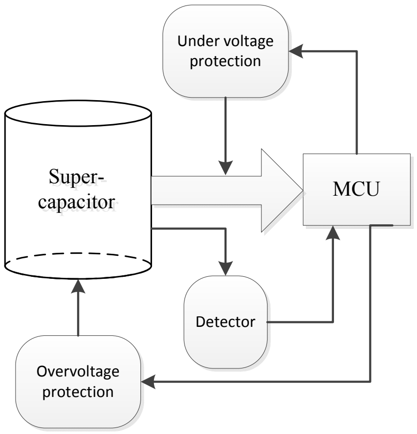

Figure 3-24 Voltage protection block diagram

As shown in Figure 3-25, a 2.1 V voltage detector IC TC54VC feeds through to FETs Q3 and Q4 which interrupt the supply connection of the MCU, should the output voltage of the booster fall below 2.1 V. The voltage detector has built-in hysteresis to mitigate issues with repeated switching. A control signal (VCC_MCU) makes a latch to ensure the supply voltage is stable when the MCU starts up.

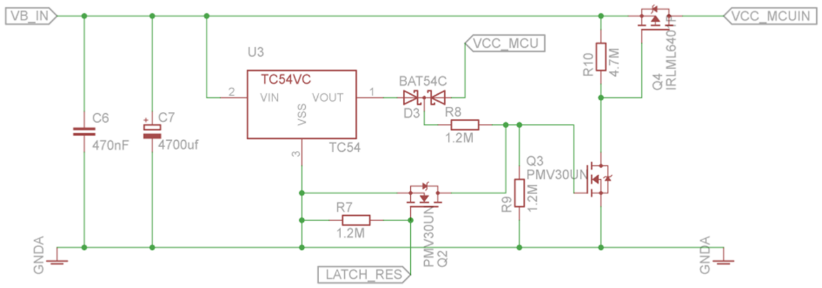

Figure 3-25 Circuitry design of voltage protection

Figure 3-26 shows the waveform of this process such that channel 1 shows the output voltage of the booster, this channel is the output of voltage detector, and channel 3 is the power supply of MCU.

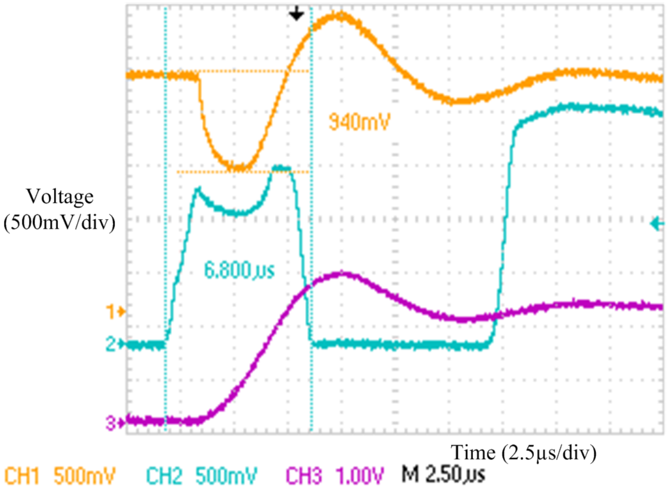

Figure 3-26 Waveform of voltage output of latch when system start up

Figure 3-27 shows the waveform of the voltage spike when the system starts up, this consumes 20 mW in 5 µs, and then the MCU switches to LPM. Channel 2 shows that the booster boosts the voltage to 2.2 V after the MCU start-up, which prevents a peak amount of power required if the MCU and booster start at same time.

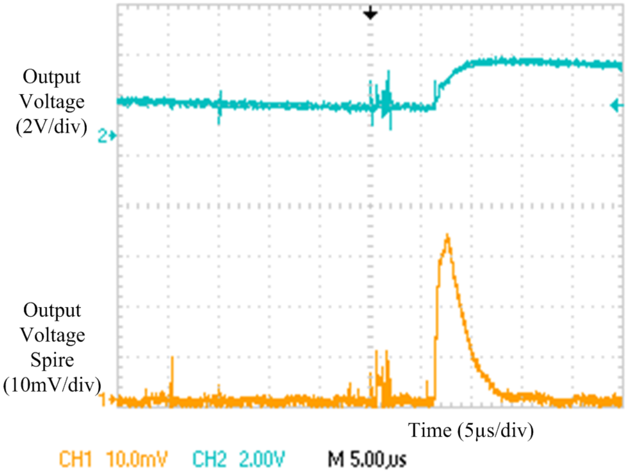

Figure 3-27 Waveform of spire when system start up

The same voltage source is designed for the MCU and PIR sensor to avoid offset voltage between them.

The interface of the evaluation board ez430-rf2500 provides the following ports:

- The VCC_MCU is the power supply port for the MCU.

- The PIR_OUT port links the PIR to the MCU directly.
- The VOL_DETECTOR connects the ADC port of the MCU to supercapacitors.
- The BOOSTER_EN links the enable pin of booster to turn the booster on or off.
- The LATCH_RES port controls the latch circuits.

For testing the system, JP4 and JP6 give two external I/O ports to communicate with the MCU on the board. The SW00 and SW01 connect to switches to change the MCU operation mode manually. The schematic for the connection from each of these blocks to the MCU is detailed in Table 3-16. GDO0 and GDO2 are connected to CC2500 internally to the evaluation board; other ports are connected to the custom PCB via 18 pins.

Table 3-16 MCU ports description

Label	Port	Description
VCC_MCU	AVCC, DVCC	Power supply
PIR_OUT	Digital input port (P2.0)	PIR sensor signal
LATCH_RES	Digital input port (P2.4)	Latch circuitry reset
VOL_DETECTOR	Analogue input port (P2.1)	Energy storage measurement/feedback
JP4 and JP6	Analogue input/output ports (P2.2, P4.4)	Testing ports
SW00 and SW01	Digital input ports (P4.5, P4.6)	Manual mode selection
GDO0 and GDO2	Digital input/output ports (P2.6, P2.7)	Communication ports for CC2500 transceiver

A double sided PCB layout is designed using the CAD software EAGLE, and then manufactured by PCB-POOL. The size of this board is 60.8 × 43.2 mm. The 3D model of the shell for system is designed using CAD software Inventor, and then printed by OBJET 3D printer. It uses the rubber-like material Tango+ DM_9895/9795 which is suitably hard for a shell of a device that needs to hang on the wall. A rotor shaft is designed for changing the angle of the face of solar cell so that it can gain maximum light energy where it installed. The arc of the solar cell tank is also designed to maximise the light energy available from the environment. The size of the whole device is 82.8 × 97.2 × 67 mm.

This demonstrator device is installed on the wall of an office for the system testing that is discussed in section 3.4.2, as shown in Figure 3-28. A fluorescent fitting is as far as 300 mm away from the surface of the solar cell, such that it is exposed to 600-700 lx light energy while this light is on.

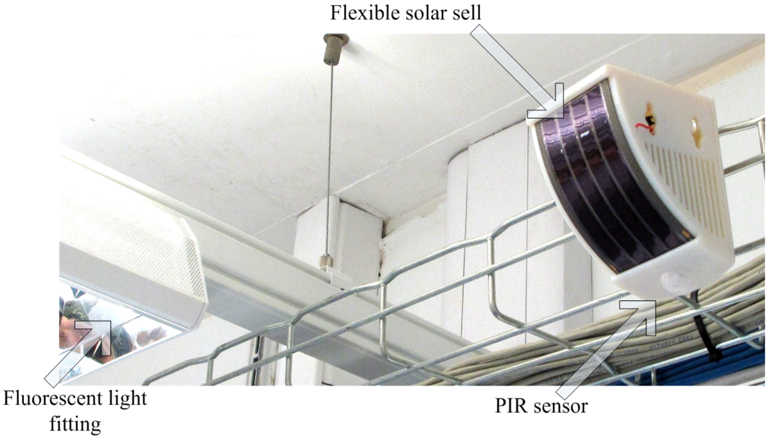

Figure 3-28 PIR wireless Sensor in office environment

3.3.2 Embedded Software Design

The embedded software of the demonstrator device incorporates an initialization function for hardware and an Interrupt Service Routine (ISR) for the signal from the PIR sensor as described in section 3.1 and shown in Figure 3-29. Actions such as adding load when the output voltage of supercapacitors is over the full charge level, or shutting the system down when the energy store is emptied are taken into account in the system state mode amending process. The contents of the message packet can be changed depended on the energy store level, for instance, the message packet can be reduced in size when the energy is insufficient to send a complete packet. The sleep timer in LPM can be fixed as setting the MCU and transceiver to sleep until the system gets sufficient energy.

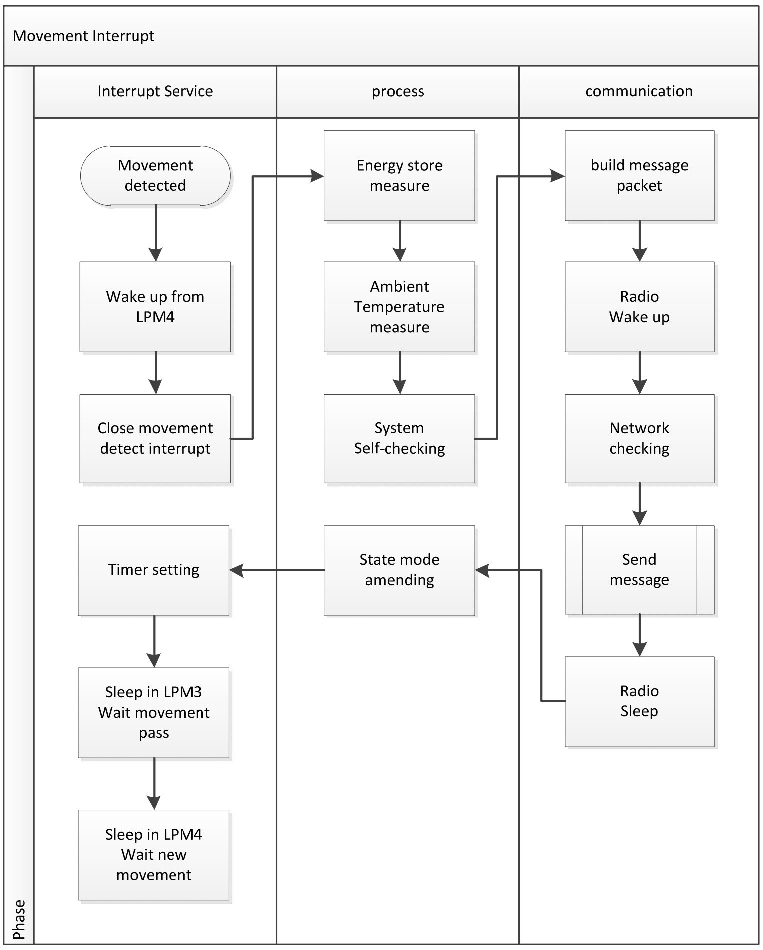

Figure 3-29 Program flow of the interrupt service routine

When sending a message, MCU wakes up the transceiver and transmits a packet via the network that was initialized when the system started up in broadcast. The structure of wireless communication packet within CC2500 can be configured and consists of the following items:

- $8 \times n$ bits preamble
- $16/32$ bits synchronization word
- 8 bits length field or constant programmable packet length
- 8 bits optional address byte
- $8 \times n$ bits payload
- 16 bits optional cyclic redundancy check (CRC)

To limit the power consumption when the radio is working in the TX mode, the time taken to send the message is reduced by adjusting the packet as shown in Figure 3-30.

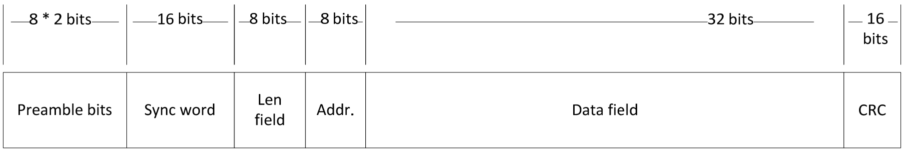

Figure 3-30 Structure of wireless communication packet

The information for the Building Management System (BMS) is written in the data field before the packet is sent. Within the data field, the 32 bits of payload data include 12 bits representing the ambient temperature measurement, 12 bits representing the voltage of storage supercapacitors and 8 bits representing the voltage of supply.

When a base station receives the message, it takes the data field from the wireless communication packet as a string via its CC2500. Then, the base station communicates to the PC using a standard RS232 serial link. The structure of this packet is shown in Figure 3-31.

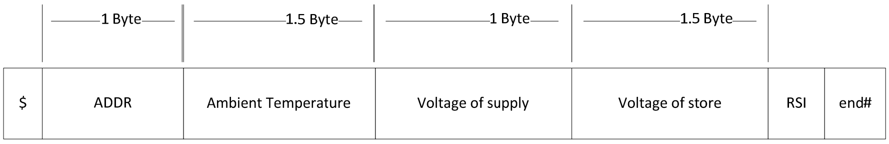

Figure 3-31 Structure of RS232 packet

A custom program on the PC receives the packet and converts the string to the values of ambient temperature, voltage of supply and voltage of store in supercapacitor. Since the string has a fixed length and follows a pre-set format, the decimal points and units for the data can be cut to reduce the length of the data packet and save the time on communication, such as 345 in one Byte voltage of supply means that the supply voltage is 3.45 V. After the explanation of the received string, this custom program shows the movement signal and information of the time stamp, ambient temperature and energy storage in a GUI, and it also records the data in a database for analysis of the performance of the system. This program is a simple one to demonstrate that a centre point can read the information in real time, a more advanced building management control centre can use the information in a more complicated way but that is outside of the scope of this investigation.

3.4 Practical System Testing

3.4.1 Worst Case Scenario

When a movement is detected, the PIR sensor sends a rising edge as shown in channel 2 of Figure 3-32, then the processes of system wake up and transmission causes the voltage of the power supply to drop slightly (less than 30 mV). Including the delay of the system waking up, it takes less than 46 ms for the system switching from LPM to TX, which meets the real time requirements of a normal human tracking system.

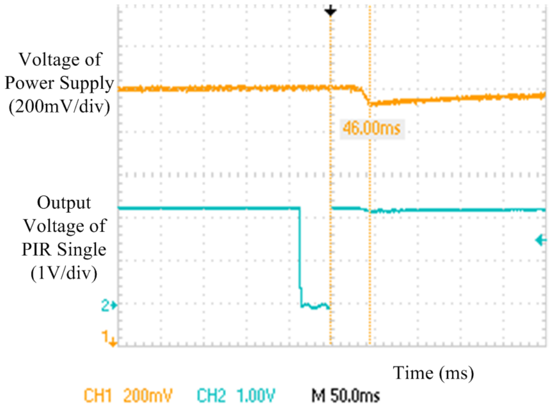

Figure 3-32 Waveform of voltage drop when transmitting

For testing the amount of time that the system can operate without energy input, the system disconnects the solar cell after the output voltage of supercapacitors reaches 2.3 V, the PIR sensor measures a movement every 5 s and then the radio transmitter sends a message to base station every 25 s. The ambient temperature is around 25 °C.

Figure 3-33 shows the output voltage of supercapacitors in 4 tests, and average power consumption is less than 140 µW in each case.

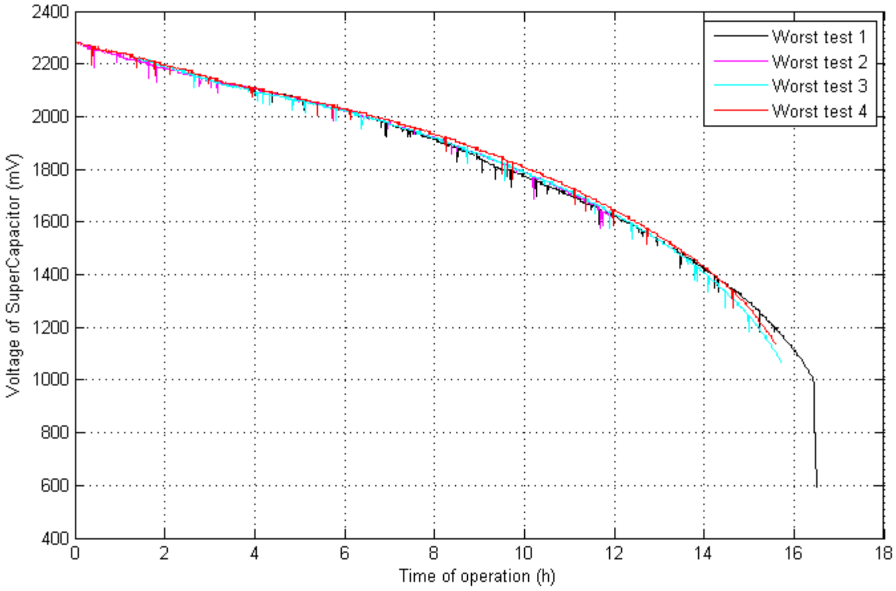

Figure 3-33 Output Voltage of supercapacitor when system operating without energy input

According to the result of this test, it is verified that the system can work no less than 16 hours without any energy input, this result confirms that the calculated capacitance can supply the energy for the system operation more than 14 hours as design.

3.4.2 Normal Scenario

In the normal scenario, the device is installed in a normal office environment such that the PIR sensor faces in to a passageway, more than 500 lx light from fluorescent fitting during 7 am to 5 pm mixed with natural light from 2 pm to 4 pm is on the surface of solar cell, and the environment temperature is around 23 °C. Sensed movements are randomly occurred approximately every 5 minutes during the tested days. The detector will report movements to a base station that is connected to a PC to record along with the voltage of the storage supercapcitors as shown in Figure 3-34.

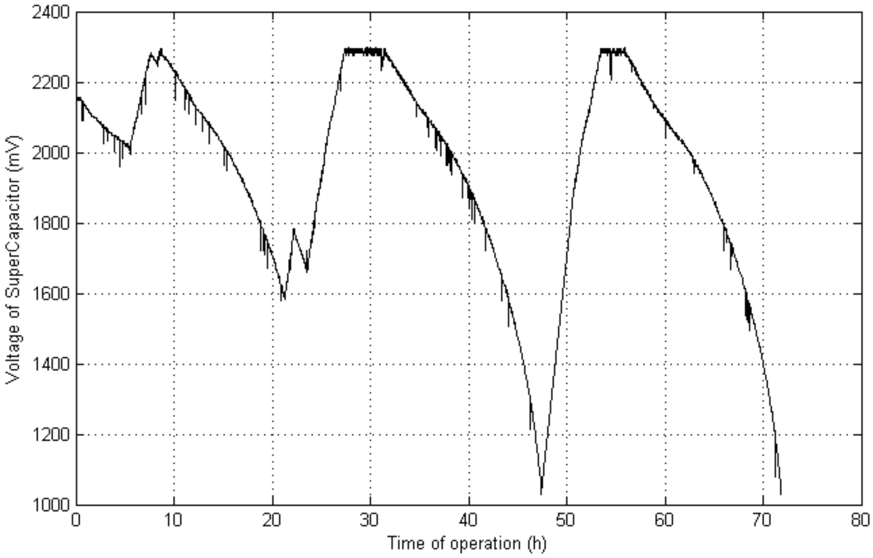

Figure 3-34 Output voltage of energy storage within the detector

This device operates functionally for 72 hours, this figure clearly shows the charge-discharge cycle of the supercapacitor, and when the voltage reaches the limited level, the system controls the load to prevent damage to the components.

3.5 Conclusions

The device with a passive PIR sensor and average power costs in the range from decades micro watt to hundreds micro watt, such as the PIR detector demonstrated in this chapter, can be powered by ambient light energy source wirelessly to relieve the restrictions from mains cables or batteries. The function and power consumption of its main components was discussed in detail. As the power source, solar cells with different types of light source were investigated. The solar cell selected to be used as the power supply for energy harvesting devices should harvest sufficient energy to operate robustly when deployed, irrespective of the type of light source providing the illumination. The investigation was therefore based on typical levels of illumination in buildings, and has shown the practical effects of changing the type of illumination sources used on the output power densities of selected types of solar cells. A change in the type of illumination source used causes a change in the radiant spectra of the ambient light. A solar cell can harvest more power when its spectral sensitivity, which is defined by its active materials, fits the radiant spectra of ambient light sources.

The output power densities of four solar cells have been investigated in different sections of the visible light spectrum using a colour-controllable LED. To achieve the same measured lux level, the blue light mode has to emit the most radiant power followed by the red mode and then the green mode. This is because the human eye is not as sensitive to blue wavelengths as it is to red and green. Consequently, all the solar cells tested can harvest more power under blue illumination than for red and green illumination for the same perceived luminous intensity. In an illumination system inside a building, the colour of the light is usually white for general use, and colour changing lamps are mainly used for entertainment. However, from our measurements, green light should be considered as the worst illumination colour condition when designing an energy harvesting device.

The output power densities of four types of solar cells have been investigated under three typical illumination sources encountered in buildings. The detrimental effect of upgrading to higher efficiency illumination sources on the performance of solar energy harvesting devices has been evaluated. In most cases, maximum power is harvested by solar cells under incandescent illumination sources followed by CFL and then LED.

The amorphous-Si solar cells tested (AM-5608 and AM-1815) show a similar power output under all three tested illumination sources encountered in buildings, therefore, for general use from both natural and artificial lighting sources, a solar cell based on amorphous silicon will perform satisfactorily under all lighting sources.

The large difference in output power of the polycrystalline silicon solar cell (MC-SP0.8) between incandescent and CFL/white light LED sources could restrict operation to just incandescent lighting. Indoor energy harvesting devices based on this type of solar cell will perform poorly if the lighting source is upgraded to CFL or white light LED.

All the solar cells examined have a region larger than 20% of their operation current area in which their power density is at least 90% of the output power density of that at their MPP, with the exception of the DSSC flexible solar cell under the LED light source. The DSSC flexible solar cell harvests least solar energy in all situations but is required in any application needing flexibility, such as mounting onto curved-surfaces.

The proportional overlap between the normalised source spectra and solar cell sensitivity spectra was examined for combinations of white-light sources and the cell materials, this can be used to give indicative results however the actual conversion efficiency values for the solar cell materials are needed to give output power comparisons between the different materials.

The investigations of MCU, radio transceiver, and PIR sensors were investigated, then the system design was discussed. System tests in a normal office environment verified the validity of design of both hardware and software. This chapter has investigated the system blocks in a wireless sensor powered by energy harvesting. As an initial stage of the present research, it was proposed that a commercially available harvesting device should be used. This detector includes a flexible solar cell, a custom built power subsystem, an evaluation board consisting of the MCU with transceiver, and an integrated PIR sensor for detecting occupancy, the designed detector functions adequately for continuous operation powered only by ambient light sources. Compared with similar products provided by EnOcean, this designed detector with the flexible solar cell has the advantage on collecting light energy from different angle (>90°) and can survive from longer “dark” time (>16 hours compare with 8 to 10 hours). It shows that, after an investigation on the available ambient energy sources and the energy harvester for such energy, the passive sensor can be designed with the feature of self-powering for applications, which employing a microprocessor, of an AAL system in building environment as demonstrated in the PIR detecting and monitoring in this chapter.

4 Theory of Wireless Power Transfer

4.1 Introduction

The Wireless Power Transfer (WPT) theory model of inductively coupled systems is studied in this chapter, and the key parameters of the two coupled oscillating coils, which are the major elements to design, calculate, fabricate and examine in this thesis, are discussed. Expressions for the key electrical characteristics of a flat spiral air core coil and the coupling coefficient of two coils are obtained from the analysis to guide the design of a coil to achieve the desired result. The relationship between the parameters of the coils and the coupled system is discussed based on the electrical characteristics. An expression for the resonant tank capacitors used to compensate the coils in the circuit is studied, and optimised to give optimal operating conditions for the WPT system.

4.2 Inductively Coupled System for Wireless Power Transfer

4.2.1 Coupled-Mode Theory

The inductively coupled system for WPT is based on the coupled-mode theory that provides an accurate modelling of different resonant objects [147], in this system, the transmitter (TX) and receiver (RX) coils are coupled and transfer the energy wirelessly. For an ideal coupled system, entire power transmitted by the TX coil can be received by the RX coil, relatively, certain part of the power will be leaked between two coils in the practical system. The efficiency of the link between TX and RX coils is the ratio of the power received to the power transmitted. The analysis model of the link between TX and RX coils has the optimum efficiency which is given by [148]:

$$\eta_{link} = \frac{k^2 Q_{TX} Q_{RX}}{(1+\sqrt{1+k^2 Q_{TX} Q_{RX}})^2} \qquad (4.1)$$

Where: k is the coupling factor between the resonant coils. Q_{TX} and Q_{RX} are the unloaded quality factor of the TX and RX coils, respectively, k, Q_{TX} and Q_{RX} are the dimensionless quantities and will be discussed in the following sections in this chapter. The theoretical efficiency of the link between TX and RX coils against the key parameters of $k^2 Q_{TX} Q_{RX}$ is shown in Figure 4-1.

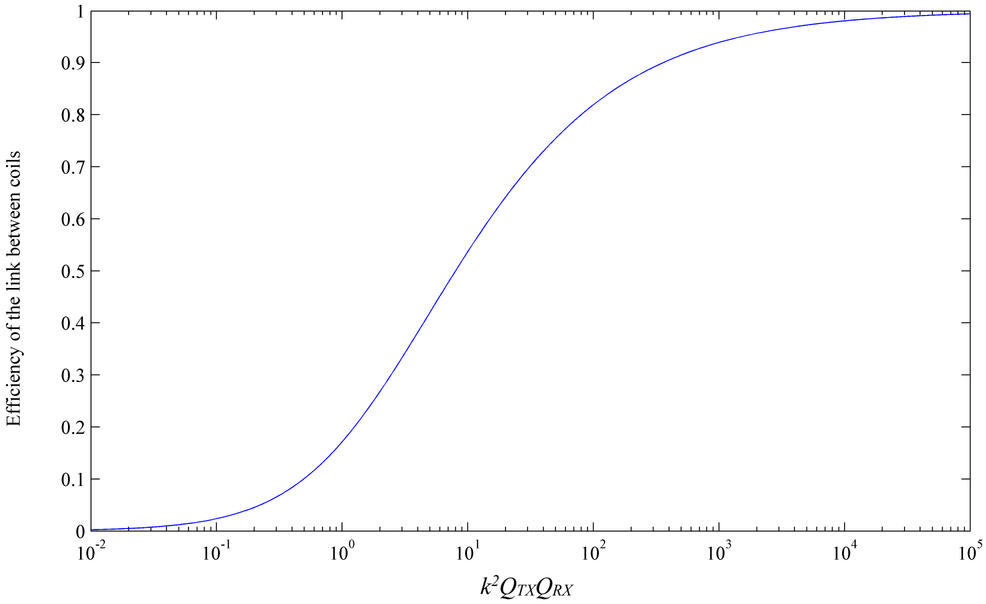

Figure 4-1 Theoretical efficiency between TX and RX coils against $k^2Q_{TX}Q_{RX}$

Large values of k, Q_{TX} and Q_{RX} are desired to gain a high efficiency of the link. In Figure 4-1 the efficiency of the link is less than 10 % when $k^2Q_{TX}Q_{RX}$ is less than 0.5, which means more than 90 % power is leaked in the system that is not acceptable. On the other hand, the efficiency increases tardily when $k^2Q_{TX}Q_{RX}$ is greater than 400. To design a coupled system employing the printed coil, the relationship between physical parameters, electrical characteristics of coils are being discussed in following sections to achieve an efficiency as high as possible.

4.2.2 Transferring Power via Two Coupled Coils

Inductive WPT is based on the theory described by Maxwell's equations. An alternating current through the TX coil conductor produces an oscillating magnetic field, this oscillating magnetic field creates an electric field within the RX coil, and the electric field causes the electrical charges to move, producing a current to load. The TX and RX coils construct a coupling system with an oscillating magnetic field, the coupling factor k is a key parameter to evaluate a WPT system that reflects the quality of the connection and thus the efficiency of the link between TX and RX coils. The coupling factor is related to the positional relationship of the two coils and is proportional to the difference in self-resonant frequency between such two coils. In the case that one coil has been excited by an energy source, and the other coil consumes power, the coils transfer power with a wave that carries negative energy. A fraction of the overall magnetic flux linkage between the coils can be defined to reflect the losses due to leakage and the relative position of coils, this fraction is defined as coupling factor k and therefore given by [149]:

$$k = \frac{M_{TR}}{\sqrt{L_T \times L_R}} \tag{4.2}$$

where M_{TR} is the mutual inductance between the TX and RX coils, and L_T and L_R are the self-inductance of the TX and RX coils, respectively. The mutual inductance that links the TX coil to the RX coil directly correlates to the separate distance between two coils. The electromagnetic field generated by the TX coil is induced into an adjacent receiver coil by mutual induction M, while the two coils are magnetically linked together by a common magnetic flux. Mutual inductance is the basic operating principle of inductively coupled inductive power transfer, and it is defined as the current flowing in one coil that induces a voltage in another, adjacent, coil. In a given wearable application, the size of the coil in the system is limited in a range based on the context, at the same time, the distance between two coils can be varied caused by the movements during the usage. The isolation for the printed coil, which providing the production for both system and user, is necessary and increases the distance between the coils. These limitation reduces the coupling factor k unavoidable, to achieve a desired efficiency between coils, the key parameters for the unloaded quality are mainly discussed in the following sections.

4.3 Mathematical Circuit Modelling for Coil Inductor

In the WPT system, the resonant objects are the transmitter and receiver coils, and they are coupled in an electromagnetic field. The relationship between the physical dimensions of the coils and the parameters of objects in coupled system theory is analysed in this section. The equivalent circuit of a coil with an air core [150] is shown in Figure 4-2. The inductance of the coil is presented as L, the parasitic capacitance of the coil is presented as C, and the resistance of the coil includes the series resistance R_s and the parallel resistance R_p. The series resistance represents energy consumed in the inductor, and the parallel resistance represents that consumed in the parasitic capacitor. The power consumed in the parasitic capacitor in a general coil is a minor fraction of the overall power, so the parallel resistance is in a mega ohm range.

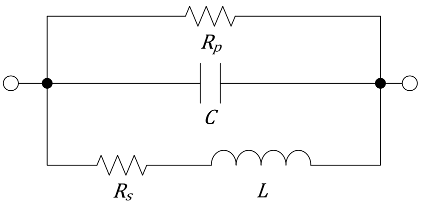

Figure 4-2 Equivalent circuit of coil

Circular spiral designs, as well as polygonal spirals such as hexagonal and octagonal are used widely as planar inductors. Figure 4-3 (a)-(d) shows their layout.

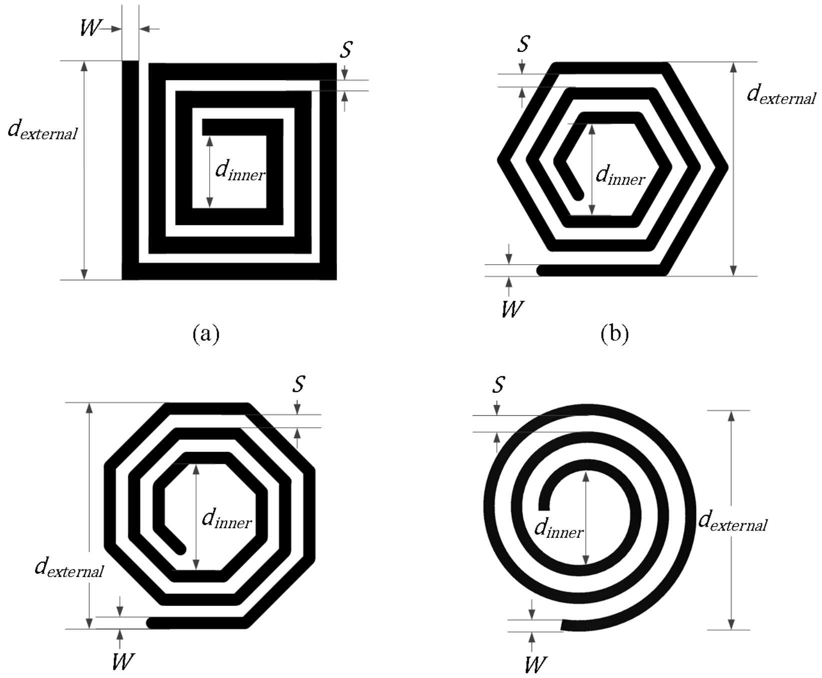

(a) (b) (c) (d)

Figure 4-3 Shape designs of coils

For a given shape of flat coil, the electronic characteristics of a coil are specified by the number of turns N, the track width W, the spacing between two tracks S, the thickness of track t_c and any one of the following: the external diameter $d_{external}$, the inner diameter d_{inner}, the average diameter $d_{avg} = \frac{d_{external}+d_{inner}}{2}$, or the fill ratio, defined as $\Delta = \frac{d_{external}-d_{inner}}{d_{external}+d_{inner}}$, so the length of wire and gap in coils are derived as equations below:

$$l_{wire} = \pi N(d_{external} - NW - (N-1)S) \tag{4.3}$$

$$l_{gap} = \pi N(d_{external} - NS - (N-1)W) \tag{4.4}$$

4.3.1 Self-inductance

The inductance of a coil is affected by its shape, dimension, and the number of turns, for given values of N, d_{inner} , $d_{external}$, W and S, square and circular coils have different inductance. For an engineering calculation of the inductance of a flat spiral coil with an air core, several different approximations exist [119, 151]. The difference in the result that is obtained by applying different formulae does not exceed 10% for any system. Many researchers use the formula given in [152]:

$$L_{sheet} = \frac{\mu_0 N^2 d_{avg} c_1}{2}\left(\ln\left(\frac{c_2}{\Delta}\right) + c_3\Delta + c_4\Delta^2\right) \tag{4.5}$$

where μ_0 , N , d_{avg} and $\Delta = \frac{d_{external} - d_{inner}}{d_{external} + d_{inner}}$ have the same significance as mentioned in previous sections. The four parameters from c_1 to c_4 are used to give the value in the equation 4.5 depend on different shape of coil, which are listed in Table 4-1.

Table 4-1 Parameters for different shapes of coil [152]

Shape	c_1	c_2	c_3	c_4
Square	1.27	2.07	0.18	0.13
Hexagonal	1.09	2.23	0	0.17
Octagonal	1.07	2.29	0	0.2
Circular	1	2.46	0	0.2

For the same N, d_{avg}, and Δ, it can be calculated using equation (4.5) that a square coil has the largest inductance. In an application that has a square enclosure, the square coil design is therefore the best design to get a large inductance. For a coil which is formed as a double flat spiral conductive track structure, the equivalent inductance of the coil L_{double} can be calculated by considering two series inductances L_{top} and L_{bottom} with a coupling coefficient between them. Hence, L_{double} is expressed as [153]:

$$L_{double} = L_{top} + L_{bottom} + \mu_0\mu_r K_N\sqrt{{d_{external}}^2 + {t_{dielectric}}^2} \tag{4.6}$$

where K_N is Nagaoka's coefficient, as the parameters used in this thesis, this coefficient only depends on the space between two layers, and it can be obtained from the table reported in [154]. In another case, the cylindrical wound copper coil with air core and same equivalent diameter of d_{avg} and Δ as the flat coil also has similar inductance with 5% error, and is used to compare the performance of different types of coil with similar inductance in WPT systems.

4.3.2 Resistance

The series resistance of a coil is formed of the DC resistance R_{DC} and AC resistance R_{AC}. The DC resistance is the related resistance of a practical conductor, given by [155]:

$$R_{DC} = \rho\frac{l_{wire}}{A} = \rho\frac{l_{wire}}{W t_{wire}} = R_{sheet}\frac{l_{wire}}{W} \tag{4.7}$$

where ρ is the resistivity of the conductive coil track, l_{wire} is the length of the track, A is the cross section area of the track with the thickness of t_{wire} and the width of W. For a printed conductor, the sheet resistivity R_{sheet} is normally given by the manufacturer as described in Chapter 2. For a single layer coil which has 5 turns and 2 mm space between each turn, the resistance is calculated and shown in Figure 4-4.

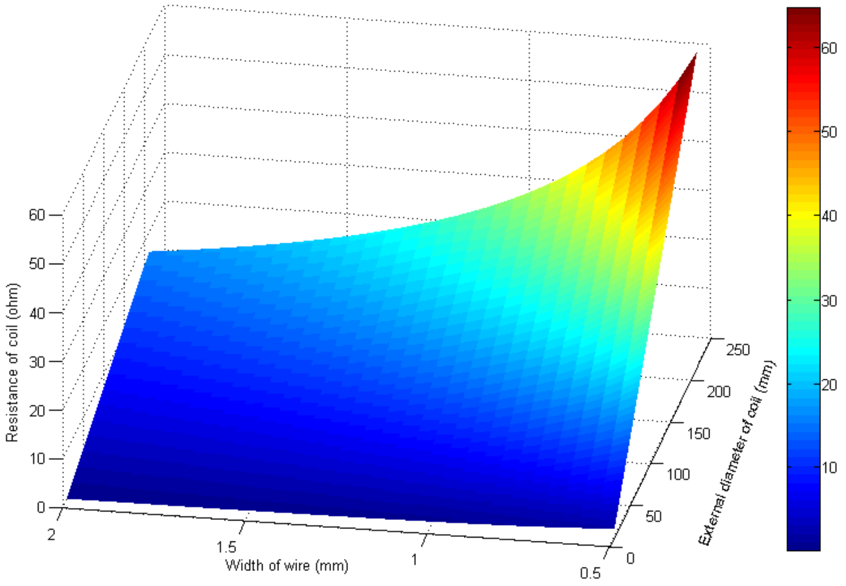

Figure 4-4 Resistance of single layer coil

The figure suggests that the resistance of the printed coils increases dramatically when $\frac{l_{wire}}{W}$ reaches a certain threshold. Setting a larger W yields a lower DC resistance for a coil with the same external diameter.

At the same time, the AC resistance R_{AC} increases the coil resistance considerably at MHz operating frequencies. R_{AC} is composed of the skin effect and the proximity effect. The skin effect is the tendency of an AC to flow mostly near the outer surface of a conductor, and this results in a higher resistance compared with the DC mode [156].

For a current with J as current density flowing through a conductor of rectangular cross-section, the depth below the surface of the conductor at which the current density has fallen to $1/e$ of J_s ($J = J_s e^{-d/\delta}$) is given by the skin depth δ [157]:

$$\delta = \sqrt{\frac{2\rho}{\omega\mu_0\mu_r}} \tag{4.8}$$

where ρ is the resistivity of the conductor, ω is the angular frequency of the current and μ_0 is the absolute magnetic permeability of the conductor. For a conductor which has a rectangular cross-section, R_{skin} is proportional to R_{DC}, as [158]:

$$R_{skin} = R_{DC}\frac{1}{1-\frac{A'}{A}} \tag{4.9}$$

$$A' = W \times t_c - (W - 2\delta)(t_c - 2\delta) \tag{4.10}$$

The AC in one track generates an oscillating magnetic field in space, which then generates eddy current in the other track, so when the coil is carrying AC, the proximity effect occurs because the eddy current increases the resistance of the entire coil. The equivalent resistance of the proximity effect is given by [159]:

$$R_{proximity} = 0.1R_{DC}\left(\frac{\omega}{\omega_{critical}}\right)^2 \tag{4.11}$$

The critical frequency at which AC coil resistance begins to increase significantly is given by [160] :

$$\omega_{critical} = \frac{3.1}{\mu}\frac{(w+s)}{w^2}\frac{\rho}{h} \tag{4.12}$$

where μ is the permeability of the conductor material. This explains why a smaller width of wire to width of space ratio can be used to decrease resistance. The operating frequency is set below the critical frequency to avoid the increase of resistance due to the skin effect and the proximity effect. As the result, the approximated series resistance of coil is [159]:

$$R_s = R_{DC}\frac{t_c}{\delta\left(1-e^{-t_c/\delta}\right)} \tag{4.13}$$

The parallel resistance of the coil results mainly from the dielectric loss [161]. The dielectric materials used in the substrate and coating, as well as the surrounding air, have low dielectric loss. By comparison, when the coils are put on clothes, the tracks are surrounded by the human body, that the distance between the tracks and the human body is in the range from few to decades millimetre. The human body has high permittivity and significantly increases the dielectric loss of the coils. The total R_p is given by [162]:

$$\frac{1}{R_p} = \frac{\omega\varepsilon_0\varepsilon_r \tan\delta}{2\pi} \ln\left(\frac{4(\sqrt{2}+1)}{\sqrt{2}-1}\right) \tag{4.14}$$

where ε_r is the relative permittivity of the material around coil tracks. A larger coil resistance consumes more energy, which is supposed to be delivered to the application, and it also reduces the unloaded quality factor of the coil. Therefore the coil is designed so as to minimise it as described in Chapter 5. The resistance as well as the flexibility of the printed conductor in this work are discussed as properties of fabricated samples in Chapter 6.

4.3.3 Parasitic Capacitance

The parasitic capacitance of the coil is mainly determined by the spacing between planar conductive tracks and their surrounding materials. When the coils are worn next to the body, the parasitic capacitance is significantly increased. Modelling the capacitances in a system in different surroundings and with different coupled statuses gives a range of capacitance for a given system.

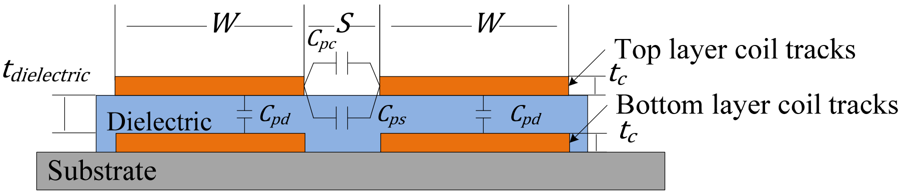

Figure 4-5 Parasitic capacitance in double conductive layer structure flat coils

There are two types of insulating materials affecting the capacitance of each layer as shown in Figure 4-5. One is air or the coating insulator that fills the gap between adjacent tracks. The other is the substrate. Therefore, the capacitance of a single layer coil, either top layer coil track or bottom layer coil track, can be approximated as [161]:

$$C_{Single} = C_{pc} + C_{ps} \approx (\alpha\varepsilon_{rc} + \beta\varepsilon_{rs})\varepsilon_0 \frac{t_c}{s} l_{gap} \tag{4.15}$$

where ε_{rc} and ε_{rs} are the relative permittivity of the coating and substrate materials respectively, and α and β are measured by the method given by Ashoori, *et al.* in [159]. For the bottom coil layer, both the coating and substrate materials are the interface material described in

Chapter 5. For the top coil layer, the coating material is air or the human body and the substrate is interface material. For air $\varepsilon_{rc} = 1$, and for the human body $\varepsilon_{rc} = 70$ [163], for any other material without a known permittivity, a simple measurement of the capacitance C and thickness d on the samples can deduce the relative permittivity, with a given limited area of overlap of the two plates that clamp such samples as:

$$C = \varepsilon_r \varepsilon_0 A/d \tag{4.16}$$

The parasitic capacitance between two layers is formed between top and bottom coil tracks and is dependent on the thickness of the dielectric layer. This capacitance is expressed as [164]:

$$C_{pd} \approx \frac{\varepsilon_{rs}\varepsilon_0 l_{wire} W}{t_{dielectric}} \tag{4.17}$$

For a coil with double flat spiral conductive track structures, the overall parasitical capacitance is:

$$C_{overall} \approx \frac{C_{Single}}{2} + C_{pd} \tag{4.18}$$

This indicates that using double layer coils results in larger parasitic capacitances and reduces the self-resonant frequency of the coils.

4.3.4 Self-Resonant Frequency

The Self-Resonant Frequency (SRF) of a coil is caused by the parasitic capacitance resonating with the inductance, so that the inductor becomes a parallel resonant tuned circuit. Since early in the last century, engineers have recognised the effect of distributed capacitance within an inductor and the resulting SRF as follows [165]:

$$f_r \cong \frac{1}{2\pi\sqrt{LC}} \tag{4.19}$$

When the coils operate at resonant frequency, the two current and charge density profiles that form as $\lambda_0 \sin(\frac{\pi s}{l})\, e^{-i\omega_0 t}$ are $\pi/2$ out of phase from each other, so that the real part of one is maximum when the other one is zero. Equivalently, the energy contained in the coils at certain time points is completely due to the current, and at other certain points, completely due to the voltage. As defined in electromagnetic theory, L and C have the property that the energy U contained in the coil is given by [166]:

$$U = \frac{1}{2} L |I_0|^2 = \frac{1}{2C} |q_0|^2 \tag{4.20}$$

In the coupled-mode model, given in equation 4.1, the decay constant at the resonant frequency is given by $\Gamma_{coil} = (R_s + R_p)/2L$.

4.3.5 Unloaded Quality Factor

The dimensionless unloaded Q factor characterises the bandwidth $\Delta\omega$ of a resonator relative to its centre frequency, and in coupled model theory, a resonant coil loses $1/Q$ of its energy in one period away from the centre of oscillation. The unloaded quality factor (Q) of a coil can be obtained as the ratio of stored against lost energy. It describes how under-damped the coils are, and is used to evaluate the quality of coils, whereby a high unloaded Q factor indicates a lower rate of energy loss relative to the stored energy of the induction coil [41]. Taking the electrical characteristics of the coil mentioned sections in 4.3.1 – 4.3.3 into account, the unloaded Q factor is given as [160]:

$$Q_{unload} = \frac{\omega L - \omega\left({R_s}^2 + \omega^2 L^2\right) C_p}{R_s} \tag{4.21}$$

In the relative researches, the equivalent parallel resistor is in a range of mega ohm, consequently, the effect of it on the unloaded Q is negligible. The unloaded Q is calculated with a given inductance and resistance of the coil, with varying operating frequency and parasitic capacitance, shown in Figure 4-6 to demonstrate the effect. The highest frequency of the varying range of operating frequencies of the coil is set below the self-resonant frequency of such coil since that the coil shows capacitive nature when it operated at the frequency above the self-resonant frequency, which in that frequency, the inductively coupling cannot be built and no energy can be transferred.

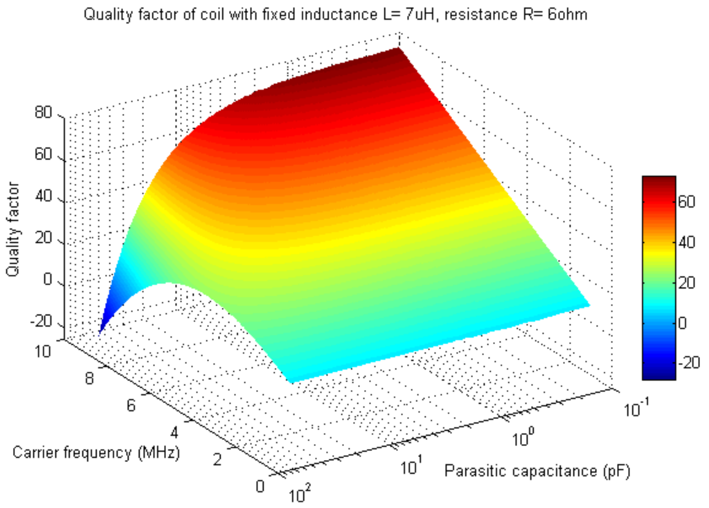

Figure 4-6 Quality factor with variable capacitance and carrier frequency

Many researchers assume that the C_p is negligible or the frequencies are low, and therefore take an unloaded Q as approximately $\frac{\omega L}{R_S}$ [159, 161, 167]. Figure 4-6 suggests that the capacitance of a given coil has a limited effect only when it is smaller than a critical value, which is 10 pF in the given configuration of other parameters in this simulation of the application, and at the same time, the coil is required to operate under a certain frequency, which is under 5 MHz. The upper limit of the frequency is much lower than the reviewed research because the parasitic capacitance is increased dramatically when the coils are printed on a flexible substrate or coated by a thin flexible dielectric layer.

The effect of inductance and operating frequency on unloaded Q is shown in Figure 4-7, calculated with a given parasitic capacitance and resistance. The highest frequency of the varying range of operating frequencies of such coil is below the self-resonant frequency as mentioned.

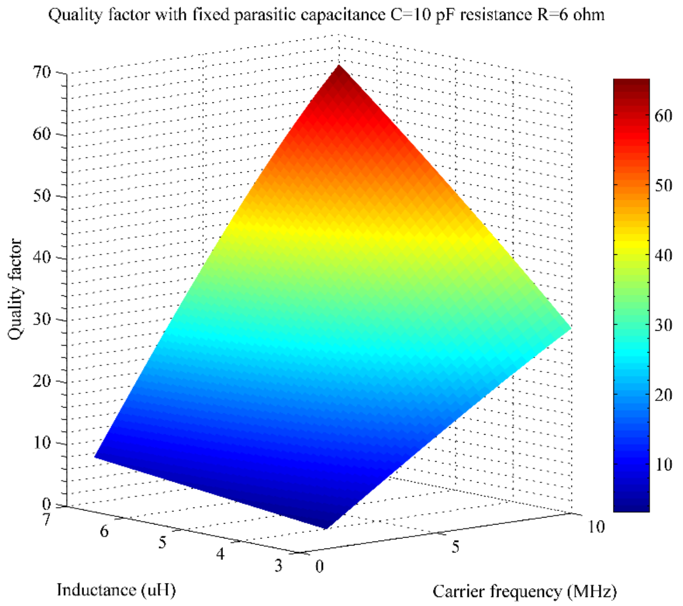

Figure 4-7 Quality factor with variable inductance and carrier frequency

Figure 4-7 suggests that, by increasing inductance, the unloaded Q factor is improved. The effect of inductance on the unloaded Q factor is greater at higher frequencies: 0.5 μH^{-1} at 1 MHz compared with 10 μH^{-1} at 10 MHz. An optimal unloaded Q factor of coil is a high priority in the coil design, so that the efficiency of WPT can be maximised [148]. In a comparison between the unloaded Q factor of printed coils with different shapes of square or circle with the same N, W, S, t_c, $d_{external}$ and d_{inner}, it was found that the circular coils have the highest unloaded Q factor of the coils with different shapes, because a shorter length of track and lower resistance are critical due to the limitation on the conductivity of printable paste. The square coils have the largest inductance of different shapes, but the circular coils have the highest unloaded Q factor, and consequently a coil with a higher unloaded Q factor is more efficient in a coupled system.

4.3.6 Mutual Inductance of Two Coils

The power is transferred via the magnetic field, with the magnetic flux produced by either inductor being coupled to the other. In an ideal coupled model comprising two coils on an infinitely permeable magnetic core, driving the TX side produces an oscillating magnetic flux, which is fully coupled to the RX coil with no flux leakage. In the case of flux leakage occurring, the influence of the transmitter and receiver coils on each other is introduced by the mutual inductance M_{TR}. The mutual inductance is determined by the position and separation distance between two coils as shown in Figure 4-8.

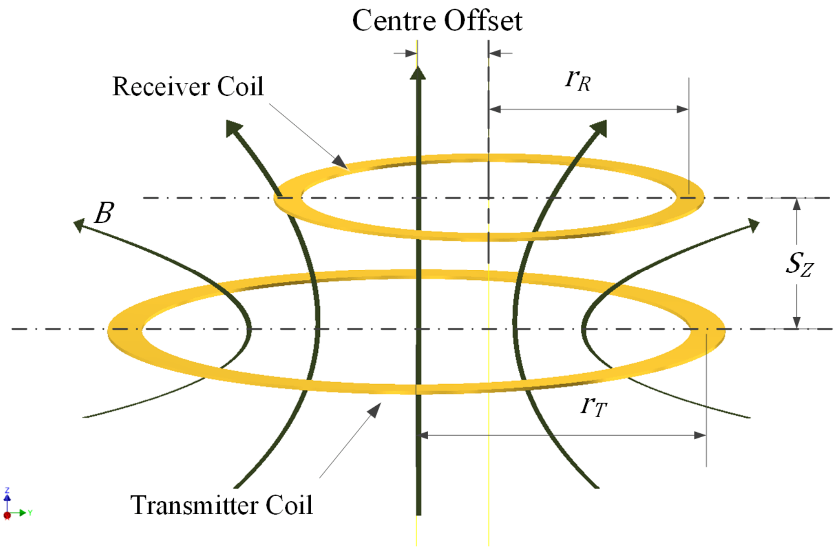

Figure 4-8 Position and separation distance between transmitter and receiver coils

The TX and RX coils have radii of r_T and r_R, respectively. The central spacing between these coils is S_Z, and the lateral misalignment is α. The mutual inductance of two coils is calculated as [168]:

$$M_{TR} = \mu_0 \pi \sqrt{r_T r_R} \int_0^\infty \left(J_1\left(x\sqrt{\frac{r_T}{r_R}} \right) J_1\left(x\sqrt{\frac{r_R}{r_T}} \right) J_0\left(x\frac{\alpha}{\sqrt{r_T r_R}} \right) e^{-x\frac{S_Z}{\sqrt{r_T r_R}}} \right) dx \qquad (4.22)$$

where J_0 and J_1 are the Bessel functions of the zeros and first order, respectively. M_{TR} will increase when the radii increase, one design rule is therefore to set the r_T and r_R as large as the application size allows [169]. To simplify the integration in the expression, a coupling factor between two coils is introduced to reflect the leakage part of the overall magnetic flux linkage between the coils.

4.3.7 Coupling Factor between Two Coils

The coupling factor k is a measure of the relationship between the RX and TX coils, it measures how efficiently the RX coil receives the magnetic flux from TX coil. A factor of one corresponds to the ideal model where there is zero flux leakage, and zero means no coupling at all. For practical system, the coupling factor is between zero and one. In a WPT system, the coupling factor is expected to be as high as possible to optimise the transfer efficiency between TX and RX coils. The exact value of coupling factor k is demanding to calculate, and at the same time, it will vary during experiments. An approximate formula is given in [170] for flat spiral coils:

$$k \approx \frac{{d_{external\_t}}^2 {d_{external\_r}}^2}{\sqrt{d_{external\_t} d_{external\_r}} \left({S_Z}^2 + \max(d_{external_t}, d_{external\_r})^2 \right)^{\frac{3}{2}}} \tag{4.23}$$

For coils with a known size, the coupling factor k is affected by the distance between two coils, S_Z. In this thesis the coupling factor is also measured for each pair of printed coils to determine the resonant tank capacitor required for each individual coil at the desired operating frequency, an optimal resonant coupling is studied in [167] and discussed in Section 4.4 and Chapter 5 to calculate the resonant tank capacitors, and an expected coupling factor will be estimated in Chapter 5 based on the coil design and the separated distance between TX and RX coils in the application scenario. In the experiment, the coupling factor can be calculated based on a given driving oscillating voltage V_T across the TX coil and measuring the receiving oscillating voltage V_R across the RX coil with an infinite impedance as [96]:

$$k = \sqrt{\frac{V_{TA} V_{RB}}{V_{RA} V_{TB}}} \tag{4.24}$$

Where the voltage values with subscript A are measured when driving to the coil A and receiving from the coil B, the voltage values with subscript B are measured when driving to the coil B and receiving from the coil A.

4.4 Compensation Circuitry

Compensation capacitors are required for both TX and RX coils to optimise the driver and receiver circuits, and to resonate the system to preserve the energy from flux leakage, and they are therefore termed resonant tank capacitors in a WPT system. The magnetic coupling is therefore maintained, and the energy entered into the system can be delivered to the load.

Assuming the system has a series compensation secondary and a resistive load, the circuit can be analysed, beginning with the load, then the RX coil, and ending with the TX coil for simplification. The RX coil impedance Z_{L_R}, the impedance of RX resonate tank capacitors Z_{C_R}, and the load resistance R_{Load} comprise the overall receiver side impedance as:

$$Z_{RX} = Z_{L\_R} + Z_{C\_R} + R_{Load} \tag{4.25}$$

The effect of varying the impedance of resonant tank capacitance on the voltage across the given load resistance is shown in Figure 4-9 with a given 25 V peak-to-peak voltage received by the RX coil, 7 µH RX coil inductance, 6 Ω RX coil resistance, and operating at 200 kHz.

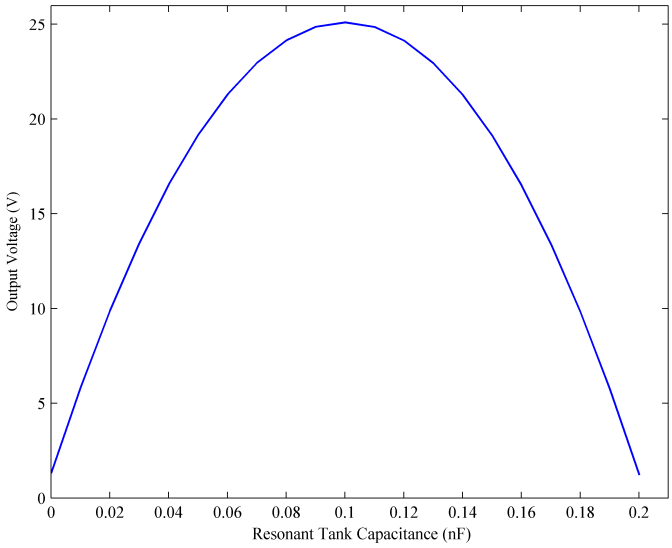

Figure 4-9 Effect of resonant tank capacitance on the voltage crossing the given load resistance

It can be seen that the peak output voltage on the load is occurred when the capacitance of the resonant tank capacitor reaching a certain point, where the capacitive reactance of resonate tack capacitor cancel the inductive reactance of RX coil at the given operation frequency, and in this case, the load gains highest energy from RX coil that achieving the maximum efficiency in such configuration. Consequently, an optimal RX resonant tank capacitance C_R occurs when the L-C circuit is tuned at the operating frequency as:

$$C_R = \frac{1}{{\omega_o}^2 L_r} \tag{4.26}$$

From the point of view of the TX coil, the RX coil is seen as a transformed impedance Z_s from the receiver side as [171]:

$$Z_s = \frac{{\omega_o}^2 {M_{TR}}^2}{{Z_r}^2} \tag{4.27}$$

On the transmitter side, the total impedance Z_{TX} is driven by the AC voltage source, and it is composited by the impedance of the TX resonant tank capacitor Z_{C_t} in series with the TX coil impedance Z_{L_t} and the transformed RX side impedance Z_s as:

$$Z_{TX} = Z_{C\_t} + Z_{L\_t} + Z_s \tag{4.28}$$

The optimal TX resonant tank capacitance is affected by both TX and RX coil and can be obtained when it is tuned at the frequency that the secondary is resonated, which is set as the operating frequency as [104]:

$$C_T = \frac{1}{\omega_o{}^2\left(L_t - \frac{M_{TR}{}^2}{L_r}\right)} \tag{4.29}$$

The practical selection of resonant tank capacitors follows this overall capacitance principle and is discussed in Chapter 5.

4.5 Summary

In summary, this chapter has analytically discussed the theory model related to inductively coupled systems. The key parameters of a WPT system with two coupled coils have been discussed and expressions for the coupling factor have been obtained. These key parameters are listed as follow:

- DC resistance,
- AC resistance,
- Inductance,
- Self-resonant frequency (SRF),
- Parasitic capacitance, and
- Unloaded Q factor.

The relationship between the physical dimensions of the coils and the parameters of objects in coupled systems theory has been discussed. The electrical characteristics such as resistance, capacitance and inductance of the coil were discussed based on established engineering formulae, and these can give a guideline for the design of the coil. The unloaded Quality factor of the coil based on the electrical parameters was discussed, and it is the key parameter to evaluate a coil for use in a WPT system. After the coil has been designed and fabricated, the error should be within 10% between the theoretical calculations applied to the design and the measured values of these characteristics. It is critical that the fabrication result is as expected in theory to ensure the functionality and reliability of the WPT system. The selection of the resonant tank capacitors has been discussed and expressions for a general values have been obtained, the detail design will be discussed in Chapter 5.

5 Design of Printed Coils for Wireless Power Transfer

5.1 Introduction

In this chapter, the materials and designs for screen printed wireless power transfer are finalised. Firstly, substrates for screen printing are described in detail. The pastes for each layer are then selected based on their properties. The coil layout is defined based on the literature review and the theoretical calculation of the coil's inductive properties. Five properties of the coil are defined for practical prototype and experiment, which are the coil shape, size, constant versus variable track width, and single versus double conductive layer structures. Circuitry is designed to make the flexible coil compatible with a WPT system, and the structure and parameters of resonant tank capacitors are discussed.

5.2 Substrate Selection

Commercial screen printing pastes are available with a diverse range of properties and have been successfully tested on rigid and flexible substrate materials. The substrate provides mechanical support to printed structures. For textile substrates, low temperature (less than 130 °C) curing pastes are required to avoid damaging the substrate. The general rule adopted in this work is to cure the paste at the highest temperature that the substrate will handle without degradation or unacceptable dimensional change. The requirements of substrates for the screen printed coil are listed here [125, 172]:

1. Electrical insulation properties.
2. To provide a strong, stable support surface that has a low and consistent surface roughness.
3. To maintain dimensional stability up to the curing temperature of the paste.
4. To comply with dimensional tolerances required for consistently accurate screen printing that ensure the printing process is repeatable.
5. To be capable of having holes fabricated for mounting pins and connectors.
6. To provide a strong bond between the screen-printed layer and the substrate is formed.
7. To be deformed and remain the support for a flexible device.
8. To provide a breathable surface for a wearable device.

An alumina, a polyimide film (Kapton) and a textile are used as substrates in this work. These three materials have different levels of flexibility and compatibility with screen printed electronics.

The alumina substrate has a rigid, dustless, and smooth surface that is used as a substrate for the initial evaluation stage. Aluminium oxide tiles (150 mm × 150 mm × 0.635 mm) from Hybrid Laser Tech Company have been used in this work. The alumina can take temperatures in excess 1000 °C meaning a large range of pastes are compatible. It is easy to print pastes on these alumina tiles, so this is used to test the profile, validate the paste printing process described in Section 2.5, test the curing process, and analyse the electric characteristics of flat coils. Based on previous research [173, 174], the alumina substrate is placed into an ultrasonic bath for 15 minutes using acetone, ethanol and deionised water in that order to clean the surface, after which most of the possible surface contaminants are removed, a clear surface can prevent the contaminants from mixing into the printed paste, and consequently, the clear printed paste could have a more predictable results in the printed layer than the printed paste with contaminants.

The Polyimide film, known as Kapton, was developed by DuPont and has been the industry standard substrate for flexible screen printed electronics for over 45 years [175]. A Kapton substrate has a dustless and smooth surface, it is flexible and can be subjected to up to 400 °C while retaining stability and flexibility. Therefore, Kapton is selected as the substrate to assess the flexibility of coils. Before printing, the Kapton is placed into an ultrasonic bath for 15 minutes, and then glued on to an alumina tile to keep the surface flat. The coil is then printed on Kapton to measure the layer thickness and profile of the coil, validate the paste printing and curing processes on a flexible smooth substrate, and analyse the electric characteristics of the resulting flexible coils.

The textile 65/35 polyester/cotton has widespread use as a material for clothing. For the wireless power transfer system to be wearable, the coils must eventually be printed on textiles like textile 65/35 polyester/cotton. The textile used in this thesis, such as used to fabricate the clothes, have a rough surface, the textile used here has an arithmetic mean surface deviation of 140 µm [176]. Therefore, a smooth interface layer is required between the textile and the printed device layer to ease printing, this will be discussed in Section 5.3.1. The textile is very flexible, has a rough surface with gaps between the textile fibres, low endured temperature, and low surface energy, which exclude most of the potential pastes from consideration. The textile 65/35 polyester/cotton can endure a 130°C curing temperature for 60 minutes without significant damage or degradation. The textile is ironed and shaved to improve the printability of the surface, and then glued on an alumina tile during the printing and curing process to keep the surface flat. The coil is printed on interface-coated textile to validate the paste printing and curing processes on the textile substrate, and analyse the electrical characteristics of flexible coils. These textile printed coils are deployed in a WPT system to examine their functionality in Chapter 6.

5.3 Materials for Screen Printed Coils

5.3.1 Interface and Dielectric Material

Printing the conductive paste directly on the textile causes several issues in manufacture and application. Firstly, a rough or porous substrate causes a higher effective resistance as conductive paste sinks into gaps between the textile fibres [177]. Secondly, the conductive paste printed directly on textile without a supporting structural material is brittle and when the textile is deformed the conductor can be fractured in varying degrees, increasing the resistance of conductive tracks, or even leaving an open circuit [176]. Finally, the resulting profile of a printed conductor is less consistent on a rough substrate. These factors lead to unpredictable inductive properties which can cause the printed coil to lose its functionality, be out of tune in WPT system, or may even overload the driver circuit. An interface layer is therefore required on the textile to create a smooth surface for the printing of subsequent conductive layers with uniform thickness.

Fabink-UV-IF1 from Smart Fabric Inks Ltd has been studied and compared with other products by Paul*, et al.*[172], it is an available flexible interface material for screen printing on textile with high surface energy on its cured surface which is suitable for widely screen printable functional pastes. It is selected as an interface material in this thesis because it has effectively reduced the roughness of a textile for screen printing in previous research [178, 179]. The interface layer provides a smooth surface that provides advantages such as:

- It keeps the thickness of the conductive layer under control.
- It fills the gaps between the fibres and uses less conductive material.
- It gives a good balance of flexibility between the requirements of fabric and conductive layer, providing support to the conductive layer while giving some flexibility for wearer comfort.
- The smooth surface of interface makes it possible to print a profile of the conductor layer with high definition.

The interface layer is printed on the textile to provide the support for the first conductive layer, and also in the crossover layer that insulates one conductive layer from the next. This minimises the capacitive coupling between the conductive layers as well as supporting the top conductors and protecting the entire coil. To obtain a suitable surface energy for the cured crossover dielectric layer and interface layer, the material for both will be Fabink-UV-IF1 [180].

5.3.2 Conductive Material

Fabink-TC-AG4002 silver paste from Smart Fabric Inks Ltd [129] is selected as the conductive paste to print the track to form the coil, which has low sheet resistance (24-27 mΩ/□) and high flexibility, it is composed primarily of silver particles and the conductive polymer binder which provided by the manufacturer. The sheet resistance of printable conductive paste is higher than the pure silver, this is caused by the polymer binder and the gaps between the metal particles. The curing temperature of Fabink-TC-AG4002 is 110-130°C, and the curing time is 2 to 10 minutes for each layer depending on the printed size with the recommended wet deposit thickness of 25 μm. In the uncured liquid state, this conductive paste contains a solvent to maintain the viscosity to make it screen printable, this solvent has higher resistivity than the conductive silver particles and polymer binder in Fabink-TC-AG4002, and will be evaporated during the curing process. After fully curing, the thickness of a silver layer is reduced to 16-18 μm since the solvent has been evaporated. The recommended curing time from the manufacturer is 10 minutes for screen printing small area (less than 5 mm^2), for applications like printed resistors. An area larger than 100 cm^2 is required for flat flexible coils and consequently this requires a longer curing time, which will be measured in Chapter 6.

5.4 Coils Design

5.4.1 Shape

According to the discussion in Chapter 4, the coil can be square, hexagonal, octagonal or circular, for a given diameter, a square coil has the highest inductance, while a circular coil has the highest unloaded Q factor. The resistivity of printed conductor is considerably higher than the copper used in wired coils because of the limitations of the conductive paste for the screen printing, the conductive polymer binder has higher resistivity than silver particles. The printed coil has larger parasitic capacitance because of the thinner isolation than wound copper wire. The circular coil has the lowest resistance and capacitance of all the shape of coils, that essential obtain a high unloaded Q factor.

The square and circular coil shapes are selected for further design and testing in this thesis. Other details of the design are discussed in the following sections, the top-down views of the conductive layer of these spiral coils are shown in Figure 5-1 and Figure 5-2 for square and circular coils, respectively.

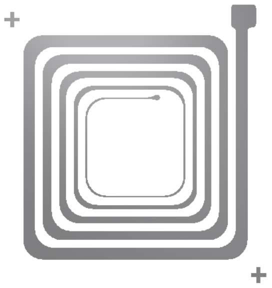

Figure 5-1 The square coil with variable track width.

Figure 5-2 The circular coil with constant track width.

Figure 5-1 shows the shapes of square coil with variable width of track, Figure 5-2 shows the shape of circular coil with constant width of track, the advantage and disadvantage of the track with variable versus constant width is discussed in Section 5.4.3. For a flat single conductive layer structured spiral coil, the conductive layer constructs the coil track. An isolated conductive track, which runs over the spiral coil, connects the coil track from its inner end to an external pad, and then two pads connect inner and outer ends of coils to the driver or receiver circuit.

5.4.2 Diameter

The printed layer structures increase the thickness of the wearable system and reduce textile's flexibility and air permeability, as the compensation, the external diameter of the coils is minimised based on ensuring that the power supply system is as comfortable as possible. An area less than 140 mm × 140 mm of printed coil is smaller than the approximately flat area on the back of 90% human in UK [181], which also fits the printable area (150 mm × 150 mm) of the semi-automatic screen printer used in this work. The paired coils with the size approximately 140 mm × 140 mm diameter have the desired mutual inductance according to the estimation by equation 4.5. The external dimensions $d_{external}$ of coils, including the connection pad, the screen printing alignment aids, and the space between the patterns and the edge of the substrate, are 116 mm × 117.81 mm for the square coil and Ø138 mm for the circular coil in the designs. The external diameter of the TX and RX coils with respect to their spacing and lateral misalignment has a direct positive correlation with the coupling factor when the unloaded Q factor of two coils is fixed [153]. The optimum coupling coefficient is obtained when $d_{inner} \cong 0.4 \times d_{external}$. The inner diameter d_{inner} of the coils in this thesis is 47 mm for square coils and 48 mm for circular coils.

5.4.3 Tracks

The AC and DC resistance of the TX and RX coils consume power and diminish the efficiency of the WPT. The aim of the design on the tracks is to limit the AC and DC resistance as much as possible, hence to maximise unloaded Q factor with same coil inductance and operation frequency. A thicker track has lower DC resistance. However, the thickness is limited by screen printing to less than 250 µm, a thicker layer is time consuming and problematic to build. A thicker track will have greater extension at the extremes compared with the thinner track with same deformation curvature, printed structure and material [182], and will also be more likely to break. A potential solution is an insulation layer over the conductive layer, but this will further reduce the flexibility of the printed coil.

The closer to the centre of a coil, the greater the magnetic field density. The oscillating magnetic field generates eddy currents that causes the proximity effect as mentioned in Chapter 4, resulting in increased AC resistance. By reducing the width of the track, the losses from the proximity effect can be minimised, however, a wider track minimises DC resistance [41]. A design of changings the width of tracks from the centre of a coil to the periphery, a relative narrow track width is designed in the centre of the coil where has relatively high magnetic field to reduce the proximity effect, hence to reduce the AC resistance, and a wider track is deployed in the periphery where has relatively low magnetic field density to minimise DC resistance. The design with the variable width tracks gives consideration to the different relative magnitudes of AC and DC resistance at varying distances from the centre of the coil. Ng*, et al.* [41] have compared the results of the improvement on the coil with this design and another design which the coil has a variable width of the space between the coil tracks with constant width, and the results show the advantages on the design of the coil with variable-width tracks. This design improves unloaded Q factor by increasing track width as it spirals outwards that as shown in Figure 5-3.

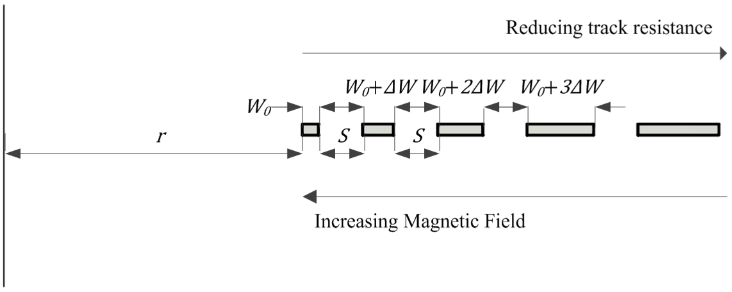

Figure 5-3 The cross section of the tracks of coil with variable width

The radius for the start of each turn of the coil, is given in equation 5.1 below:

$$r_N = r + N(w_0 + s_0) + \frac{N(N-1)}{2}(\Delta w + \Delta s) \quad (5.1)$$

where N is an integer number of turns of coil. The width of space between tracks S should be equal or greater than 2 mm to minimize parasitic capacitance, as discussed in Section 4.3. A larger track spacing gives a slightly lower parasitic capacitance but decreases the width of tracks in the same room for the same number of turns, which introduces extra DC resistance. The track spacing S is therefore fixed at 2 mm. For instance, the calculation result of a coil which has 5 turns in a 120 mm external diameter with 4 mm track spacing is that the coil track has the initial inner minimum track width $W_0 = 2$ mm and per-turn increase in track width $\Delta W = 1$ mm, but with 2 mm track spacing, the coil track has the initial inner minimum track width $W_0 = 3.6$ mm and per-turn increase in track width $\Delta W = 1$ mm. This 1.6 mm difference between the initial inner minimum track widths leads to 13% reduction of DC resistance from the track with 4 mm spacing to the one with 2 mm spacing.

5.4.4 Number of Turns

The following analysis identifies the optimum number of turns for square or circular coil with either constant or variable width. When increasing the number of turns N of a coil, both the numerator and denominator of its unloaded Q factor are increased as described in equation 4.21. The relationship between N and Q factor was calculated in MATLAB by using the equations 4.5, 4.7, 4.9, 4.11, 4.13 and 4.14, and is illustrated in Figure 5-4. This calculation uses the following parameters, 200 kHz operation frequency, 138 mm external diameter, 53 mm inner diameter, 2 mm spacing between tracks, and a constant track width which calculated for each coil with different number of turns to fit a given number of turns in limited printed area. The coil with variable width of track and a double conductive layer structure will be discussed later.

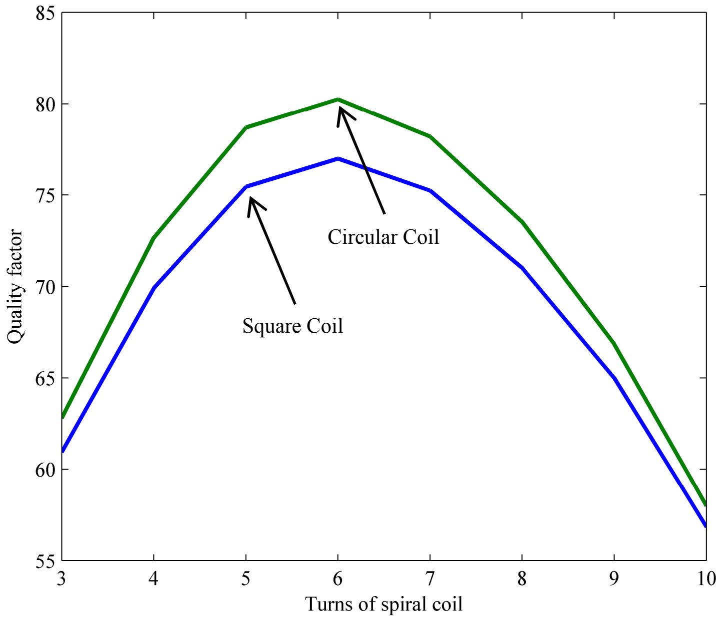

Figure 5-4 Unloaded Q factor versus the turns of spiral coil with 138 mm external diameter

The unloaded Q factors are calculated for the coils with both circular and square shapes with a 24 mΩ/□ sheet resistance. With an external diameter of 138 mm and inner diameter of 48 mm, the 6-turn coil has the highest unloaded Q factor for both shapes of coils. The circular coil has a higher unloaded Q factor than the square coil for all numbers of turns. The width of each turn of the track can be calculated based on the number of turns in the given space between the external and inner margin, for instance, the 6 turns coil has 4.5 mm wide conductive tracks.

When the external diameter is increased and all other coil and operation parameters remain the same, the optimal number of turns is greater and a higher unloaded Q factor is obtained as shown in Figure 5-5. This confirms that by increasing the size of the coil, the unloaded Q factor can be increased as discussed in Chapter 2.

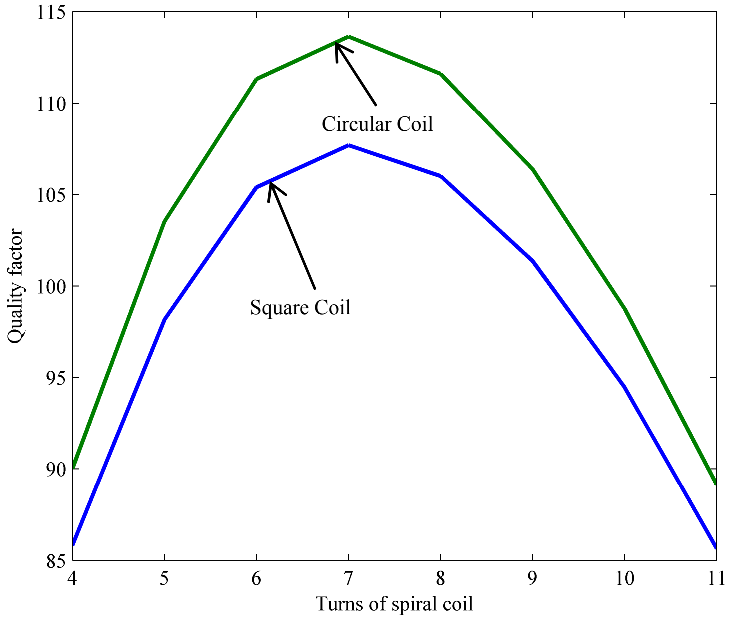

Figure 5-5 Unloaded Q factor versus the turns of spiral coil with 200 mm external diameter

The figures of the calculation of unloaded Q factor for coils with different external diameters show that for any number of turns, N, the circular coils have a higher unloaded Q factor than square coils, this appears to be true irrespective of the external diameter. This effect is caused by the shorter track length the circular coil has than the square one, furthermore, the relatively high resistance of the printed coil, which due to the relatively high sheet resistance of screen printed conductive pastes, increases these differences between circular and square coils.

To connect the inner end of the coil at the centre to the connection pad at the periphery, another conductive layer is required. This could be achieved using a second spiral coil layer design or a simple straight line. The major advantage of a coil with two spiral conductive layer structures is the doubling of the number of turns of the coil within the same printed area. However, there are also disadvantages like higher resistance and a large overlap area that leads to relatively high parasitic capacitance. The optimal design of parasitic capacitance will be discussed in Section 5.4.5, as the square and circular coils with constant width of tracks is very limited on the improvement, consequently, these designs will not be considered for a double conductive layer structure. A simulation on unloaded Q factor has been taken for the square and circular coils with same parameters of the external and inner dimension, the configuration of variation on the width of track, and the spacing between tracks. This simulation shows a comparison between coils with a single conductive layer structure and coils with a double conductive layer structure. The unloaded Q factors at 200 kHz are shown in Figure 5-6.

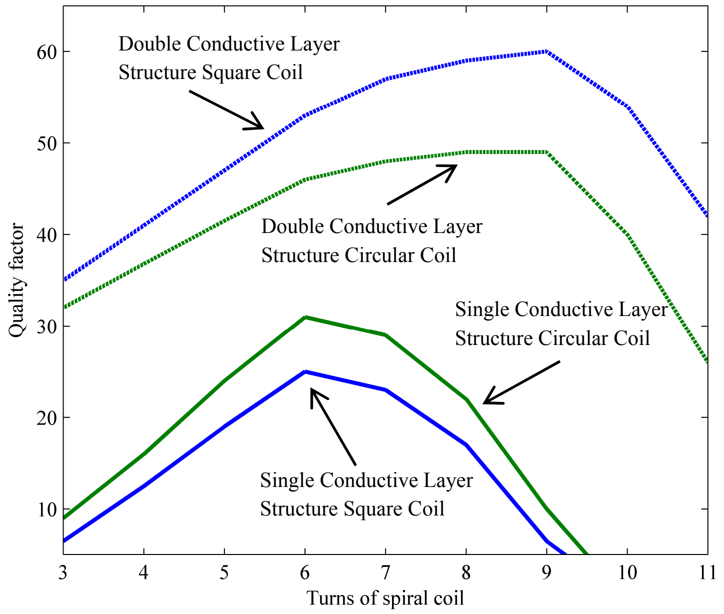

Figure 5-6 Unloaded Q factors comparison between the printed coils with single and double conductive layer structure

After comparing coils with different shapes, it was found that the circular coils have a larger unloaded Q factor, a shorter track length and a lower resistance than the square coil. The resistance is considerably higher than a wound copper coil (typical 100 Q factor) because of the higher resistance of the conductive paste used in the screen printing. This limitation on the conductivity of printable paste makes the resistance the key limiting factor of the unloaded Q factor of the printed coil with this design for the applications investigated in this thesis. For the circular coil, a single conductive layer structure coil with 6 turns has the highest unloaded Q factor, and the width of the track is 4.5 mm with a track pitch of 6.5 mm. For the square coil, a double conductive layer structure coil with 9 turns (4 turns and 5 turns for two layers) has the highest unloaded Q factor, the width of track is configured as the initial inner minimum track width, W_0, is 3.6 mm and per-turn increase in track width, ΔW, is 1 mm.

5.4.5 Minimising Parasitic Capacitance

At the corner of the square coil, the 90° turn introduces undesirable parasitic capacitance and increases noise in EMF for high frequency applications [183]. All the corners of the square coil are filleted with same radius to minimise the parasitic capacitance on turns as shown in Figure 5-7.

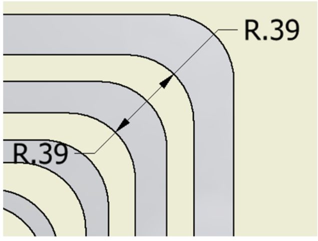

Figure 5-7 Top-down view of the round corner design of square coil (mm)

For the double-layer coils, the parasitic capacitance between two conductive layers depends on the width of the overlap area. In equation 4.17, it is shown that C_{pd} can be decreased by reducing the width of the overlap area, as illustrated in Figure 5-8.

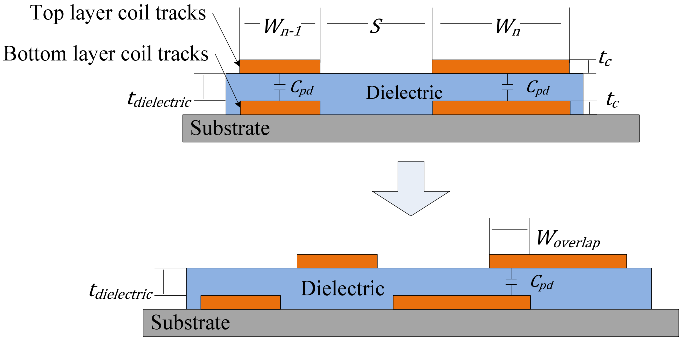

Figure 5-8 A design for reducing the width of overlap area

The double layer coil designs for variable width square coil with a minimised overlap are shown in Figure 5-9. The dielectric layer is not shown in Figure 5-9 to show the position of two conductive layers more clearly, the dielectric layer will be printed between the top and bottom conductive layers to isolate them.

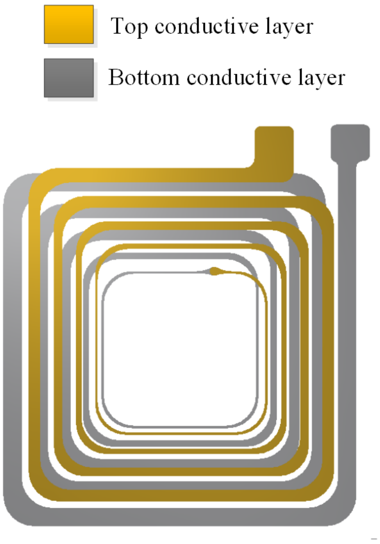

Figure 5-9 The double layer designs of square coil and circular coil

The overlap area can be reduced from 52.15 cm^2 to 10.82 cm^2 for the square coil design with variable width of track. The reduction of overlap area can gives 79.3% drop down in C_{pd} theoretically. The same configuration for minimise the overlap area between two conductive layers is applied on the circular coil, since the track of circular coil has same radius in every turn, the improvement is limited as the overlap area can only be reduced from 40.96 cm^2 to 26.32 cm^2, which achieve a 35.7% drop down on C_{pd}. For the coils with constant width of track, the spaces between tracks are smaller than they are in the design of the coils with variable width of track. Only approximately 10% drop down on C_{pd} can be achieved, but it increases approximately 55% on DC resistance compare the coils with constant width track with ones have variable. The variable width track is perfectible on the design of the square coil with double conductive layer structure. The circular coil with double conductive layer structure has the limitation on its electrical characteristics, only the designs of the circular coil with constant width track and single conductive layer structure and the square coil with variable width track and double conductive layer structure will be fabricated in this thesis.

5.5 Circuitry Design for Flexible Coils

The electrical characteristics of a coil depend upon the physical parameters of the materials and geometric layout, and these electrical characteristics must be considered for the circuit design. The flexible coils are not inherently matched with the Qi standard driver and receiver circuits used in this thesis, so they must be tuned to a matching operating frequency within the range between 100 kHZ to 200 kHz [101] to make them compatible with driver and receiver circuit. Consequently, resonant tank capacitors between the driver and TX coil as well as between the RX coil and receiver, are constructed to tune the TX and RX coils to the operating frequency. The circuit layout of the resonant tank capacitors for the TX and RX coils is shown in Figure 5-10 where equivalent load resistance, Z_{TX}, is the impedance looking into transmitter load network and Z_{RX} is the impedance looking into receiver load network.

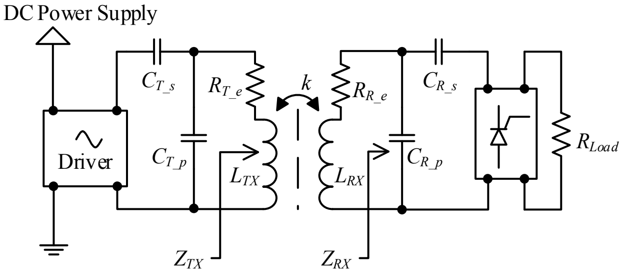

Figure 5-10 Resonant tank capacitors for coils

The resonant tank capacitors for the TX coil are constructed by a parallel capacitor C_{T_p} and a serial capacitor C_{T_s}. The parallel capacitor is optimised for a flexible coil, and is used to compensate for the varying of inductance of a flexible coil when it is bent. The serial capacitor dictates the resonant frequency of the coil and results in a low output impedance. The resonant tank capacitors for the RX coil has the same structure, being constructed from a parallel capacitor C_{R_p} and a serial capacitor C_{R_s}. The dimensions of the coils were defined in Section 5.4, and the theoretical electrical characteristics of printed coils were used to analyse the resonant tank capacitors. The values of the resonant tank capacitors are determined by following method:

1. Set the maximum constraint of Z_{TX} based on the maximum output power of the driver circuit with the load of application.
2. Set the minimum loaded Q of circuit for driver circuit with driving voltage V and current I, based on L_{coil}, R_{coil} and unloaded Q of coils, the optimal loaded Q is calculated from equation 5.2:

$$Q_{load} = \frac{Q_{unload}V\sqrt{{L_{coil}}^2 + {R_{coil}}^2}}{I{R_{coil}}^2 + V\sqrt{{L_{coil}}^2 + {R_{coil}}^2}} \tag{5.2}$$

3. Calculate the capacitance C_r required for a particular resonant frequency using equation 4.26.
4. Calculate the 20dB impedance at the resonant frequency point, take capacitance value for the serial capacitor for TX coil C_{T_s} at the point with rising edge (an example as shown in Figure 5-11), which results in an increasing trend of reactance with increasing load resistance and keeping the resistance relatively the same, and will prevent the power lost from the resonant frequency mismatch.

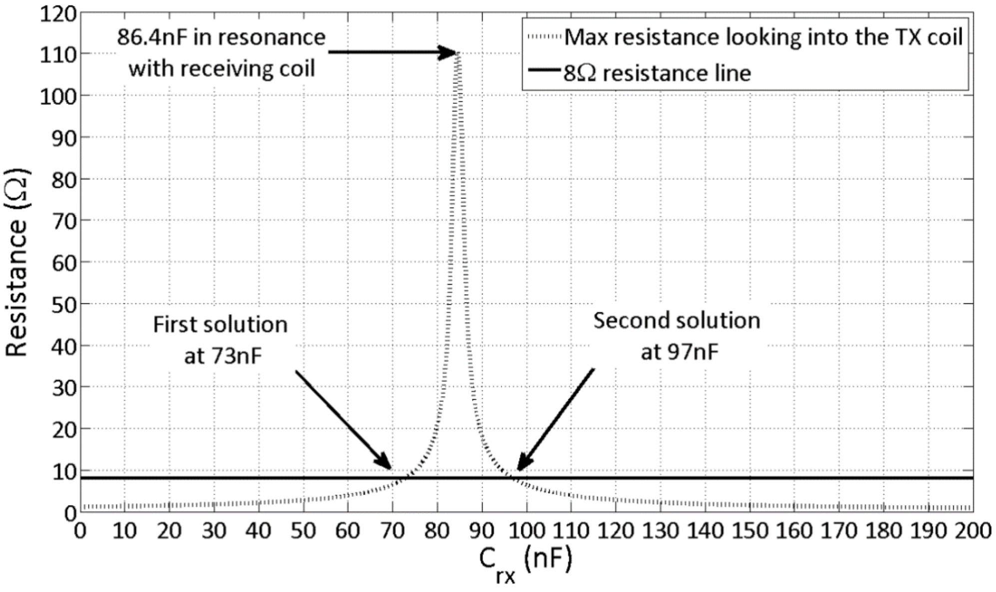

Figure 5-11 Resonant tank capacitors for coils

5. Calculate the parallel capacitor for TX coil, C_{T_p}, based on equation 5.3:

$$C_{T\_p} = C_r - C_{T\_s} \tag{5.3}$$

6. Calculate the minimum phase angle θ of Z_{RX} from the receiver circuit for conjugate based on equation 5.4:

$$cos\theta = \frac{R_{R\_e}}{Z_{RX}} \tag{5.4}$$

7. Calculate the parallel capacitor for the RX coil based on equation 5.5:

$$C_{R\_p} = Z_{RX} sin\theta \tag{5.5}$$

8. Calculate the serial capacitor for RX coil based on equation 5.6:

$$C_{R\_s} = \frac{1}{\omega^2 L_{RXcoil}} - C_{R\_p} \tag{5.6}$$

The coils are tuned at 195 kHz, this frequency is less than one tenth of the theoretical self-resonant frequency of the coil (17.8 MHz, calculated from equation 4.19) and is in the range of Qi standard operating frequencies. The impedance looking into receiver load network Z_{RX} is very close to the DC load resistance after the rectifier as very little energy is lost on high efficiency schottky diodes receiver rectifier, and Z_{RX} should be larger than 20 Ω based on the wearable applications. Table 5-1 shows the design values to make the coil compatible with the

Qi WPT system, which is calculated based on the discussions in Chapter 4 and the designs in Section 5.4. These values are the impedance looking into the transmitter load network Z_{TX}, the inductance of the designed coil L_{coil} , the resonant tank capacitors for both TX and RX coils C_{T_s}, C_{T_p}, C_{R_p}, and C_{R_s}.

Table 5-1 Parameters for the driver circuitry design from theoretical calculation

Parameter	Value	Equation
Z_{RX} (Ω)	20	4.25
Z_{TX} (Ω)	45	4.28
L_{coil} (μH)	4	4.5, 4.6
C_{T_s} (nF)	220	4.26
C_{T_p} (nF)	3.3	5.3
C_{R_s}(nF)	220	5.5
C_{R_p}(nF)	3.3	5.4

These parameters give the initial values of the components to build a WPT system. The values should be modified depending on the different coils, whereas each different flexible coil sample has variable electrical characteristics due to the printing fabrication process, it is necessary to adjust this and thereby ensure the circuit operates at its maximum efficiency.

5.6 Summary

In this chapter, the materials for substrates and screen printable pastes have been investigated. Three different kinds of substrate with different levels of printability have been described. This will allow prototyping on an easily printable rigid substrate to give a proof of concept and allow comparison with later work on flexible substrates. The coils will be printed in the order of on alumina, Kapton and interface-coated textile.

Pastes have been selected for the interface layer (Fabink-UV-IF1), dielectric layer (Fabink-UV-IF1) and conductive layer (Fabink-TC-AG4002), with the selected pastes having been verified by other research.

Two shapes for the coils have been designed based on theoretical calculations and the requirements of the application. Different designs of coils are investigated and selected by considering their electrical characteristics. The selected designs are the circular coil with constant width track single conductive layer structure, and the square coil with variable width track double conductive layer structure. These designs were created by using CAD software and then screens were manufactured for screen printing. Finally, resonant tank capacitors have been designed for flexible coils to be deployed in the WPT system, and theoretical values for passive components have calculated.

The achievable coil properties are calculated by theoretical calculation, the circular coil with constant width track single conductive layer structure should have 4 μH of inductance, 20 pF of parasitic capacitance, 17.8 MHz self-resonant frequency, 80 of unloaded Q factor. The square coil with variable width track double conductive layer structure should have 10 μH of inductance, 80 pF of parasitic capacitance, 5.6 MHz self-resonant frequency, 60 of unloaded Q factor.

The highest unloaded Q factor of designed coil is 80, which is 20% smaller than the unloaded Q factor a typical wound copper coil has. It is limited by the conductivity of printable conductive paste. The low unloaded Q limits the loaded Q factor of driver circuit, which raises the challenge on the circuit design for high efficiency WPT system. Based on the designed dimensions of printed coil, a coupling factor of 0.6 between TX and RX coils is established for the coils' separated distance of 10 mm, which is less than 10 % of the diameter of these identical coils, in the wearable applications.

6 Experimental Results of Flexible Printed Coils

6.1 Introduction

In this chapter, the fabrication process and experimental results of printed coils are discussed. The surface smoothness and the thickness of printed coils with different structures are examined. A suitable conductive layer curing temperature and duration are selected to provide a homogeneous cured layer at a temperature the textile can endure. After printing and curing, electrical characteristics of the coils are measured, and compared with the theoretical model and calculations provided in Chapters 4 and 5 to verify the fabrication. The flexibility of the printed coil on interface-coated textile is discussed. The coils are fabricated successfully, and then deployed in a WPT system to examine the functionality of them. The output power and DC to DC efficiency are measured of the WPT system using either coupled printed coils or other combinations of coils to verify and compare the performance of printed flexible coils.

6.2 Screen Printed Fabrication

6.2.1 Interface Layer

A woven textile typically has a rougher surface than Kapton. Consequently, it is necessary to print an interface layer on the textile to create a smooth surface for the printing of subsequent conductive layers with uniform thickness and to prevent the issues caused by the gaps between the textile fibres as discussed in Section 5.3.1. An interface layer composed of selected Fabink-IF-UV4 is printed on standard 65/35 polyester/cotton fabric to achieve this smooth surface.

Varying the number of wet deposits in each sub-layer and the total number of cured sub-layers varies the thickness of the resulting interface layer. The thickness of each wet printed deposit is determined by several printing parameters (the speed and pressure of the squeegee and the snap off distance), physical properties of the paste (viscosity surface tension, evaporation rate, suspension stable, and particle size), and screen properties (open area of screen mesh and thickness of screen emulsion). The screen emulsion thickness is the main factor controlling the thickness of the wet printed deposit of one paste. A factor in determining the thickness of a single cured sub-layer is the rate of shrinkage of the paste during curing. Further, each sub-layer has a different thickness due to the limitation of the surface tension of a printed paste, the flowing of the printed paste to a lower level such as the outside of lower cured layer, and the change in distance between the top of the printed structure and the screen mesh as more cured layers are added, this distance cannot be controlled precisely as constant since a measurement of this distance is unavailable during the printing process. These variations of thickness in each sub-layer are examined here.

A screen with a 40 μm emulsion thickness and 2 μm diameter stainless steel mesh filaments is used for printing and examined, a resulting 38 μm wet thickness for one deposit is expected. The non-contacted method of measuring the thickness of a wet layer is demanding and time consuming, but the contacted method like using a micrometre can easily damage the profile and surface of this layer. The thickness of the cured sub-layer infers the thickness of the wet printed deposit and the cured layer is the printed result of the fabrication, the thickness of cured sub-layer is measured and used to examine the thickness of a wet printed deposit.

After each print, UV curing is performed for 60 seconds at an intensity of 50 mW/cm^2. The thickness of the cured layer is then measured using a non-contact method. Normally, thicknesses on the order of microns are measured by a micrometre, but this contacts the sample, which can be detrimental to the structure of subsequent layers. A Nikon eclipse LV 100 microscope with a Nikon LU Plan Fluor 100 × / 0.90 lens is used to perform a non-contact measurement. Since the thickness of such object is also the vertical distance shift of the objective stage between the focal point for the bottom and top of the measured layer, by recording the movement of the stage, the thickness can be measured.

Table 6-1 shows the overall thickness of interface layers on textile with varying numbers of cured sub-layers, and for the layer with a same number of cured sub-layer, the effect of varying the number of wet deposits consisted in each cured sub-layer on thickness is examined. The practical thickness is compared with the expected thickness from data given by the manufacturer, the variation in achieved thickness is calculated based on the measurement of multiple different samples and this variation is caused by the admissible fabrication error.

Table 6-1 The number of deposits per layer, the number of cured sub-layers and the resulting thickness of the interface layer

Wet Deposits	Cured Sub-layers	Expected Thickness of Interface Layer (μm)	Achieved Thickness of Interface Layer (μm)
4	2	34	30 ± 56%
6	2	42	38 ± 50%
4	3	51	45 ± 44%
6	3	63	54 ± 40%
4	4	68	65 ± 23%
6	4	84	75 ± 20%
4	6	85	84 ± 11%
6	6	105	96 ± 10%

The table shows that the measured thickness of all samples which are lower than expected is within one standard deviation in all cases. The thickness of a cured interface layer with 3 sub-layers is 7% greater than half the thickness of a layer with 6 sub-layers. This means that the thicknesses of upper sub-layers are lower than the thickness of lower sub-layers, due to the reduced separation between substrate and screen mesh when the upper sub-layers are printed. As more sub-layers of the interface are added, the thickness increases and the standard deviation of thickness is reduced, and consequently the roughness is reduced. The reduction in roughness as more sub-layers are added can be observed without magnification. An acceptable smooth surface with 6 sub-layers of interface (left side) and an unacceptable rough surface with 2 sub-layers (right side) are shown in Figure 6-1 with demo conductive printed layer. It can be seen that the issues are occurred when printed a functional layer on a rough surface such as disconnections and the pattern losing.

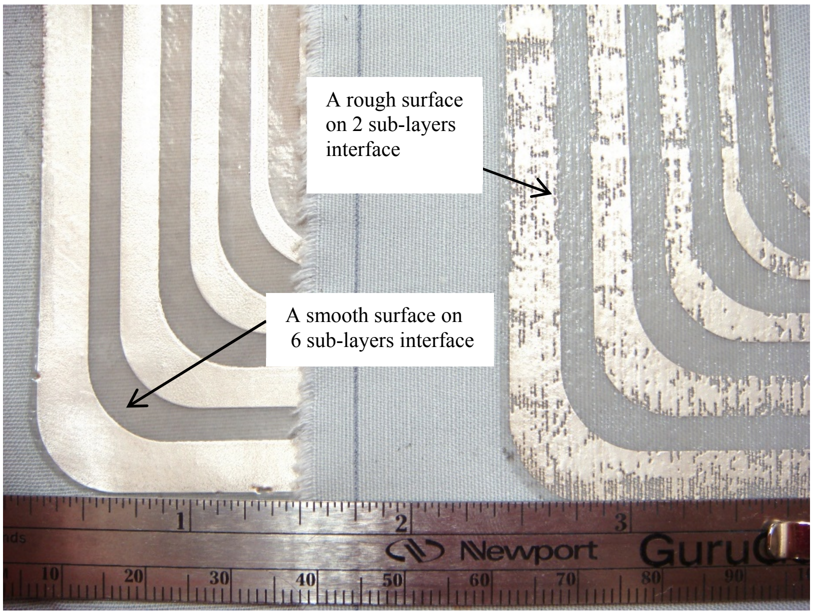

Figure 6-1 Comparison of surface roughness of interface layer with different numbers of sub-layers.

Based on SEM measurements it can be concluded that the maximum diameter of surface defects is less than 5 µm with a 6 sub-layer (4 wet deposits per sub-layer) interface. The SEM micrograph in Figure 6-2 shows that this interface layer provides a smooth surface for printed conductive layers on textiles.

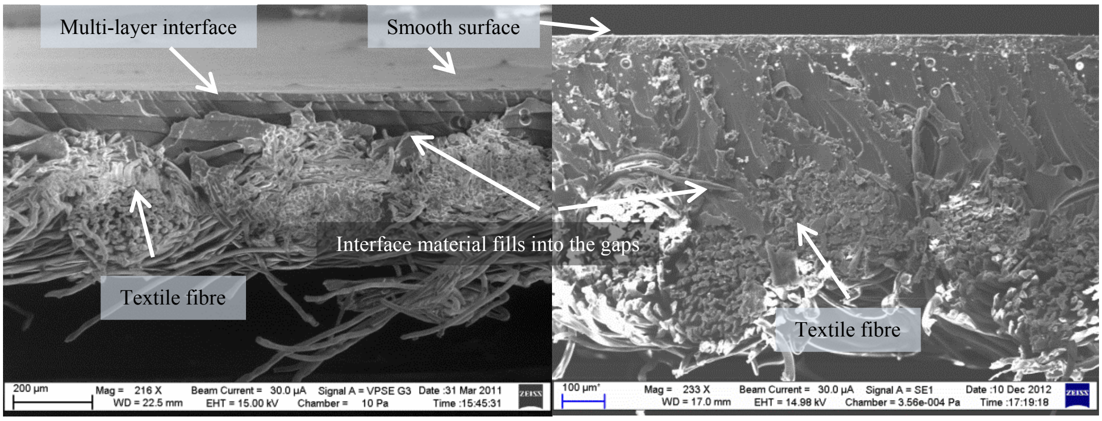

Figure 6-2 SEM micrograph of an interface layer on 65/35 poly-cotton textile.

6.2.2 Thermal Curing Duration of Conductive Layer

As discussed in Chapter 5, different coil shapes with either one or two layers of conductive layer structures are printed to fabricate coils with the theoretical required inductance. The resistance should be as low as possible to reduce the losses in printed coils and maximise power transfer efficiency. The curing temperature and duration for the conductive layer are those recommended by the manufacturer of silver paste to achieve minimal resistance, the fabrication process used in this thesis is different from the processes employed in industry because of the large print areas used in this work, approximate 200 cm^2. Consequently, the relationship between the curing duration and cured resistance of the screen printed coils is examined in this work.

The planar coil is formed of a printed conductive track. Here this track layer is printed on to substrates of alumina, Kapton and interface-coated textile. Issues with bubbles in this layer occurred in some printed samples on interface-coated textile when a relatively larger area of conductive layer is covered by a dielectric layer. The conductive layer cures further during the curing process for the dielectric layer, and causing bubbles. This is caused by incomplete curing during the conductive layer curing process. To solve this problem, an appropriate curing duration is selected for areas larger than 100 cm^2 (the design printed coil area as mentioned in 5.3.2) of conductive printing to give the optimised conductivity of conductive track without bubbles, based on identifying a relationship between curing process and resistance. Since the textile can endure a maximum 130 °C curing temperature curing at a higher temperature is not an option, so curing at 130 °C with increased curing durations was performed. The required curing duration could be longer than the 10 minutes recommended by the manufacturer. No significant damage to the textile is observed during the curing of a single conductive layer, the discoloration of the textile is occurred when the curing duration longer than 30 minutes at 130 °C but no break or burn. In its uncured liquid state the conductive paste contains a solvent which has higher resistivity than the conductive silver particles in selected Fabink-TC-AG4002 silver paste from Smart Fabric Inks Ltd as described in Chapter 5. Consequently, the DC resistance of a conductive track decreases as solvent evaporates throughout the curing process. The DC resistance of a track is therefore an indicator of the completeness of the curing process.

In this test, a conductive sub-layer was printed with two wet deposits of Fabink-TC-AG4002 to form a coil shape on the selected substrate (Kapton or interface-coated textile) or lower cured conductive sub-layers and then cured at 130 °C for 5 minutes. The DC resistance is measured, then the coil is cured for another 5 minutes at the same temperature. This 5 minute measuring and curing process is repeated until the DC resistance of the coil stabilises, which indicates that it is fully cured. Figures 6-3 and 6-4 shows the reduction in normalized DC resistance of conductive tracks composed of one, two, four and eight sub-layers on Kapton and interface-coated textile, respectively.

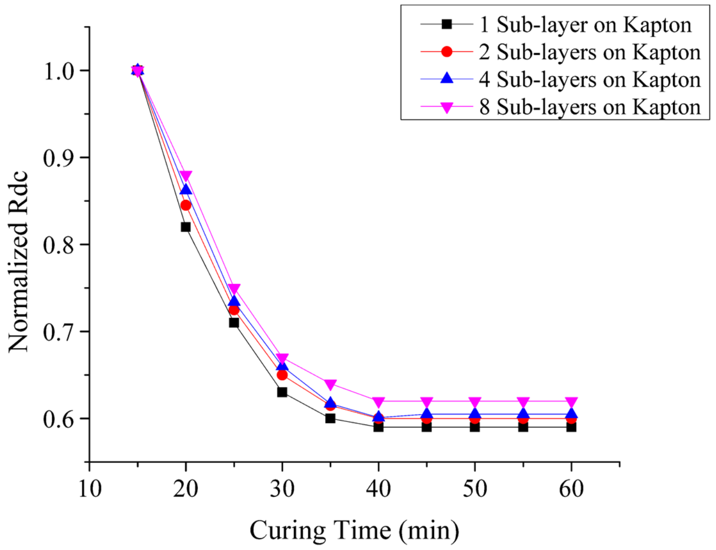

Figure 6-3 Normalized DC resistance against curing duration for conductive tracks with different number of sub-layers (different layer thickness) printed on Kapton

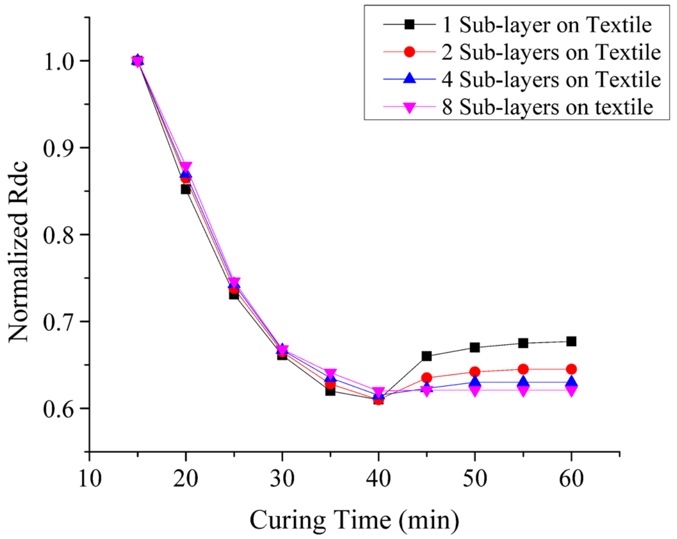

Figure 6-4 Normalized DC resistance against curing duration for conductive tracks with different number of sub-layers (different layer thickness) printed on interface-coated textile

On Kapton, the conductive track resistance stabilises after 40 minutes of curing, which means the conductive paste is fully cured. In cases where the thickness of the conductive layer is greater, upper conductive sub-layers with approximately the same thickness as lower sub-layers contribute less proportion of the total thickness (e.g. the second sub-layer approximately double the total thickness, but the third sub-layer increases 50% of the total thickness), as a result, thicker conductive layers have less resistance change during curing.

On interface-coated textile, tested sub-layers show consistent decreases in normalized DC resistance for curing times from 10 to 40 minutes, for curing durations over 40 minutes they show varying levels of increase in DC resistance. This occurs with all numbers of sub-layers, but the effect is reduced as the total thickness increase (as the number of sub-layers increases). The cause of this effect is due to interactions between the interface layer and the conductive layer which occur once the conductive paste is over-cured, comparative tests for the same conductive layer printed directly onto Kapton without an interface layer show no increase in DC resistance for curing durations over 40 minutes. The selected curing process for a 150 mm × 150 mm printed coil conductive layer is 40 minutes at 130 °C, which minimises the DC resistance and avoids increases due to over curing.

6.2.3 Bottom Conductive Layer

Based on the study described in Chapter 5, a circular coil has the highest Q for a single layer structure, and a square coil has the highest Q for double layer structures. Coils are printed in these two different shapes with various conductive layer thicknesses to examine the fabrication process, and furthermore, for the comparison of the coils performances when they are deployed in a WPT system in later experiments. Since the second conductive layer of a double layer structured square coil is printed on a dielectric layer covering on the first conductive layer, which is less smooth than the initial interface layer, the thickness varies between first and second layers. It is, however, unaffected by the printed shape. In this section the "bottom" conductive layer refers to both the first of two printed conductive layer coil track layers of the double layer structures square coil and also the coil track layer of the single layer structure circular coil, because they are printed on the same substrate form. The thicknesses of bottom conductive layers are measured, and then the relationship between these thicknesses and the sheet resistance of the tracks are examined.

The sheet resistance is calculated as $R_s = R_{DC} w / l$, where R_{DC} is the DC resistance measured by a FLUKE 179 multi-meter, and w and l are the length and width of the conductive track, respectively. The width is designed as w= 4 mm, and the length of track is easily obtained from CAD software as l = 2417 mm. In the datasheet of Fabink-TC-AG4002 conductive paste, the manufacturer gives a sheet resistance R_{sr} = 24 mΩ/□ with recommended thickness (t_r = 18 μm). The thickness of a printed conductive layer is thicker than the recommended thickness in this experiment because minimal DC resistance is desired. Consequently, a theoretical sheet resistance is calculated as $R_{sc} = R_{sr} t_r / t$, where t is the average thickness of conductive layer measured by using the same method as was used in the measurement of the thickness of interface layers. These calculated sheet resistances R_s are compared with the theoretical sheet resistance R_{sc} to verify that the sheet resistance on the samples is as expected. The thicknesses, theoretical sheet resistance, DC resistance and calculated sheet resistance of single layer coil form conductive layer are listed in Table 6-3. Each cured sub-layer has two deposits, and they are printed on different substrates which were described in Section 5.2. The given standard deviation of thickness is calculated based on the measurements of five different samples.

Table 6-2 Thickness, theoretical sheet resistance, measured DC resistance and calculated sheet resistance of the single layer circular coil printed on alumina, Kapton and interface-coated textile

Substrate	Cured Sub-layers	Thickness (µm)	Theoretical R_{sc} (mΩ/□)	R_{DC} (Ω)	Calculated R_s (mΩ/□)
Alumina	1	22 ± 9%	19.6	12.1 ± 5%	20.0
	2	42 ± 7%	10.3	6.4 ± 3%	10.6
Kapton	1	23 ± 15%	18.8	11.6 ± 7%	19.2
	2	44 ± 8%	9.8	6.1 ± 6%	10.1
Interface-coated Textile	1	29 ± 16%	14.9	9.2 ± 9%	15.2
	2	56 ± 11%	7.7	4.7 ± 7%	7.8

In this table, the thicknesses of layers that are comprised of two sub-layers are up to 5% less than double the thickness of layers with single sub-layer. It means that the thickness of second layers is thinner than the first sub-layer, due to previously discussed variation in the substrate and screen separation as more sub-layers are printed. As the second sub-layer of conductive track is printed, the thickness of the entire conductive layer increases and the standard deviation of thickness is reduced, consequently the roughness and the DC resistance are reduced, because a conductive layer with a homogenous cross section increases the uniformity of resistance. The conductive layer printed on the alumina is the thinnest, followed by Kapton and then interface-coated textile. Alumina has the smoothest surface, and interface-coated textile has the roughest, thicknesses of conductive layer is getting greater where the substrate they are printed on rougher. The calculated sheet resistance based on the measured DC resistance is higher than the theoretical sheet resistance, it shows that the DC resistance is higher than expected on all samples. The higher sheet resistance is caused by the practical thickness of printed conductive layer is thicker than the recommend one, and the fall in sheet resistance as thickness increases is not a linear function, rather than the principle of resistance for pure conductor, due to the mix of different resistivity between conductive binder and silver particle. These single layer coils are printed as shown in Figure 6-5 (a) on alumina, (b) on Kapton and (c) on interface- coated textile, respectively.

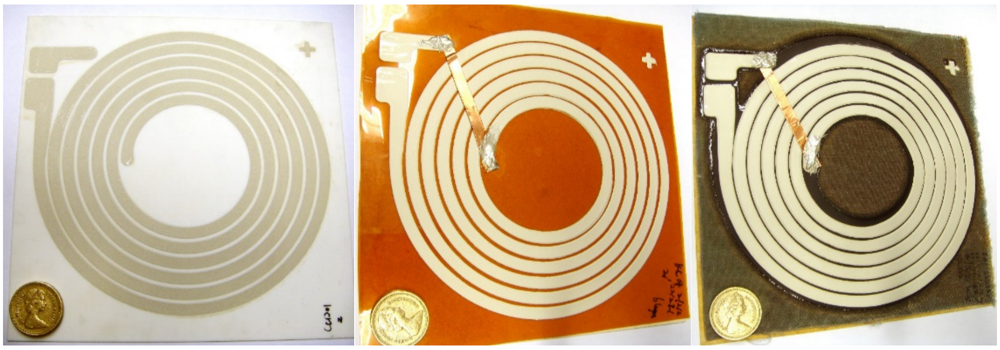

(a) (b) (c)

Figure 6-5 Single conductive layer structure circular coil printed on substrates of (a) alumina, (b) Kapton and (c) interface-coated textile

For the double layer structure square coil, where the dielectric layer and the top conductive layer were printed atop the bottom conductive layer, a smooth substrate surface is required for each layer. Consequently, no double sub-layers are printed for this layer, one sub-layer with two wet deposits is deployed in the bottom conductive layer to avoid it having a thickness greater than 30 µm, it is because that a large step changing (>30 µm) causes breaks on the upper printed layer along the direction of printing. Since it has a variable width of track, w/l can be obtained from CAD as 0.0015, which is lower than the 0.0017 in the circular coil design, and consequently, the square coil has a higher DC resistance than the circular coil when they have same sheet resistance. The coils were printed on to three substrate materials for comparison with previous experiments and the resulting thickness, theoretical sheet resistance, DC resistance and calculated sheet resistance are listed in Table 6-3.

Table 6-3 Thickness, theoretical sheet resistance, measured DC resistance and calculated sheet resistance of the bottom conductive layer of the double layer structures square coil printed on alumina, Kapton and interface-coated textile

Substrate	Thickness (µm)	Theoretical R_{sc} (mΩ/□)	R_{DC} (Ω)	Calculated R_s (mΩ/□)
Alumina	25 ± 7%	17.3	13.4 ± 5%	20.1
Kapton	28 ± 9%	15.4	11.5 ± 6%	17.2
Interface-coated Textile	28 ± 12%	15.4	11.9 ± 9%	17.8

In this table, the thickness of layers printed on Kapton and interface-coated textile are 10% thicker than the layer printed on alumina, and the variation on the thickness of the layer printed on interface-coated textile is 3% greater than the layer with same thickness printed on Kapton. It can be concluded that the same discrepancy between theoretical sheet resistance and calculated sheet resistance occurred as with the conductive layer printed in a circular form, this decreased conductivity compared to the theoretical value is not affected by what shape the conductive layer has.

6.2.4 Dielectric Layer

The dielectric layer provides a smooth surface for the printing of the top conductive coil layer, and provides electrical isolation and spacing between the bottom and top coils. The dielectric layer increases the distance between the two conductive layers, and consequently limits the parasitic capacitance, but also reduces the flexibility of the coil. The thicknesses of dielectric layers on various substrates are listed in Table 6-4, the variation in each achieved thickness is calculated based on the measurement of five samples for each substrate and this variation is caused by the admissible fabrication error.

Table 6-4 Thickness of the dielectric layer on alumina, Kapton and interface-coated textile substrate coils

Substrate	Deposits	Cured Sub-layers	Entire Thickness (μm)
Alumina	6	3	22 ± 5%
	4	4	34 ± 5%
Kapton	6	3	27 ± 9%
	4	4	33 ± 6%
Interface-coated Textile	6	3	25 ± 12%
	4	4	34 ± 7%

In this table, the dielectric layers which have 4 cured sub-layers with 4 wet deposits in each sub-layer are 23%, 18%, and 26% greater in thickness than the layers have 3 cured sub-layers with 6 wet deposits in each sub-layer on the substrates of alumina, Kapton and interface-coated textile, respectively, it also shows that the samples with 4 cured sub-layers have smaller variation (3% for Kapton and 5% for interface-coated textile) on the thickness of dielectric than the samples with 3 cured sub-layers. A cross-sectional SEM micrograph of the dielectric layer is shown in Figure 6-6, which shows a sample which has 4 cured sub-layers of dielectric material on Kapton between two green lines, this dielectric layer isolates the bottom and top conductive layers from one another.

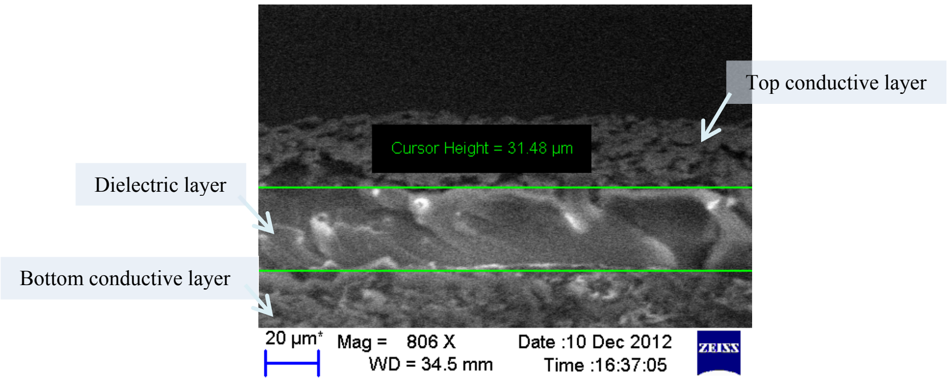

Figure 6-6 SEM image of the dielectric layer

A dielectric layer thicker than 50 µm is needed to keep the parasitic capacitance lower than 25 pF in a double layer structure square coil, but this increased thickness will lower the flexibility dramatically. Single conductive layer coils could be a better choice for a wearable application because no dielectric layer is required and the flexibility can therefore be retained.

6.2.5 Top Conductive Layer

For the coils with the double conductive layer structure design, the top conductive layer spirals out from the inner end of the bottom conductive layer as shown in Figure 5-9. There is one small circle (Ø 5 mm) on each inner end of both bottom and top conductive layer coils, and at the same position, the dielectric layer has a via hole (Ø 6 mm), this design implements an electric connection between two conductive layers to construct as one coil and other area is isolated by the dielectric layer to prevent any short circuit. In the processes of screen printing, alignments between bottom conductive layer, dielectric layer and top conductive layer are required to keep the inner end circles and via hole in the same position to achieve the electric connection.

The substrate, the bottom conductive layer and the dielectric layer can be seen as a whole part which provide a surface to print the top conductive layer on, a small variation of thickness is desired to perform a fine printing of the top conductive layer. The steps of the bottom conductive layer track varies the thickness of this whole part, consequently, the thickness of the bottom conductive layer is limited as described in Section 6.2.3. The top conductive layer is therefore printed on to a more irregular surface comparing with the substrate surface which the bottom conductive layer printed on, which causes thinning of the top conductive layer immediately above each bottom conductive line, thus increasing the risk of break of top conductive layer. To get a desired thickness, one solution is applying four wet deposits in one cured sub-layer, another solution is printing another conductive sub-layer. As the results, the top conductive layer was printed successfully on the samples built on alumina and Kapton.

Neither solution could be used to provide a satisfactory top conductive coil layer on the samples with an interface-coated textile substrate, due to the fact that bottom conductive and dielectric layers have up to 3 mm shrinkage in the horizontal and up to 2 mm plastic deformation in the vertical directions and are not suitable as a substrate to print the top conductive coil layer onto. The drawbacks of high parasitic capacitance, high DC resistance, low flexibility, and low reproducibility make the double conductive layer structure on an interface-coated textile unsuitable as a coil for wearable WPT. So the top conductive layer was only printed on the samples on alumina and Kapton substrates for comparison but not on interface-coated textile. After printing and curing, the thicknesses of top conductive layers are measured using the microscope, w/l is obtained from CAD drawings as 0.0013, and the DC resistances are measured by multi-meter, the theoretical and calculated sheet resistance can be calculated. There parameters are listed in Table 6-5, each cured sub-layer contents 2 deposits. Relatively, the AC resistance of the coil will be discussed in Section 6.3.1.2.

Table 6-5 Thickness, theoretical sheet resistance, measured DC resistance and calculated sheet resistance of the top conductive layer of the double conductive layer structures square coil printed on alumina, Kapton and interface-coated textile

Substrate	Cured Sub-layers	Thickness (μm)	Theoretical R_{sc} (mΩ/□)	R_{DC} (Ω)	Calculated R_s (mΩ/□)
Alumina	1	24 ± 21%	18.0	15.9	20.7
	2	50 ± 10%	8.6	7.8	10.1
Kapton	1	23 ± 19%	18.8	16.5	21.4
	2	53 ± 11%	8.1	7.4	9.6

A second cured sub-layer in the top conductive layer increases its thickness dramatically and decreases its surface roughness. Compared with the average thicknesses of the bottom conductive layer, which are 25 μm ± 13% for single sub-layer and 47 μm ± 9% for double sub-layers, the top conductive layers have larger variation in thickness (24 μm ± 20% for single sub-layer and 52 μm ± 11% for double sub-layers). The thickness of the top conductive layer decreases the flexibility of the device, and the rough surface reduces the uniformity of resistance and the conductivity of printed coil. The practical sheet resistances are higher than theoretical value on all samples, it is caused by the practical thickness is greater than the recommend one, as the same issue occurred in bottom conductive layer. Figure 6-7 shows bottom conductive layer, dielectric layer, and top conductive layer of these coils printed on (a) alumina and (b) Kapton respectively.

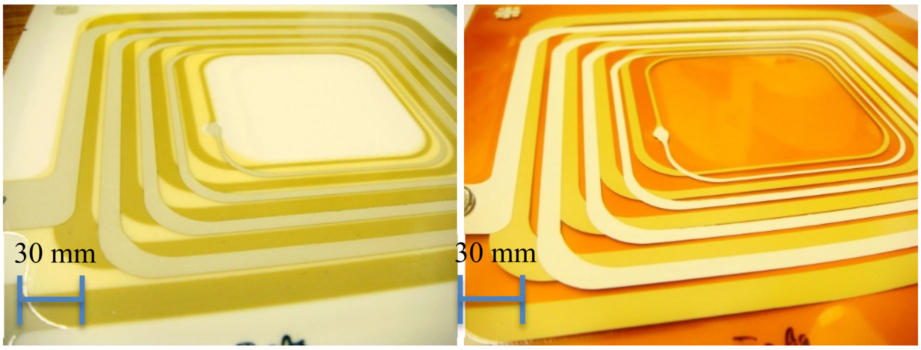

(a) (b)

Figure 6-7 Double layer structure square coil printed coil on (a) alumina and (b) Kapton

After the top conductive layer is printed and cured, the coil with double conductive layer structure is completed only on the substrates of alumina and Kapton, the screen printing fabrication process has been verified for single conductive layer structure coil printed on flexible interface-coated textile which is suitable for the wearable WPT applications.

6.3 Screen Printed Coils

6.3.1 Electrical Characteristics of Printed Coils

As noted in Chapter 4, the following six essential electrical characteristics are key parameters to characterise the performance of a coil for WPT:

- DC resistance,
- AC resistance,
- Inductance,
- Self-resonant frequency (SRF),
- Parasitic capacitance, and
- Unloaded Q factor.

A WAYNE KERR 6500B impedance analyser can analyse parameters at a range of frequencies from 20 Hz to 10 MHz. The AC resistance, inductance, self-resonant frequency and unloaded Q factor can be directly measured using this impedance analyser. According to [184], the parasitic capacitance can then be calculated based on the inductance and self-resonant frequency of the coil. As the range of operating frequencies of coils for a WPT application is from 100 kHz to 6 MHz [185], analysis at frequencies above 10 MHz is not critical. For some tested coils which have a SRF higher than 10 MHz, a Rhode & Schwarz ZVB 4 vector network analysis, which has a frequency range from 300 kHz to 3 GHz, was used to analyse the impedance phase angle to measure the SRF. The unloaded Q factor of coils can be calculated based on the DC and AC resistance, inductance, and parasitic capacitance at a given frequency, which can be used to compare with the result directly measured by the WAYNE KERR 6500B impedance analyser and will be discussed in Section 6.3.1.5.

To relate the performance of a printed coil in a WPT application to these six characteristics, two other type of coils are introduced. One is the flat air core spiral coil wound with 1.2 mm diameter copper wire, it has the same equivalent diameters (d_{avg}= 93 mm , Δ= 0.484) of the printed coil as described in Chapter 4. The other one is a copper tape based coil formed on paper with the same planar as the printed coil, this copper tape has a thickness of 40 μm (18 % of the printed coil) and a resistivity of 16.8 nΩ·m, that the resistance of this copper tape coil is one tenth of the resistance which the printed coil has.

All coils in this paper have these six parameters measured under the same environmental conditions, so that their behaviour in an application can be compared to theoretical calculation. The resonant tank capacitors are calculated as described in Section 5.5 based on the parameters of each coil. The particular value of capacitance can be added by using industrial standard value of the polypropylene film capacitors, which have lowest dielectric absorption and are suitable for the compensation of inductive coils.

6.3.1.1 DC Resistance

The DC and AC resistances consume power when the current flows into the coil, so a low DC resistance is expected and can be achieved by increasing the thickness of conductive layer of coils as described in Section 6.2, an acceptable thickness is therefore determined by considering the flexibility of the wearable coils. For a coil with a given width and length of printed track, and made from the selected conductive paste Fabink-TC-AG4002 with 24 mΩ/□ sheet resistance, the thickness of printed track is the only variable that affects the DC resistance. The thickness of a printed conductive layer varies because the printing process causes anisotropic structural effects on the printed layer, determined by factors of direction of travel and pressure applied by the squeegee. By adding more conductive sub-layers, different thicknesses of conductive layer can be printed, conductive layers in this section are thicker than those described in Sections 6.2.3 and 6.2.5, verification of screen printed fabrication, because a low DC resistance of approximately 1 Ω is essential to achieve acceptable efficiency in WPT systems. The theoretical DC resistance and measured DC resistance of printed coils with a single conductive layer structure spiral coil track are shown in Figure 6-8. Four different numbers of conductive sub-layers are examined. Standard deviations of thickness and resistance are calculated based on ten measurements of three different samples of each sub-layers number. The theoretical DC resistance is calculated as described in Section 4.3.2.

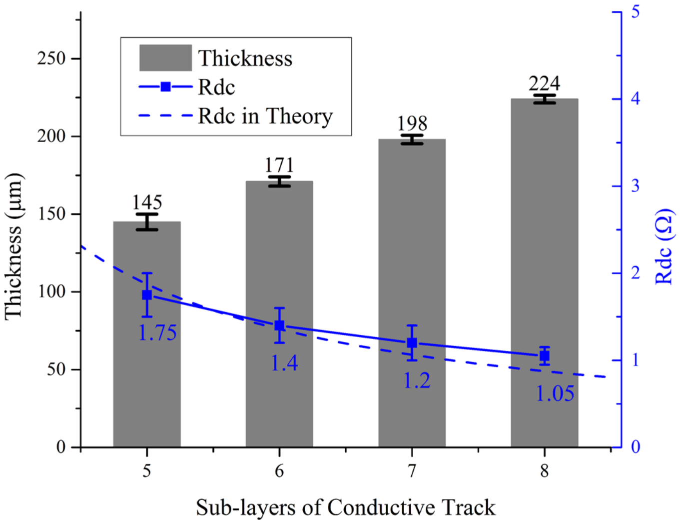

Figure 6-8 Thickness and practical DC resistance of circular coils with single conductive layer structure compared with theoretical DC resistance in different thicknesses

The relationship between DC resistance and the thickness of conductive layer is a continuous function on the closed interval from the minimal thickness to the maximal. Figure 6-8 shows that the practical DC resistance of a printed coil conductive layer is within -15% to +10% of the theoretical calculation. One reason for the discrepancies is the variation in the thickness of the printed conductive layer at different points over its pattern as described earlier. Another reason is the difference in thickness between the layers printed here and the manufacturer’s recommend thickness due to the fact that a low DC resistance is a priority. Despite these discrepancies, the practical DC resistances of all samples is within an acceptable margin of theoretical values.

The thickness of approximately 220 µm is required to achieve a DC resistance of approximately 1 Ω for a conductive layer of the printed coil. Printing such a thick layer prohibits the use of another conductive layer after the dielectric coating as the surface is too uneven. Consequently, a coil with the double conductive layer structure could not be fabricated with as low DC resistance as a coil with single conductive layer structure. Figure 6-9 shows the thickness and practical DC resistance of square coils with double conductive layer structure and variable width compared with theoretical DC resistance. Four different thicknesses obtained with different numbers of cured sub-layers are examined.

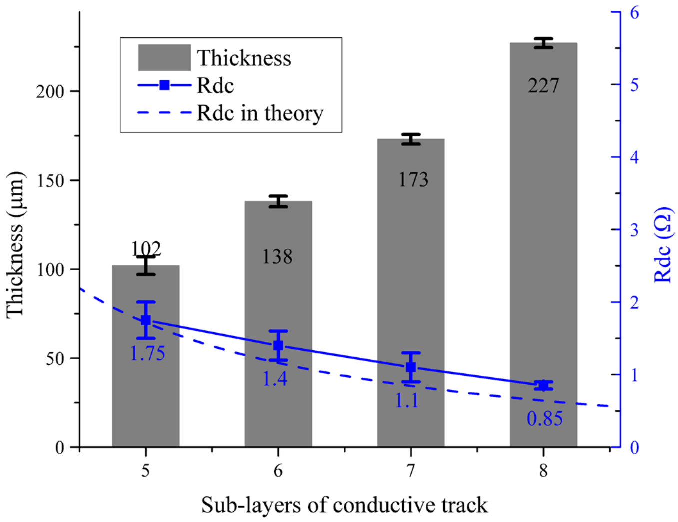

Figure 6-9 Thickness and practical DC resistance of square coils with double conductive layer structure compared with theoretical DC resistance in different thicknesses

The DC resistances of all sample coils with double conductive layer structure follow the theoretical calculations, but the drawback of higher resistance compared with coils with a single conductive layer structure makes the design of double conductive layer structure unsuitable for WPT because the conductive paste used to produce the flexible coil limits the sheet resistance.

In both theoretical calculations and practical measurements, a conductive track with more than eight sub-layers has limited improvement on DC resistance as the thickness is approximately 220 µm. In the practical fabrication of a flexible coil, it is difficult to correctly align eight sub-layers, and a conductive layer with a thickness greater than 220 µm reduces the flexibility of a coil on interface-coated textile. In summary, a single layer coil composed of a conductive track with 8 sub-layers is selected for the WPT system in this thesis.

6.3.1.2 AC Resistance

When the alternating current passes through the conductive track, the AC resistance is caused by the skin effect and proximity effect, and is a function of frequency. A reasonable operating frequency range should be selected depending on the AC resistance of coils to limit the heating losses caused by current. The AC resistance of the wound copper coil, copper tape coil, printed coils with single and double conductive layer structures on Kapton are shown in Figures 6-10 to 6-13, respectively.

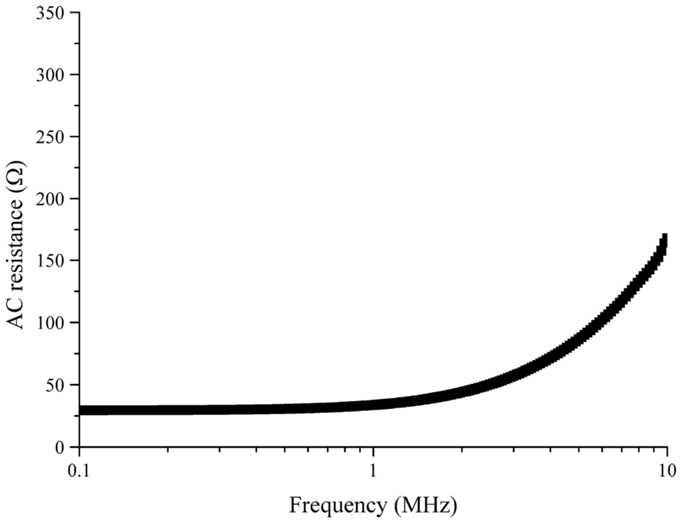

Figure 6-10 AC resistance of the wound copper coil as a function of frequency

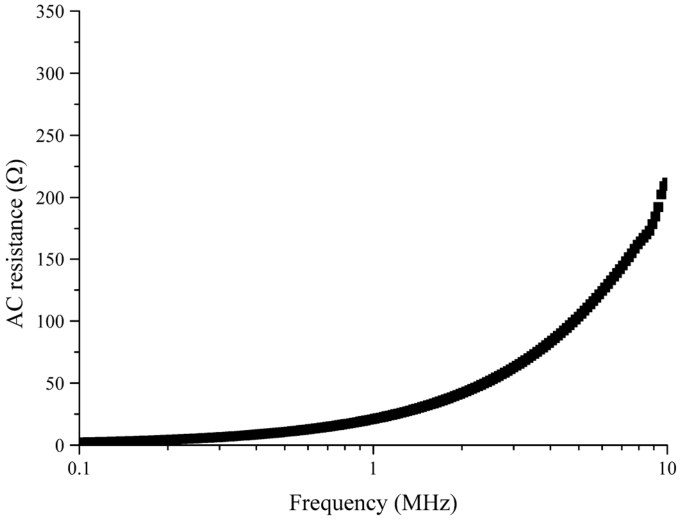

Figure 6-11 AC resistance of the single conductive layer structure copper tape coil as a function of frequency

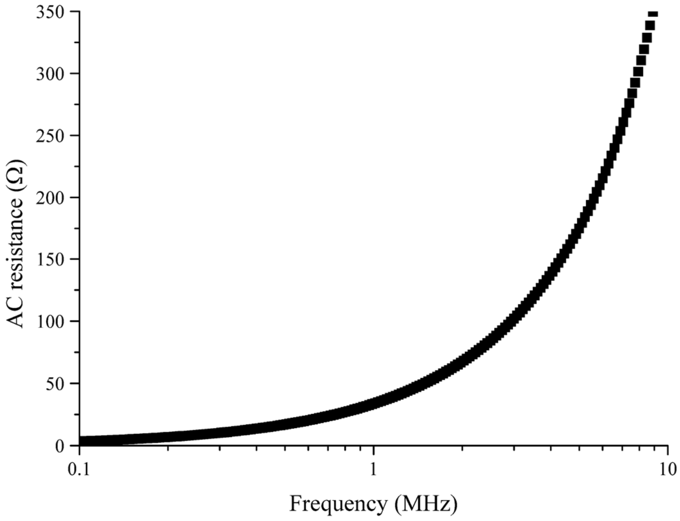

Figure 6-12 AC resistance of the single conductive layer structure printed coil on Kapton as a function of frequency

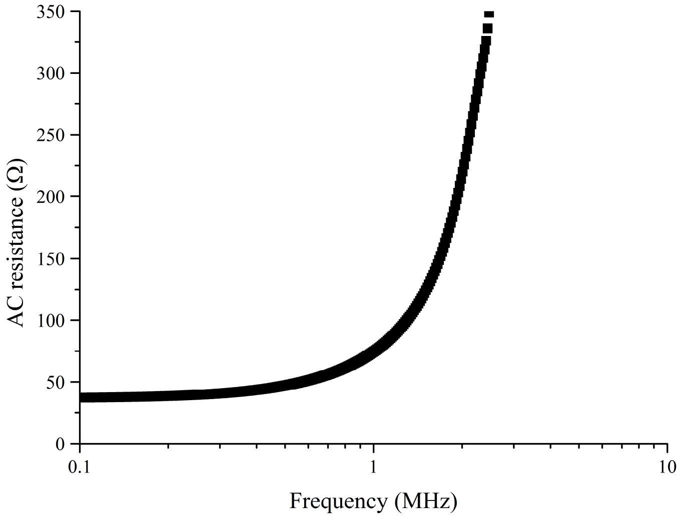

Figure 6-13 AC resistance of the double conductive layer structure printed coil on Kapton as a function of frequency

The AC resistance of the coil with the single conductive layer structure increases rapidly when the frequency is higher than 2 MHz, so the operating frequency for this single conductive layer structure coil should not be higher than 2 MHz. The double conductive layer structure coil has a peak of AC resistance at around 3 MHz, and the start of the sharp increase of AC resistance is at a frequency lower than 1 MHz, this gives a narrower range of operating frequencies with acceptable losses due to AC resistance than the coil with a single conductive structure. Table

6-6 shows the practical AC resistance of the wound copper, copper tape and printed coils measured at the designed 200 kHz operating frequency compared with the theoretical calculation described in Section 4.3.2.

Table 6-6 The practical AC resistance of different types of coils compared with the theoretical calculation

Coil Type	Structure of Conductive Layer(s)	Theoretical R_{AC} (Ω)	Achieved R_{AC} (Ω)
Wound Copper	N/A	6	6.1 ± 2%
Copper Tape	Single	6	5.9 ± 4%
Printed Coil on Alumina	Single	11.3	12.5 ± 12%
	double	37.8	37.6 ± 17%
Printed Coil on Kapton	Single	11.3	13.1 ± 11%
	double	37.8	37.4 ± 18%
Printed Coil on Interface-coated Textile	Single	11.3	12.0 ± 25%

In this table, the given standard deviations of practical AC resistance are calculated based on 10 measurements on 5 different samples of each type of coil. The error between the practical and theoretical AC resistance is no more than 5% in any case, which is within an acceptable margin. The printed coil on interface-coated textile has the largest deviation followed by the coil printed on Kapton, then alumina, this is due to the different level of deformation of each substrate. The double conductive layer structure introduce approximately three times the AC resistance of the coils with single conductive layer structures, due to the proximity effect that the magnetic field generated by a conductive layer effects substantially the current in another conductive layer within 50 µm. This high AC resistance in the coil with double conductive layer structure makes the device consume more power and thus reduces the efficiency. As the result, the coils with double conductive layer structure have a major disadvantage in terms of AC resistance.

6.3.1.3 Relative Permittivity of Interface Material in Dielectric Layer

In the coil with double conductive layer structure, the dielectric layer contributes a major part of the parasitic capacitance. The material used for the dielectric layer is Fabinks-UV-IF1, which is the same as the material used in interface layer to match the surface energy and tension, as described in Chapter 5. The permittivity of Fabink-UV-IF1 can be calculated as $\varepsilon_r =$

$(C \times d)/(A \times \varepsilon_0)$, where C is the capacitance of a sample, d is the thickness of the dielectric layer, A is the plate area, and ε_0 is the electric constant. In this experiment, each sample has known A= 1 cm^2 and d as measured in Section 6.2.4, the capacitance is measured using a TTi LCR400 LCR bridge. The capacitance, thickness and relative permittivity of printed coils on alumina and Kapton with double conductive layer structure are shown in Table 6-7. The standard deviation is calculated based on 10 measurements of 5 different samples of each type.

Table 6-7 Practical capacitance, thickness and relative permittivity of samples with dielectric material

Substrate	Thickness d (μm)	Capacitance C (nF)	Relative Permittivity ε_r
Alumina	22 ± 5%	1.66 ± 1%	41.2
	34 ± 5%	1.07 ± 1%	41.1
Kapton	27 ± 9%	1.35 ± 2%	41.2
	33 ± 6%	1.09 ± 1%	40.6

In this table it can be seen that the capacitance is increased when the thickness of the samples decreases, which conforms to the theoretical model of a capacitor. The relative permittivity of the dielectric material is approximately 41, and for the entire coil with A=10.82 cm^2 overlap area, the parasitic capacitance introduced by this double conductive layer structure could be up to 18 nF as calculated using equations 4.17 and 4.18.

6.3.1.4 Inductance, Parasitic Capacitance and Self-Resonant Frequency

The inductance of the coil allows the transfer of power wirelessly via inductive coupling between the transmitter and receiver coils. Inductance of the coil at its operating frequency is an essential parameter to tune the system correctly, the parallel combination of parasitic capacitance and inductance of the coil causes the self-resonance of a coil at a particular frequency, and the self-resonant frequency (SRF) is critical to a coil because the effective inductance is zero at the SRF, which prevents the alternating electromagnetic field being induced. The inductive connection between the coils cannot be made without an alternating electromagnetic field. Consequently, the inductance, parasitic capacitance and SRF are measured as following steps:

- Locate the SRF where the phase angle of the input impedance is zero (or Q is zero), crossing from inductive to capacitive.

- Read the inductance from the impedance analyser at a frequency of 1/10 of the SRF where the parasitic capacitance has negligible effect.
- Calculate the parasitic capacitance as $C = 1/4\pi^2 SRF^2$.

By comparing theoretical calculations (equations 4.5 and 4.6) with measurements from a preliminary test with wound copper and copper tape coils that have a given diameter, a reasonable error, less than ±5% was found when comparing the value of inductance between theoretical results for a flat coil and experimental measurements. This preliminary test verifies the experimental method, and the resulting electrical characteristics can be used in further tests.

Figure 6-14 shows the impedance phase angles against scanned frequencies of wound copper wire coil, copper tape coil, printed single and double conductive layer structures coils. The flexible printed coils are tested in both forms of flat and deformed at 16 m^{-1}. The impedance phase angles near the SRF are asymptotic due to the resonant effect, the SRF can be located for each coil from this figure.

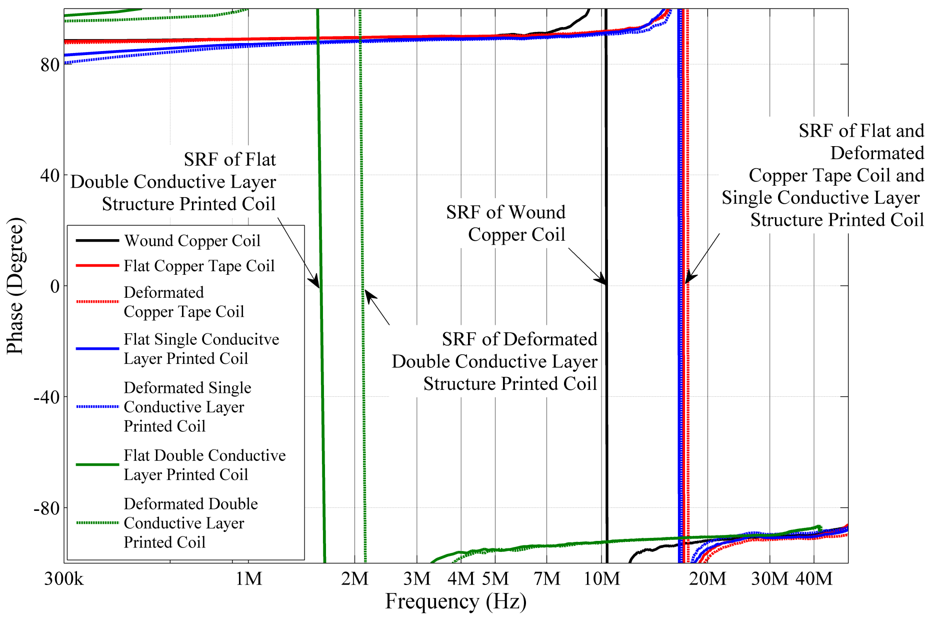

Figure 6-14 Impedance phase angle of different type of coils on frequency range from 300 kHz to 50 MHz

The SRF of all double conductive layer structure coils are between 1.5 MHz and 2.5 MHz, while all single conductive layer structure coils, wound copper coils and copper tape coils have their SRFs at approximately 17.6 MHz. The differences of SRF between the flat and deformed flexible printed coils are within 2%, which means the effect of deformation on the SRF of these coils is negligible. In the range of frequencies which tested different types of coils have positive input impedance phase angles, these coils are inductive and these frequencies can be used as operation frequency for WPT.

Table 6-8 shows the practical SRF and inductance of each coil, and the parasitic capacitance is calculated and compared with the theoretical values based on the model described in Section 4.3.2.

Table 6-8 Inductance, parasitic capacitance and self-resonant frequency of different types of coils

Coil Type	Structure of Conductive Layer(s)	Self-resonant Frequency (MHz)	Inductance (μH)	Theoretical Parasitic Capacitance (pF)	Calculated Parasitic Capacitance (from measurements) (pF)
Wound Copper	N/A	23.57 ± 1%	5.24 ± 1%	5	8 ± 0.5%
Copper Tape	Single	23.95 ± 3%	4.40 ± 2%	6	10 ± 1%
Printed Coil on Alumina	Single	17.15 ± 5%	6.54 ± 6%	20	13 ± 6%
	double	4.23 ± 8%	15.2 ± 9%	80	93 ± 5%
Printed Coil on Kapton	Single	16.12 ± 7%	3.83 ± 5%	20	25 ± 6%
	double	4.33 ± 10%	7.78 ± 9%	80	107 ± 10%
Printed Coil on Interface-coated Textile	Single	16.37 ± 8%	3.88 ± 8%	20	24 ± 9%

The inductances of coils with single and double conductive layer structures are within 15% of theoretical calculations for flat coils. The theoretical calculation of parasitic capacitance has a discrepancy of ± 30% from experimental values obtained based on SRF and inductance in the coils with single conductive layer structure. One reason that could cause the error is the varying relative permittivity of surrounding materials. The practical value of parasitic capacitance on the coil with double conductive layer structure is in all cases less than the theoretical calculation by 33%, it confirms that the design strategy of reducing the overlap area effectively limits the parasitic capacitance.

Coils with the double conductive layer structure have approximately four times the parasitic capacitance of equivalent coils with the single conductive layer structure, because the Fabinks-UV-IF1 ink used in the dielectric layer has a relative permittivity of approximately 41. These large parasitic capacitances on the coils with double conductive layer structure narrow the range of operating frequency of WPT systems utilising these coils. A larger parasitic capacitance has increased charging and discharging on it when current is oscillating in the tracks of the coil, this effect increases the AC resistance of such coil and reduces the efficiency of WPT system as mentioned in Chapter 4.

6.3.1.5 Unloaded Q Factor of Coils

The unloaded Q factor of inductors is a measure of the ratio of stored against lost energy in unit time, which allows evaluation of the quality of coils. The unloaded Q factor of coils in this experiment is calculated based on equation 4.21. For this calculation, the AC resistance, the inductance and the operating frequency are required. The measured and calculated unloaded Q factor of various coils at the 200 kHz operating frequency are shown in Table 6-9 and compared with the theoretical calculated value.

Table 6-9 Practical unloaded Q factor of coils comparing with the theoretical calculation at 200 kHz operating frequency

Coil Type	Structure of Conductive Layer(s)	Theoretical Unloaded Q	Measured Unloaded Q	Calculated Unloaded Q
Wound Copper	N/A	80	79	80
Copper Tape	Single	75	73	76
Printed Coil on Alumina	Single	20	18.4	18.7
	double	16	14.8	15.1
Printed Coil on Kapton	Single	20	18.2	18.5
	double	16	13.9	13.9
Printed Coil on Interface-coated Textile	Single	18	16.8	17.1

For each type of coil, the practical unloaded Q factor is within 13% of theoretical calculation, the relatively higher DC and AC resistance and lower inductance compared with theoretical values as shown in Figure 6-8, Table 6-6 and Table 6-8 respectively cause the reduction in the Q factor of the coils. Compared with wound copper coils and copper tape coils, the printed coils on all substrates with both single and double layer structures have a reduction of up to 75% in unloaded Q factor, which is mainly caused by the higher DC resistance of the printed conductive paste compared with copper. It can be seen that the coils with double conductive layer structure have a 24% reduction in unloaded Q factor compared to coils with single conductive layer structures, which shows that they are not suitable for WPT because of their high resistance, high capacitance, low self-resonant frequency and low unloaded Q factor. A practical test on transfer efficiency using coils with double conductive layer structure shows very low efficiency (<1%), so they will not be discussed further in later sections covering efficiency measurements.

6.3.2 Flexibility of Coils

As discussed in Session 6.3.1.1, a low DC resistance has been achieved by increasing the thickness of the conductive layer, this thick conductive layer reduces the flexibility of the coil. The flexibility of coils with an optimal number of conductive sub-layers is discussed here in terms of the compromise between the requirement for low DC resistance and the requirement for high flexibility. Printed coils on Kapton and on interface-coated textile can be bent to the same curvature when they attached on the same support, there is no damage occurred on all coil samples after bending round a mandrel with a radius of 150 mm (a curvature of 16 m^{-1}). It should also be noted that the DC resistance changes after the coil is bent, the DC resistance of the track is measured before and after bending to demonstrate the functionality of the coils after deformation, hence to confirm the functional flexibility of printed coils. The DC resistances (R_{DC}) of the flexible coils are measured after they are cured and then these printed coils peeled and removed from the alumina support tile used to support the flexible substrate during the fabrication process. Finally, the R_{DC} is measured again. The DC resistances of coils before and after peeling are listed in Table 6-10.

Table 6-10 DC resistance of flexible coils before and after peeling

Coil Type	Structure of Conductive Layer(s)	R_{DC} before peeling (Ω)	R_{DC} after peeling (Ω)
Printed Coil on Kapton	Single	20.0 ± 5%	26.8 ± 5%
	double	40.8 ± 15%	46.4 ± 15%
Printed Coil on Interface-coated Textile	Single	20.6 ± 10%	21.3 ± 10%

The DC resistances on both substrates increased by approximately 10% after peeling, this result shows the behaviour of increase on the resistance. This is because the length of conductive track has been changed when the substrate being deformed, and the DC resistance is relative with the length when the volume of the conductor is given. This test shows the flexibility of the cured conductive layer, as the volume of silver in the conductive track does not change, the silver particles return to approximately their initial positions after the coil with the substrate is peeled from the alumina support tile, and less plastic deformation is occurred, the change in DC resistance is low (10% increase) and the flexibility of printed coil has been verified.

In conclusion, the coils printed on both Kapton and interface-coated textile substrates with different structures are flexible as expected for a wearable WPT system as discussed in Chapter 2 and 5. The flexible coils were printed on Kapton successfully, the fabrication processes to print coils on flexible substrate has been verified, and it provides a reference to fabricate the flexible coils on interface-coated textile. The comparable results of electrical characteristics between flexible coils printed on Kapton and interface-coated textile show that the fabrication processes are repeatable for the coil with single conductive layer structure. Since Kapton cannot be stretched but the interface-coated textile can, the issues of shrinkage and plastic deformation, which cause the double conductive layer structure coil cannot be printed on interface-coated textile satisfactorily, cannot be addressed by printing coils on Kapton. The Kapton does not have any breathability as a substrate as discussed in Chapter 5, which is an uncomfortable factor when employing a coil printed on Kapton in wearable applications, thus the printed coil on Kapton is not considered as a suitable solution for flexible printed coil for WPT in AAL system, and not going to be discussed in following wireless power transfer experiment.

6.4 Wireless Power Transfer via Flexible Coils

The coils are paired as TX and RX coils in the WPT system, in this section, two different types of flexible coil are paired as three groups; two copper tape coils, two printed single conductive layer structure circular coils on interface-coated textile, and one copper tape coil with one printed coil. When the system is operating these paired coils are coupled as a link which can transfer power wirelessly. The coupling factor of each pair of coupled coils is examined for varying misalignment of centre offset and separation distance between two coupled coils, and with different curvature of deformation of flexible coils. For the wearable WPT system of AAL applications, TX and RX coils are typically kept in parallel or a limited misalignment angle within relatively small separation distance compared with the dimension of printed coil, consiquently, the effect of limited angular mislaignment between coils is negligible in the context of the application disscused in this thesis. The flexible coils connected to resonant tank capacitors to tune them to suit the driving and receiving circuits, to avoid losing energy between source (driver circuit or receiver coil) and load (transmitter coil or receiver circuit). The resonant tank capacitors are calculated and deployed with coils in pair as discussed in Section

5.5, the loaded Q factor of circuits is therefore calculated once the coils have been tuned with circuits which have determinate resonant tank capacitors. On the other hand, the coils with double conductive layer structure are unsuitable to be deployed in a wearable WPT system as discussed earlier, and the coils printed on Kapton do not have any breathability, which is also unsuitable for a wearable applications as discussed earlier, consequently, these coils are not going to be involved in following sections.

The bqTESLA is a commercially available Qi standard WPT system from TI, it includes the driver, bq500211EVM, and the receiver bq51013AEVM. In the bqTESLA system, both receiver and transmitter ICs for wireless power transfer are integrated individually, the evaluation modules have abundant testing ports to monitor the system operation, i.e. input and output power. The transmitter driver has digital demodulation signal processing to keep the system components in a low amount, hence to reduce the power consumption of the driver. In this thesis, this system equipped with different types of paired coils to evaluate the performance of different types of coil deployed in WPT system and measure the DC to DC efficiency of such transfer. The driver bq500211EVM is constructed with a class-D amplifier to invert DC power source to 200 kHz AC power. Power is transferred wirelessly via the resonant inductive link through the coupled coils, and then received by the full-bridge synchronous rectification circuit that is integrated in the bq51013AEVM receiver module.

In the bqTESLA wireless power transfer system, a pair of wound copper coils are provided in the original system along with a ferrite shield which is non-flexible, all wound copper coils and resonant tank capacitors for these coils are tuned by the manufacturer following the Qi standard to achieve optimum performance at 2.5 W output power with wireless power transfer of 52% DC to DC efficiency under full load within a 5 mm transfer distance [186, 187]. The resonant tank capacitors has been selected with high Q factor value of over 1000 at 1 MHz to provide the critical resonant circuit. In this experiment, these original coils are replaced by different combinations of copper tape and printed coils, the input voltage, input current, output voltage, and output current of the WPT system are measured to calculate efficiency as the ratio of the output power to the input power. By adding the bidirectional current shunt monitor chip AD8210 into the system, between the driving circuit and transmitting coil as well as between the receiving coil and receiving circuit, the power consumptions in WPT system are measured to examine the printed coils in circuit.

Measurements of wireless power transfer in this section are performed on a plastic support as shown in Figure 6-15. The measurements of coupling factors of different combinations of selected flexible coils and output powers of the WPT systems employing such coils require a stable support to keep tested coils in desired positions due to the results of these measurements are strongly affected by the relative position between tested coils. A rail track is used as base to keep the support attached on it centre aligned and can be moved in one direction. A pair of 0.5 mm thick plastic spring pads is positioned in slots on the support, the curvature of these pads can be adjusted individually by varying the height of support which will be discussed later. The flexible coils are attached onto these pads, then the coils are mounted in a fixed position in form of plane or certain curvature. The position each coil located on the pad is marked with 5 mm grids, since the two pads are centre aligned by the rail track, the offset of each coil on these grids indicates the centre offset between the coils. The separation distance between the tested coils, the curvature of deformation of them, and the centre offset between them can therefore be adjusted on the designed plastic support. Non-metal supports are employed to limit the effect of these accessories on electromagnetic field which WPT relies on. Although these measurements can be performed by hand, a stable support is preferable to reduce the time spending on alignments and adjustments, and improve the repeatability of these measurements.

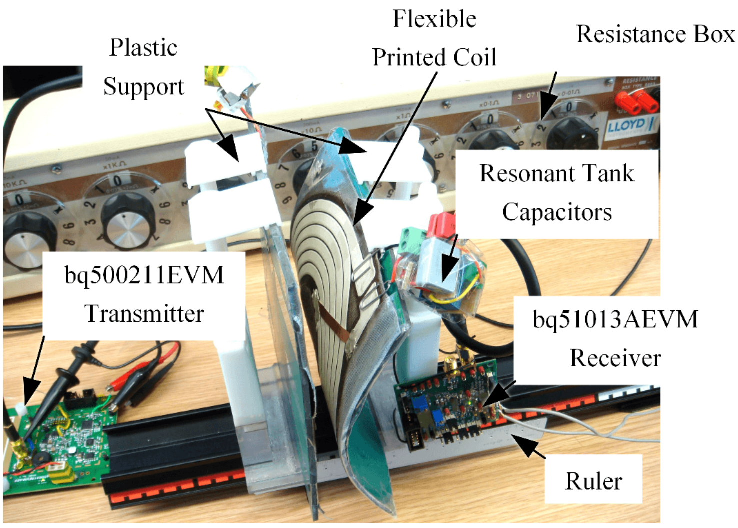

Figure 6-15 The experimental setup for performance testing of flexible coils deployed in Qi-standard Wireless Power Transfer system with mandrel radius adjustable plastic support

The centre offset between two flat circular spiral coils is not depended upon the direction of this offset, therefore a centre offset in one direction can be used to represent the factor of offsets in other directions. The separation distance between TX and RX coils is measured by a ruler, which is attached on the bottom of support and has graduations of 0.5 mm, this ruler allows a fine adjustment of separation distance. Thus the effect of varying the separation distance on the maximum output DC power and DC to DC efficiency of WTP are examined.

To set the curvature of deformation of coils, one assumption is applied: The bent spring plate that the flex coil attached is in constant curvature like a circle. Hence the curvature of the coil

κ_{coil} can be adjusted by varying the vertical height h as $\kappa_{coil} = \frac{1}{r} = \frac{8d_s}{(4{d_s}^2+h^2)}$, which is shown in Figure 6-16, where d_s is the arc depth. The arc depth and vertical height can be measured by a ruler, the arc depth is increased when the vertical height is decreased as the length of arc, which is the length of the spring pad, is constant at 150 mm. On the plastic stand, the thick plastic spring pad is locked by two slots on both top and bottom. The position of the slot is adjusted by two nuts on a bolt. The height h of the plastic stand therefore is changed by varying the positon of the top slot, thus the plastic spring pad and the flexible coil attached to it are squeezed to the desired curvature.

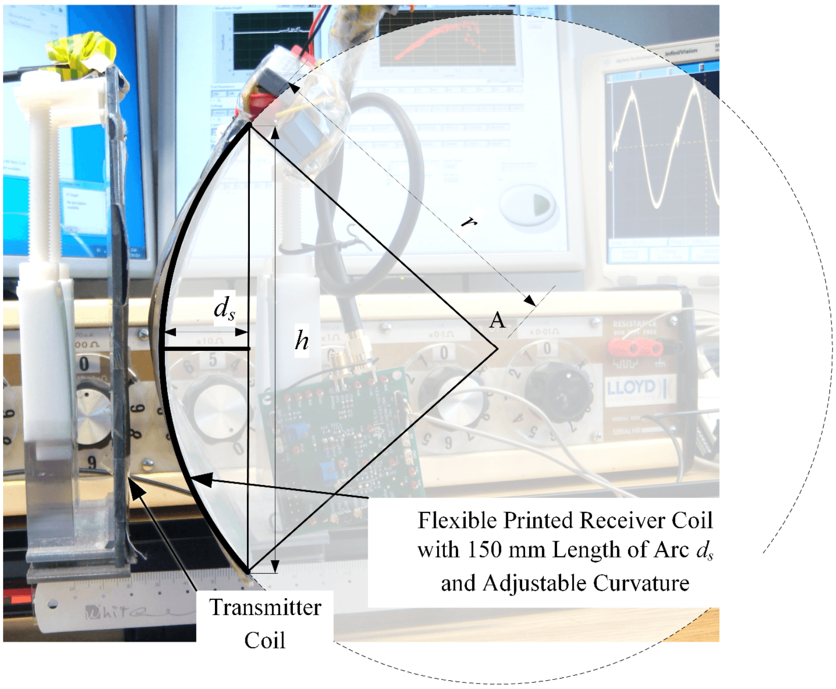

Figure 6-16 The curvature of flexible coil as adjusted by the height of plastic stand at certain radius

6.4.1 Coupling Factor

The coupling factor k expresses the coupling between TX and RX coils. The better coupling the WPT system has a larger proportion of the power transmitted from TX that the RX coil receives. The efficiency of power transfer between the TX and RX coils is therefore indicated mainly by the coupling factor. The coupling factor of a pair of coils is measured using the following procedure:

1. Mount the paired coils on the plastic stands with resonant tank capacitors, adjust the position of coils to make them centre aligned.
2. Connect the TX coil to a 200 kHz sinusoidal voltage source, the peak to peak voltage of this source is recorded as V_{TA}, and then measure and record the induced peak to peak voltage of the RX coil, V_{RA}, by using an oscilloscope.

3. Change the same 200 kHz voltage source to drive the RX coil with a peak to peak voltage recorded as V_{RB}, and then measure and record the induced peak to peak voltage, V_{TB}, cross the TX coil.
4. Calculate the coupling factor based on the equation 4.24. For the identical TX and RX coils without deformations, this equation can be simplified as $k = \frac{V_R}{V_T}$. For the TX and RX coils with any deformation, the coupling between them is required to calculate as the system with two different coils for TX and RX circuit.
5. Adjust the centre offset between the TX and RX coils, and then repeat steps 2 to 4, record the coupling factors at different centre offset distance. Plot the coupling factors versus the centre offset.
6. Adjust the distance between the TX and RX coils, and then repeat steps 2 to 4. Plot the coupling factors versus the separation distance.
7. Adjust the curvatures of flexible coils, and then repeat steps 2 to 4 at 5, 10, 15, and 20 mm separation distance. Plot the coupling factors versus the curvatures.

The peak to peak voltages are measured using an oscilloscope with x10 probes. Each probe has 10 MΩ input impedance [188], which is much larger than the typical leakage impedance of a planar air-core printed coil (< 20 Ω at 200 kHz [189]), the capacitances of voltage source, cables and measured coils can therefore be neglected at resonance peaks.

The coupling factors of paired coils against centre offset distance at 10 mm separation distance for the three combinations of copper tape coils, a copper tape coil with printed coil, and printed coils are shown in Figure 6-17.

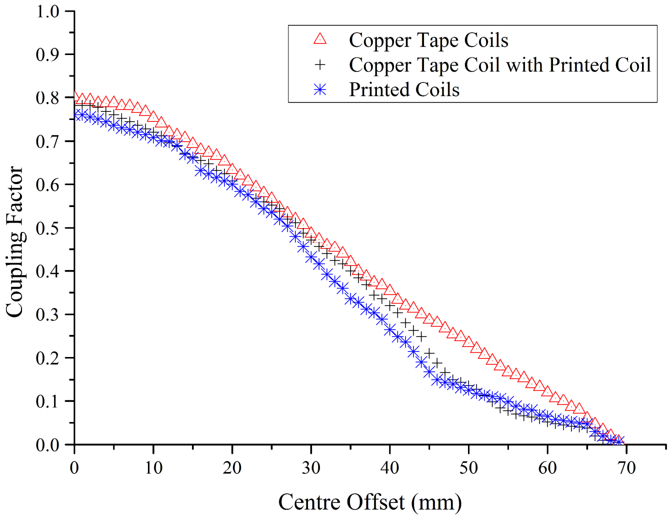

Figure 6-17 Coupling factor *k* against centre offset

The results show that the coupling factors drop down to zero when the centre offset is equal to the radius of coils, where the directions of magnetic fluxes of two coils are opposite at this position as expected. The coupling factors of the three combinations of paired coils against centre separation distance are shown in Figure 6-18 compared with the theoretical values calculated using equation 4.23.

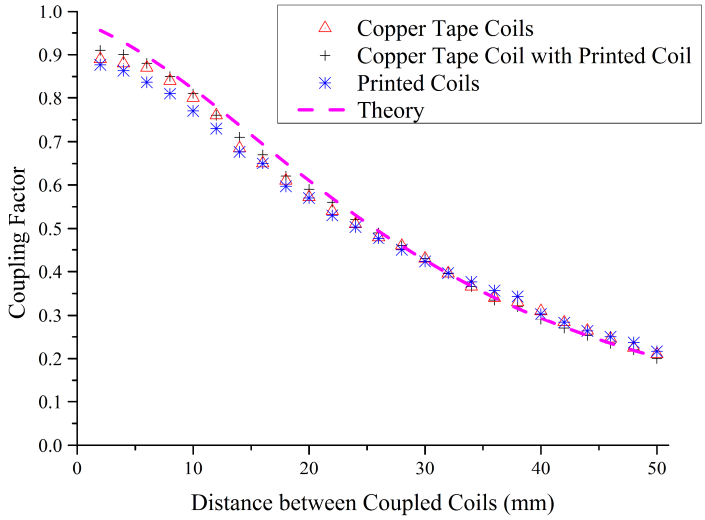

Figure 6-18 Coupling factors *k* of different combinations of paired coils against centre separation distance compared with the theoretical calculations

The general shape of coupling factors for the coils tested follow the theoretical calculation, although the coupling factor limits to a value of approximately 0.9 where the separation distance is less than 6 mm. The practical coupling factors of all pared coils have errors within 10% for 10 to 50 mm separation distances. Both centre offset and separation distance in the range from 0 to 50 has approximately 75% drop down on the coupling factor, the effect of centre offset on the couple factor is can be said to be equivalent to increasing the separation distance between coupled coils in the range between 0 to 50 mm. The effect of varying the centre offset between the printed flexible coils on the output power and efficiency of the WPT system will not going to be discussed in following sections to avoid repeating same result on the testing for the effect of varying the separation distance between the coils.

The coupling factors of the three combinations of paired coils against different curvatures are shown in Figure 6-19 to 6-22 for separation distances of 5, 10, 15 and 20 mm, respectively.

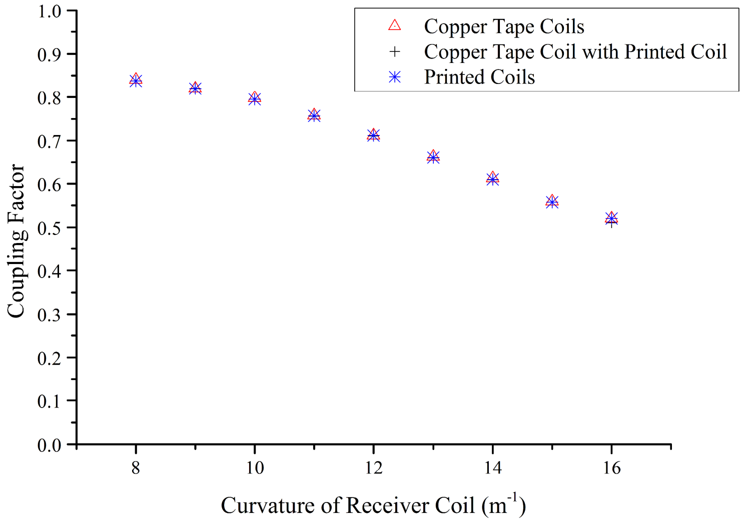

Figure 6-19 Coupling factor *k* against different rate of curvatures at 5 mm separation distance

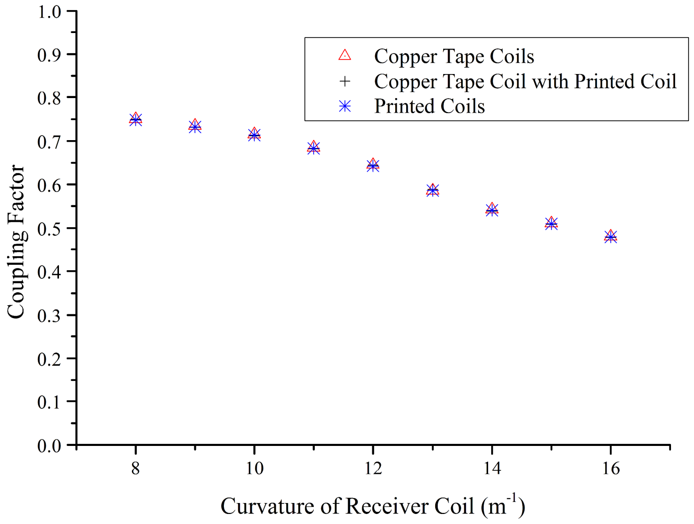

Figure 6-20 Coupling factor *k* against different rate of curvatures at 10 mm separation distance

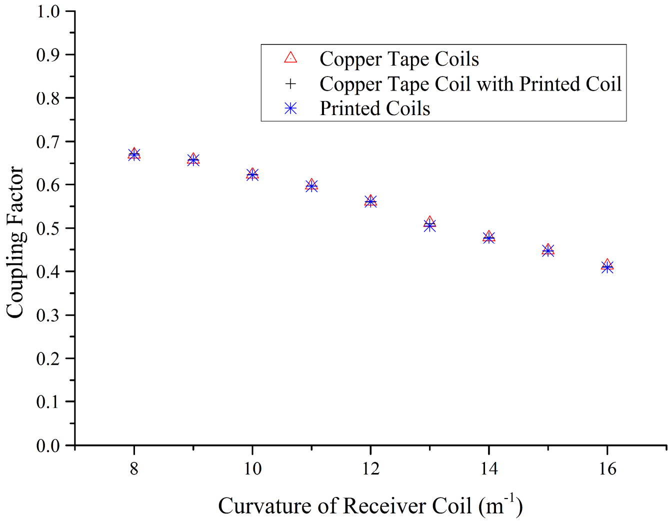

Figure 6-21 Coupling factor *k* against different rate of curvatures at 15 mm separation distance

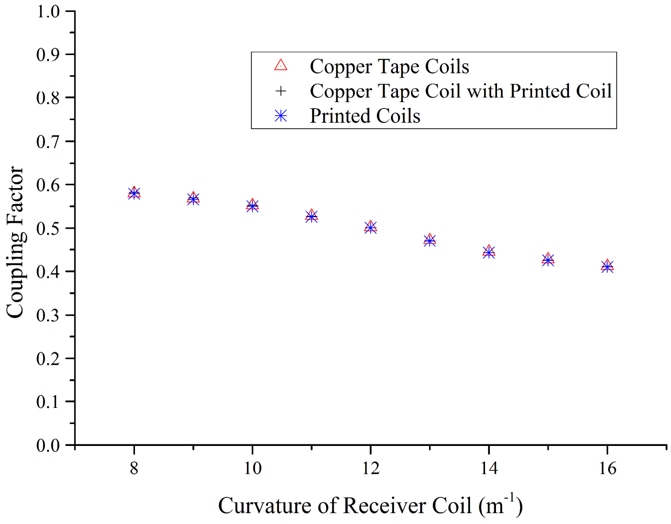

Figure 6-22 Coupling factor *k* against different rate of curvatures at 20 mm separation distance

The results show that the effect of deformations on coupling factors is irrelevant with respect to the combinations of different coil types. Since the coupling factor reflect the mutual inductance of TX and RX coils, it is independent with the material the coil made from as confirmed from these figures, that the mutual inductance is depend on the diameters of TX and RX coils and separated distance between them in the context of this application. The deformations have reductions on the coupling factors of 33%, 27%, 26%, and 17% at separation distance of 5, 10, 15 and 20 mm, for an increase in curvature from 8 to 16 m^{-1}.

6.4.2 Loaded Q Factor

Resonant tank capacitors are required to tune the TX and RX coils, they are formed as two capacitors connected with one in parallel and the other in serial as shown in Figure 5-10, the loaded Q factor of circuit can be calculated after these capacitors been determinate. The values of resonant tank capacitors depend on the characteristics of the coil they attached to and are calculated as described in Section 5.5 with an additional parameter of 58 Ω output impedance from the Qi standard driver bq500211EVM , which has a 20V AC driving peak-peak voltage with maximum 0.25 A of output current. The loaded Q factor of the circuit is limited by the unloaded Q factor of the coils and their resonant tank capacitors, it can be calculated using equation 5.1. The flexible coils are tuned at 195 kHz to co-operate with Qi standard driver and receiver, Table 6-11 shows the values of resonant tank capacitors and the loaded Q factors of different type of coils compared with the original wound copper coil on the evaluation board. The given standard deviation is calculated based on values for 8 samples of each type of coil.

Table 6-11 Loaded Q factor of circuit with different coils

Coil Type	Parallel Capacitor (nF)	Serial Capacitor (nF)	Loaded Q
Wound Copper	2	183	52
Copper Tape	3 ± 5%	220 ± 5%	52 ± 5%
Printed Coil on Interface-coated Textile	8 ± 2%	320 ± 3%	39 ± 5%

The loaded Q factors of the circuit equipped with printed flexible coils has approximately a 20% drop compared with the circuit when equipped with wound copper or copper tape coils, it is because that the unloaded Q factor of printed flexible coils is smaller than other coils (55%). These different types of flexible coils are tuned at same operating frequency, each turned coil can be coupled with the same type or any other type of coil when applying 195 kHz alternating current supplied by driver circuit, the three combinations specified in Section 6.4.1 can therefore be deployed in a WPT system without further adjustment.

6.4.3 Output Power and DC to DC Efficiency

The different combinations of paired coils with their resonant tank capacitors are connected to the Qi standard commercial driver and receiver modules to transfer the power wirelessly, the output power and DC to DC efficiency of the WPT system are measured at varying separation distance between coupled coils and deformed curvature on flexible coil, as results, the performance of these coils can be evaluated. The output DC powers of WPT systems with different combinations of paired coils are loaded using a resistance box to enable the adjustment of the load currents, and result the changing of input powers. The input and output DC power of the WPT system are measured, and the DC to DC efficiency can therefore be calculated. The output powers and DC to DC efficiencies of the WPT system with the three different combinations of coupled coils are measured at 5, 10, 15, and 20 mm separation distance between the TX and RX coils using the following procedure:

1. Mount the paired coils and WPT system on the plastic stands, adjust the position of coils to make them centre aligned.
2. Power the bq500211EVM driver using an Aim-TTi digital Power Supply Unit QL355TP, read both input voltage, V_{In}, and input current, I_{In}, from this power supply. Calculate the input DC power as $P_{Input} = V_{In} \times I_{In}$.
3. Vary the load on the output of the receiver circuit and record the input DC power, P_{Input}, for the driver circuit, and measure and record the output voltage, V_{Load}, from the receiver circuit by using a 12-bit A/D convertor (NI USB-6008) and the resistance of the load, R_{Load}. Calculate the output current as $I_{Load} = V_{Load}/R_{Load}$, and the output DC power as $P_{Load} = V_{Load} \times I_{Load}$.
4. Plot the output power of the receiver circuit versus its output current, and locate the maximum output power point.
5. Calculate the as $\eta_{DC-DC} = P_{Load}/P_{In}$.
6. Plot the DC to DC efficiency of the WPT system versus its output current, and locate the maximum efficiency point.
7. Adjust the separation distance between the TX and RX coils, and then repeat steps 2 to 6, then plot the maximum DC to DC efficiency versus the separation distance.

Figures 6-23 to 6-26 show the output power against the output current from the wireless power transfer system employing different coupled coils.

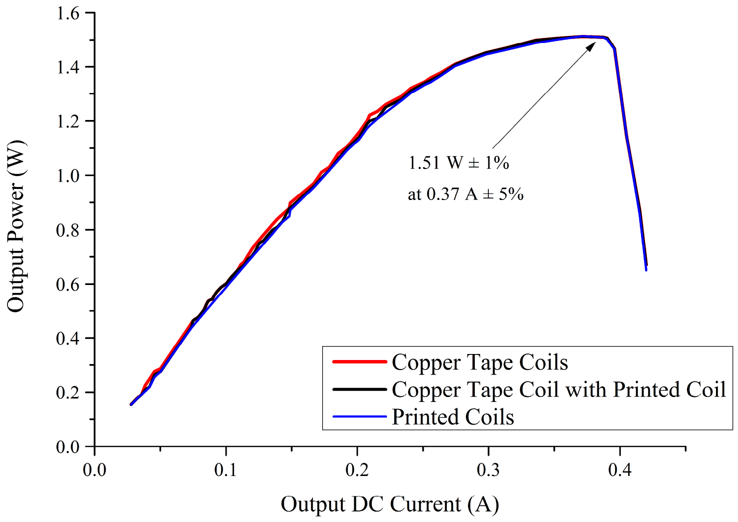

Figure 6-23 Output power of WPT system with different types of coupled flexible coils at 5 mm separation distances

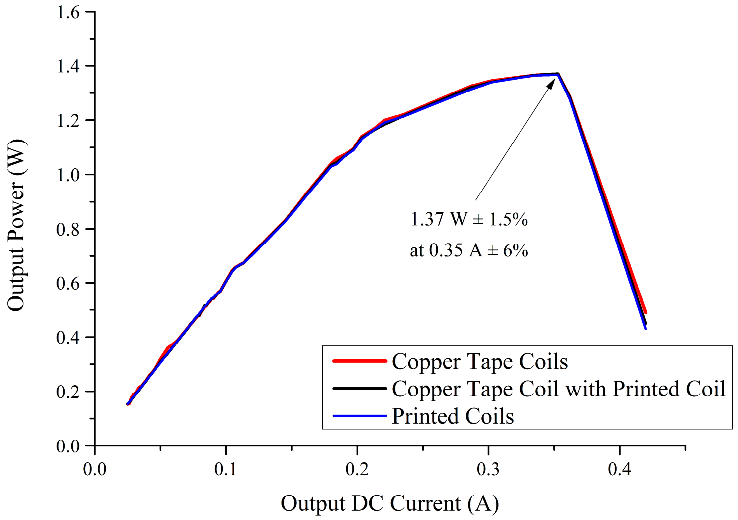

Figure 6-24 Output power of WPT system with different types of coupled flexible coils at 10 mm separation distances

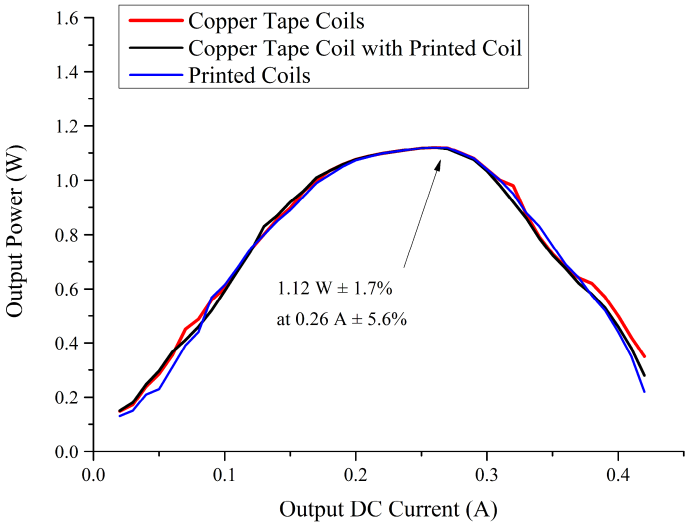

Figure 6-25 Output power of WPT system with different types of coupled flexible coils at 15 mm separation distances

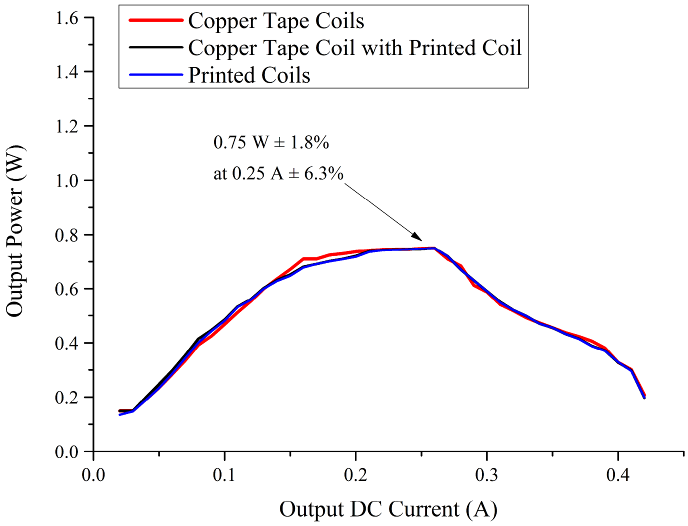

Figure 6-26 Output power of WPT system with different types of coupled flexible coils at 20 mm separation distances

As highlighted in these four figures, the maximum output power points can be located by reading the maximum values on *P*/*I* curves. The given standard deviation of maximum output power is calculated based on 10 times of measurements with two pairs of each combination of coupled coils. The sharp drops on output powers are occurred in the Figures 6-23 and 6-24, they are caused by the protection on the limited maximum load in the TI wireless power receiver solution.

The maximum output power of the WPT system using a pair of printed coils is 1.51 W at 5 mm separation distance, which gives an output voltage of 4.08 V. The maximum output power is reduced to 0.75 W as the separation distance between coupled coils increasing from 5 mm to 20 mm. For all the coils tested, the errors of maximum output power are 1%, 1.5%, 1.7%, and 1.8% at 5, 10, 15, and 20 mm separation, respectively. The power has been transferred wirelessly by different combinations of coupled coils and printed flexible coils, which achieve a maximum of 60% of the 2.5 W power that the same system can deliver using the original, commercial, coils.

Figures 6-27 to 6-30 show the DC to DC efficiency of the WPT system against the output current from the wireless power transfer system employing different coupled coils.

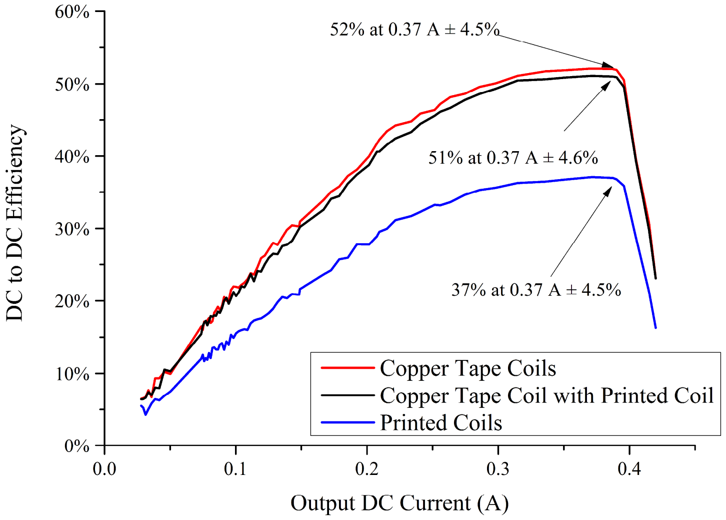

Figure 6-27 DC to DC efficiency of WPT system with different types of coupled flexible coils at 5 mm separation distances

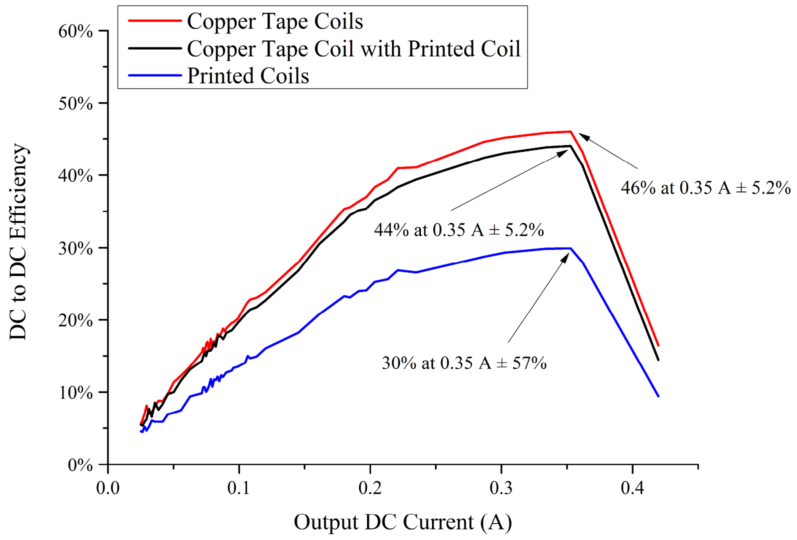

Figure 6-28 DC to DC efficiency of WPT system with different types of coupled flexible coils at 10 mm separation distances

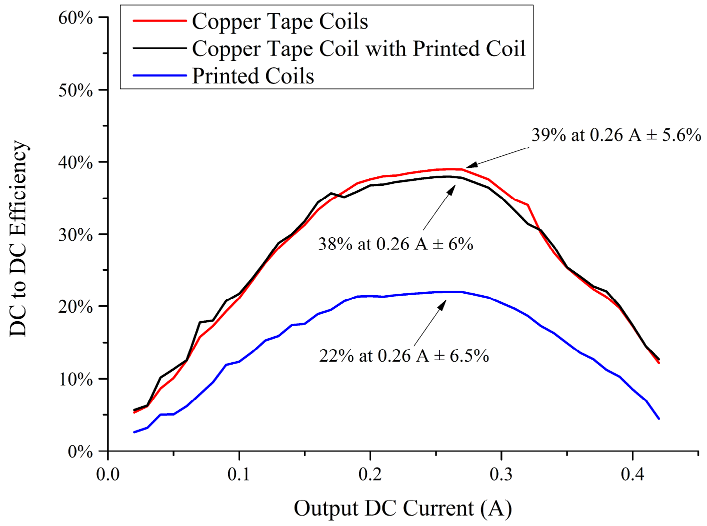

Figure 6-29 DC to DC efficiency of WPT system with different types of coupled flexible coils at 15 mm separation distances

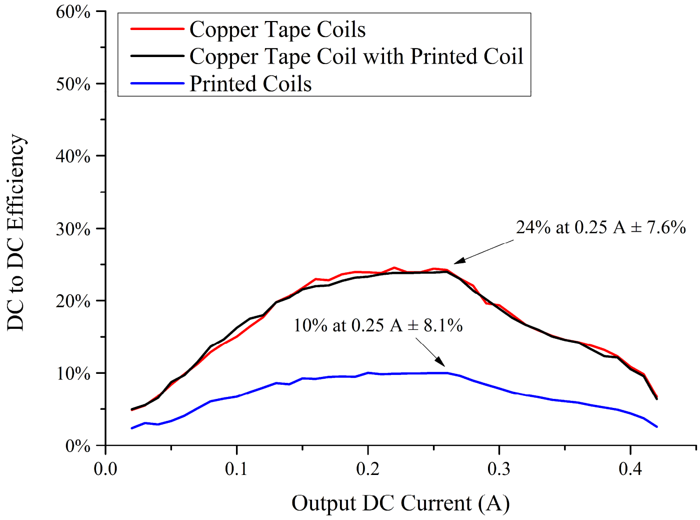

Figure 6-30 DC to DC efficiency of WPT system with different types of coupled flexible coils at 20 mm separation distances

As highlighted in above figures, the maximum DC to DC efficiency points can be found by reading the maximum values on η/I curves. The given standard deviation of maximum output power is calculated based on 10 times of measurements with two pairs of each combination of coupled coils.

More maximum output powers have been addressed by repeat the testing in different separation distances, the results show that the effect of different combinations on output power is ignorable, the maximum output powers of the WPT system employing with all tested coils combinations against centre separate distance is shown in Figure 6-31. The standard deviation is calculated based on 10 measurements with each combination.

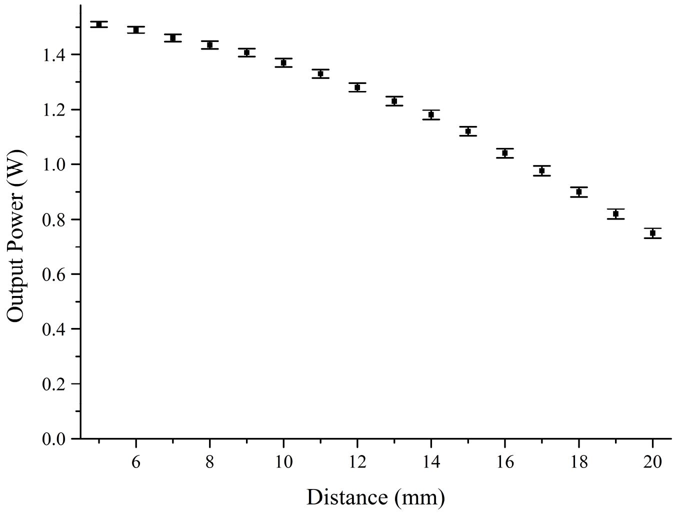

Figure 6-31 Maximum output power of WPT system employing different types of flexible coils against centre separation distance

By comparing the load currents when the maximum DC output power and DC to DC efficiencies are achieved, the highest efficiencies all occur at the maximum output power point. The Qi WPT system is designed to achieve optimal efficiency at full load, using the turned printed flexible coils, the WPT system continuous to achieve its optimal efficiency at system maximum output power point (1.51 W).

Figure 6-32 shows the maximum DC to DC efficiency against different separation distance between different types of coupled coils, the standard deviation is calculated based 10 times of each measurement.

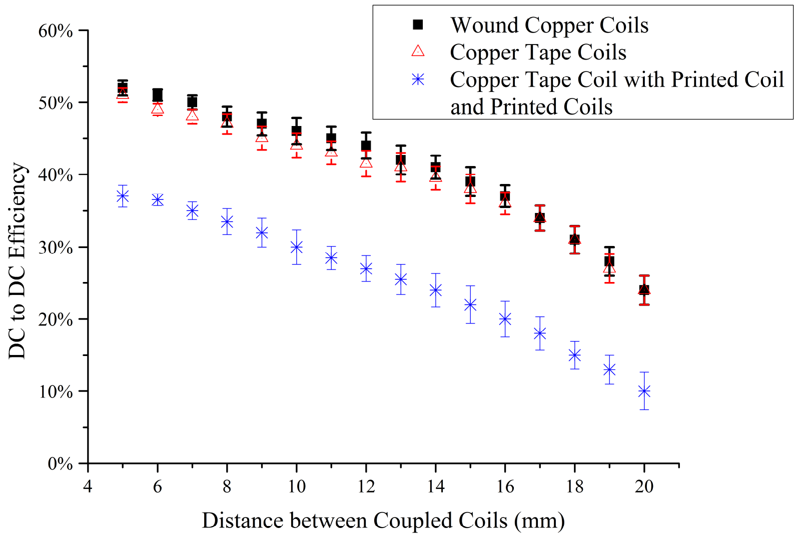

Figure 6-32 Maximum DC to DC efficiency of WPT system employing printed flexible coils against centre separation distance

The maximum DC to DC efficiency is 38% when the WPT system is equipped with one copper tape coil and one printed coil with 5 mm centre separation. This efficiency is approximately 73% of that obtained without any printed coils at the same centre separation distance, which shows the additional power consumption due to the use of the printed flexible coils. There is a 20% decrease in DC to DC efficiency in all combinations of coils when the centre separation distance increases from 5 to 20 mm.

6.4.4 Effect of Deformation of Flexible Coils

Measurements on a pair of centre aligned printed coils with varying curvature of the RX coil are used to simulate the scenario of deformations of a wearable device during its operation period. Adjusting the curvature of the RX coil while keeping the TX coil flat represents a system which has a relatively rigid transmitter and a deformed receiver caused by it conforming to the human body. The effect of deformation on output powers and DC to DC efficiencies of WPT with coupled printed flexible coils are measured at 5, 10, 15, and 20 mm separation distance between TX and RX coils as following procedure:

1. Mount the paired coils with WPT system on the plastic stands, adjust the position of coils to make them centre aligned.
2. Vary the height of stand for RX coil, check the arc depth to give the flexible coil the desired curvature.
3. Repeat the steps 2 to 6 of the experiment described in Section 6.4.3, plot and locate the maximum DC output power and maximum DC to DC efficiency versus the deformation of flexible coil.

The maximum output power and DC to DC efficiency against the deformation curvature of the RX coil are shown in Figure 6-33, the centre separation distance between the coupled coils is 5 mm and the standard deviation is calculated based on 10 measurements.

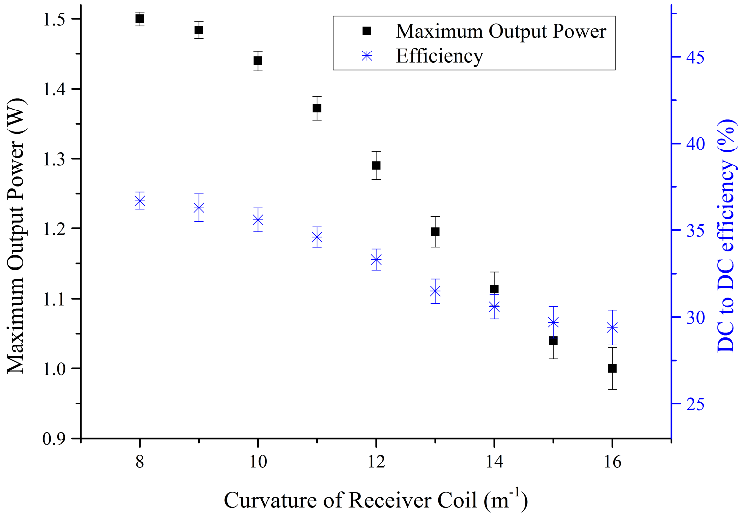

Figure 6-33 The maximum output power and DC to DC efficiency of WPT system employing printed flexible coils against deformation curvature on RX coil

Deforming the coil from a curvature of 8 to 16 m^{-1} causes a 33% reduction in maximum output power and a 20% reduction in the efficiency, this range of curvature includes the size of legs of 90.1% people in UK [190]. When the coils are deployed on the back of people, the curvature of deformation is smaller than when they are deployed on the legs, so the effect of the deformation is negligible. The other parts of the human body with greater curvature like the arms normally are being moved frequently, making them unsuitable locations to deploy the RX coils as frequently movements cause disconnections between the RX and TX coils when they are out of the range of transfer distance, so the effects of deformation curvature greater than 16 m^{-1} are not going to be discussed in this work.

When increasing the separation distance between the TX and deformed RX coils, the DC to DC efficiency reduces as shown in Figure 6-34.

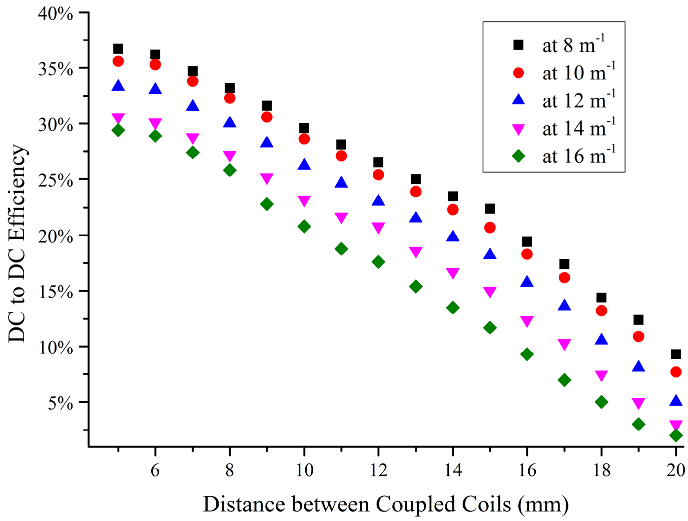

Figure 6-34 DC to DC efficiency of the WPT system with a deformed receiver coil under different curvature against the separation distance from the flat transmitter coil

It shows that the separation distance of centre aligned printed coil pairs is a major influencing factor for the DC to DC efficiency of WPT systems utilising flexible coils. In an application of a device worn on the body the separation distance between the TX and RX coils will typically be in the range between 0 to 20 mm, however the range of anticipated deformation of the coil is in the range 0 to 16 m^{-1}. Using these range values and the data presented in Figure 6-32 and Figure 6-34 the separation distance can be seen to cause the DC to DC efficiency to drop by 27.7% when the curvature is kept constant, whereas varying the curvature from 0 to 16 m-1 whilst keeping the separation distance constant only causes the DC to DC efficiency to fall by 8.8%.

6.4.5 Power Consumption

The DC to AC driver (TX) circuit, coupled printed flexible coils, and AC to DC receiver (RX) circuit consume power and limit the efficiency of the WPT system. An AD8210 bidirectional current shunt monitor chip was used to measure the current in each block, with the voltage across the block measured with an oscilloscope, these values were then used to calculate the power consumed in each block. Table 6-12 shows the percentage power consumption of each block of the WPT system when equipped with different combinations of coupled coils.

Table 6-12 Power consumption of WPT system employing different types of coupled coils

	TX Circuit	Coils	RX Circuit	Load
Wound Copper Coils	21.5%	8.7%	17.5%	52.3%
Copper Tape Coils	20.3%	9.8%	18.1%	51.8%
Copper Tape Coil with Printed Coil	20.8%	22.5%	17.9%	38.8%
Printed Coils	18.2%	26.1%	17.3%	38.4%

The results show that the printed flexible coils fabricated in this work consume up to 3 times of power than the original wound copper coils in the WPT system.

6.5 Conclusions

Experimental results from the screen printed fabrication process, the mechanical durability and electrical characteristics of the screen printed coil have been described in this chapter. Coils have been printed on different substrates of alumina, Kapton and interface-coated textile. A suitable curing temperature and duration for conductive layer of printed coils has been selected and examined based on the resulting DC resistance of the coils. A constant track width single conductive layer circular coil and a variable track width double conductive layer square coil have been fabricated using screen printing on an interface-coated flexible textile. The experimental results from the tests of the flexibility and electrical characteristics of the screen printed coil have been described and show that the flexible thick-film coils printed on 65/35 polyester/cotton textile achieve the desired flexibility. This has been achieved by using an interface layer (Fabink-UV-IF1) being used to facilitate the successful printing of the conductive paste with the desired geometry and resolution and to prevent the spreading and permeation of the conductive paste into the textile. The fabrication process has been verified as functional coils have been printed on all selected substrates.

The electrical characteristics of printed coils have been measured, and the results have been compared with theoretical calculations which show expected values of the resistance, inductance and parasitic capacitance of the coils and found to be in agreement within a reasonable range. The double conductive layer structure coil is not considered to be deployed in the WPT system in this work due to its poor performance in both electrical characteristics and flexibility.

Experiments on the coupling factors of paired coils and the loaded Q factor of TX and RX circuits employing different combinations of coils have been discussed. The output power and DC to DC efficiency has been measured on a WPT system equipped with different combinations of coils, the results from these tests show that the printed coils can deliver 1.51 W power for active sensors and networks of an AAL system. The analysis of the deformation of printed flexible coils during the WPT operation period shows the functionality of flexible coils in system, which meets the target of the fabrication of wearable printed coils for WPT systems in this thesis. Finally, the limitations of printed coils have been examined regarding their higher power consumption than wound copper coils.

The recommended design for producing flexible coils on textiles is the circular coil with constant width track single conductive layer structure, Frabink-UV-IF1 produce a smooth surface between textile and printed layer, and a high conductive flexible paste is desired to achieve a low resistance of the printed coil and remains its flexibility.

The resistance and parasitic capacitance of the printed coils lead to increased losses in the coils when compared to wound copper coils resulting in the loss of energy in the inductive coupling process, and therefore reducing the overall efficiency of the WPT system. The printed coil remains room temperature during the entire testing, including that some experiments take 3 hours running with different loads to check the stability of the system. The general performance of the system employed with printed coils is comparable with the system employed with wound coils. A comparison of the DC to DC transfer efficiency of the WPT system with different types of coils has shown the DC to DC efficiency of the printed coils to be limited to 30%, compared to a 52% efficiency recorded for the wound copper coils. The separation distance of two coils was found to be the major influencing factor on the DC to DC efficiency compared with the effect of deformation of the flexible coils from a planar form.

7 Conclusions and Future Work

This chapter concludes this thesis by summarising the work carried out, discussing the significance of wireless power supply methods, which are solar energy harvesting and Wireless Power Transfer (WPT) for the Ambient Assisted Living (AAL) system, and recommending directions for future research in this area.

The literature review has described the functionality of the AAL system, which delivers a comprehensive healthcare solution with sensors and networks both in building environments and on body area. The different power supply methods for passive and active sensors with their networks have been reviewed, the advantages and disadvantages of mains wiring, batteries, energy harvesting, and WPT have been discussed. For passive sensors, energy harvesting technology with efficient extraction circuitry has strong performance in reviewed researches and applications, it has been considered as power supply method for the passive sensors deployed in applications for AAL system in Building environment in this thesis. The light source, as a primary energy harvesting power source in buildings, have not been previously investigated by considering changing of type of lighting system and optimising solar cell materials.

For active sensors, on-body area applications of the AAL system have the limitation of user experience with their power supply due to the presence of cables and batteries, which are necessary to provide the sufficient power. The capability of inductive WPT to supply sufficient power for active sensors and networks on body area has been reviewed, which also shows that the rigid coils in the WPT system causes discomfort to users. The screen printing technique has been reviewed and it can be used to produce flexible and functional coils. The screen printing technique has been selected to fabric flexible coils for wearable WPT system to supply the power for high power consuming on-body area applications in AAL system.

A solar powered PIR sensor demonstrator has been designed, built and tested. This can provide occupancy information for the human tracking component of an AAL system. Solar cells are selected as the power supply, the selected model should harvest sufficient energy to operate robustly when deployed in a system, irrespective of the type of light source providing the illumination. A change in the type of illumination sources used causes a change in the radiant spectra of the ambient light, a solar cell can harvest more power when its spectral sensitivity, which is defined by its active materials, fits the radiant spectra of ambient light sources. The investigation shows effects of changing different light sources on selected types of solar cells, and demonstrates that a solar cell is a suitable power source for the PIR sensor. The effect of the type of illumination on the energy harvesting performance of solar cells has been investigated and published in Solar Energy journal. The blocks of this wireless PIR sensor have been examined and built. Furthermore, the demonstrator PIR sensor has been tested in a typical office room in a building environment to demonstrate its capability for detecting occupancy without ambient energy input for up to 16 hours after nine hours charging, which is longer than the commercially available devices.

WPT has been investigated as the power supply method for power consuming active sensors and networks on body area. The theory of WPT has been studied, beginning with the coupled system, then the mathematical model of printed flat air-core coils, and finally the TX and RX coils with compensation circuitry. The inductance, parasitic capacitance, resistance and unloaded Q factor as the key parameters of printed coils have been discussed, dictating the design of the printed coil.

Based on the theory, the printed coils and circuits have been analysed to provide the desired electrical characteristics to meet the requirements of the application. The substrates and pastes have been selected for the screen printed coils. In the practical printing work, attempts have been made to print on the ceramic to test the profile of the coils, on the Kapton to test the flexibility of the coils, and on the interface-coated textile to achieve the final goal of this work. Paste Fabink-UV-IF1 has been selected for the interface layer and dielectric layer, Fabink-TC-AG4002 has been selected for conductive layer. The appropriate curing duration for the conductive layer in this work has been investigated, and then the issues of air bubbles caused by incomplete curing have been resolved, a 40 minutes at 130 °C curing process has been selected for a 150 mm × 150 mm printed coil conductive layer, which minimises the DC resistance and avoids increases due to over curing. The coils have been printed on the selected substrates and then the electrical characteristics have been measured and compared with the theoretical calculations. A flexible coil with 3.9 ± 8% µH inductance has been printed on the interface-coated textile, which has a 51 of unloaded Q factor. The resistance of printed coils is relatively high because of the high sheet resistivity of printable conductive paste, while the functionality of printed flexible coils in the WPT system has been verified by deployed them in Qi standard driver and receiver circuits.

A 1.5 W DC power output has been achieved when the flexible coils are centre aligned and kept flat, and the system can deliver at least 1 W DC power when the coils are deformed at a range of curvature including legs sizes of 90% of people in the UK. The comparison of the DC to DC transfer efficiency of the WPT system with different types of coupled coils has shown the limitations of the printed flexible coils, which perform at a maximum of 38% efficiency when the coupled coils keep flat and approximately 30% when they are deformed. The investigation of power consumptions in the WPT system with printed flexible coils shows that the resistances and parasitic capacitance of the printed coils implement the loss of power in the inductive coupled link. A journal paper on smart textile based flexible coils for wireless inductive power transmission has been submitted.

The DC to DC efficiency can be improved by employing flexible coils with higher unloaded Q factor. Future work can achieve a wireless power supply with either energy harvesting or flexible WPT system for an AAL system. The list below gives further details on the deliverables of focus for related research:

- A printable solar energy harvester which can be easily deployed on any surface. The solar energy is remarkable in the building environment compared with other ambient sources, but the solar cell, as the energy harvester, has the limitation on the deployment upon its characteristics. A printable solar cell could achieve the target of easy deployment and advantage the potential applications.
- A TX coil array with an active control system for improving the efficiency of the WPT when lateral misalignment occurred. The main work in this thesis on the printed coil is to improve the unloaded Q factor, hence to improve the efficiency of the link. By increasing the coupling factor, the efficiency of the link can be also improved. One method to improve the coupling factor is preventing the lateral misalignment between coils. The TX coil array takes the advantage of the transmitter based on a non-wearable environment, such as a chair or a bed. The active control system with the monitoring for the array is required that only the best aligned TX coil in the array should be activated to limit the power consumption of the entire array.
- Flexible circuits printed on textiles for wearable WPT systems. In this thesis, the testing system is rigid PCBs and unable to integrated into the wearable application. Flexible circuits for the driver and receiver have the challenges on the impedance of the conductive tracks comparing with the printed flexible circuit for electrodes or other sensors. It is very important that avoiding large power consumptions on the driver and receiver circuit.
- The deployment of a TX coil or coil array on a chair and a RX coil on clothing. There are lots of different challenges in the deployment for an AAL application, such as the user experience, it is also very important to examine the flexibility of the WPT system in the application.

List of References

[1] THE WORLD BANK. *Population ages 65 and above (% of total)*. Available: data.worldbank.org/indicator/SP.POP.65UP.TO.ZS, Access date: 12/02/2015.

[2] E. Hoffmann and J. Nachtmann, "Old age, the need of long-term care and healthy life expectancy," *Ageing, Care Need and Quality of Life,* pp. 163-176, 2010.

[3] A. J. Jara, M. A. Zamora-Izquierdo, and A. F. Gomez-Skarmeta, "An Ambient Assisted Living System for Telemedicine with Detection of Symptoms," in *Bioinspired Applications in Artificial and Natural Computation*. vol. 5602, J. Mira, J. Ferrández, J. Álvarez, F. Paz, and F. J. Toledo, Eds., ed: Springer Berlin Heidelberg, 2009, pp. 75-84.

[4] A. Hristova, A. M. Bernardos, and J. R. Casar, "Context-aware services for ambient assisted living: A case-study," in *'08. First International Symposium on Applied Sciences on Biomedical and Communication Technologies. ISABEL* 2008, pp. 1-5.

[5] K. Fotopoulou and B. W. Flynn, "Wireless Power Transfer in Loosely Coupled Links: Coil Misalignment Model," *Magnetics, IEEE Transactions on,* vol. 47, pp. 416-430, 2011.

[6] N. Tesla, "World system of wireless transmission of energy," *Telegraph and Telephone Age,* vol. 20, pp. 457-460, 1927.

[7] O. H. Stielau and G. A. Covic, "Design of loosely coupled inductive power transfer systems," in *Power System Technology, 2000. Proceedings. PowerCon 2000. International Conference on*, 2000, pp. 85-90 vol.1.

[8] A. Kurs, A. Karalis, R. Moffatt, J. D. Joannopoulos, P. Fisher, and M. Soljacic, "Wireless power transfer via strongly coupled magnetic resonances," *Science,* vol. 317, pp. 83-6, Jul 6 2007.

[9] K. Y. Kim, *Wireless Power Transfer - Principles and Engineering Explorations*. Janeza Trdine 9, 51000 Rijeka, Croatia: InTech, 2012.

[10] Duracell Powermat. *Wireless Power World*. Available: www.duracellpowermat.com, Access date: 17/05/2013.

[11] J. Yoo, Y. Long, L. Seulki, K. Yongsang, and Y. Hoi-Jun, "A 5.2 mW Self-Configured Wearable Body Sensor Network Controller and a 12 µW Wirelessly Powered Sensor for a Continuous Health Monitoring System," *Solid-State Circuits, IEEE Journal of,* vol. 45, pp. 178-188, 2010.

[12] C. T. Wang, K. Y. Huang, D. T. W. Lin, W. C. Liao, H. W. Lin, and Y. C. Hu, "A flexible proximity sensor fully fabricated by inkjet printing," *Sensors,* vol. 10, pp. 5054-5062, 2010.

[13] S. K. Mahadeva, S. Yun, and J. Kim, "Flexible humidity and temperature sensor based on cellulose–polypyrrole nanocomposite," *Sensors and Actuators A: Physical,* vol. 165, pp. 194-199, 2011.

[14] J. Zapata, F. J. Fernández-Luque, and R. Ruiz, "Wireless Sensor Network for Ambient Assisted Living," in *Wireless Sensor Networks: Application - Centric Design*. vol. 8, G. V. Merrett and Y. K. Tan, Eds., ed: InTech, 2010.

[15] M. Ghassemian, S. F. Auckburaully, M. Pretorius, and D. Jai-Persad, "Remote Elderly Assisted Living System-A preliminary research, development and evaluation," in *2011 IEEE 22nd International Symposium on Personal Indoor and Mobile Radio Communications (PIMRC)*, 2011, pp. 2219-2223.

[16] M. Alwan, J. Leachtenauer, S. Dalal, D. Mack, S. Kell, B. Turner, and R. Felder, "Psychosocial Impact of Monitoring Technology in Assisted Living: A Pilot Study," in *Information and Communication Technologies, 2006. ICTTA '06. 2nd*, 2006, pp. 998-1002.

[17] Z. Feng, J. Jianxin, C. Songlin, and Z. Daqing, "A Case-Driven Ambient Intelligence System for Elderly in-Home Assistance Applications," *Systems, Man, and Cybernetics, Part C: Applications and Reviews, IEEE Transactions on,* vol. 41, pp. 179-189, 2011.

[18] M. Mulvenna, W. Carswell, P. McCullagh, J. C. Augusto, Z. Huiru, P. Jeffers, W. Haiying, and S. Martin, "Visualization of data for ambient assisted living services," *Communications Magazine, IEEE,* vol. 49, pp. 110-117, 2011.

[19] M. Alwan, S. Dalal, D. Mack, S. Kell, B. Turner, J. Leachtenauer, and R. Felder, "Impact of monitoring technology in assisted living: outcome pilot," *Information Technology in Biomedicine, IEEE Transactions on,* vol. 10, pp. 192-198, 2006.

[20] P. E. Ross, "Managing care through the air [remote health monitoring]," *Spectrum, IEEE,* vol. 41, pp. 26-31, 2004.

[21] J. Rowan and E. D. Mynatt, "Digital Family Portrait Field Trial: Support for Aging in Place," presented at the Proceedings of the SIGCHI Conference on Human Factors in Computing Systems, Portland, Oregon, USA, 2005.

[22] E. Lubrin, E. Lawrence, and K. F. Navarro, "MoteCare: an adaptive smart BAN health monitoring system," presented at the Proceedings of the 24th IASTED international conference on Biomedical engineering, Innsbruck, Austria, 2006.

[23] A. Hochgatterer, L. Roedl, A. Martinez, I. Etxeberria, E. Aldaz, B. Wockl, and J. Bund, "Requirements for a behaviour pattern based assistant for early detection and management of neurodegenerative diseases," in *2011 5th International Conference on Pervasive Computing Technologies for Healthcare (PervasiveHealth)*, 2011, pp. 346-353.

[24] S.-L. Hsu, N.-C. Tsai, and C.-C. Lin, "An innovative power regulation method applied for wireless magnetic-energy transportation," *Mechatronics,* vol. 23, pp. 289-296, 4// 2013.

[25] L. Gustafsson. *Ambient Assisted Living Joint Programme Catalogue of Projects*. Available: www.aal-europe.eu, Access date: 12/02/2015.

[26] G. Paul, F. Cao, R. Torah, K. Yang, S. Beeby, and M. Tudor, "A Smart Textile based Facial EMG and EOG Computer Interface," *Sensors Journal, IEEE,* vol. PP, pp. 393-400, 2013.

[27] A. I. Dounis and C. Caraiscos, "Advanced control systems engineering for energy and comfort management in a building environment—A review," *Renewable and Sustainable Energy Reviews,* vol. 13, pp. 1246-1261, 2009.

[28] T. R. Gentry, "Building Systems, Controls, and Automation," in *The Design and Construction of High Performance Homes: Buildings Envelopes, Renewable Energies and Integrated Practice*, F. Trubiano, Ed., ed: Routledge, 2011, p. 298.

[29] L. Jiang, G. Jiaqi, H. Qi, and H. Fei, "Space encoding based compressive multiple human tracking with distributed binary pyroelectric infrared sensor networks," in *2012 IEEE Conference on Multisensor Fusion and Integration for Intelligent Systems (MFI)*, 2012, pp. 180-185.

[30] C. Peter, G. Bieber, and B. Urban, "Affect- and behaviour-related assistance for families in the home environment," presented at the Proceedings of the 3rd International Conference on PErvasive Technologies Related to Assistive Environments, Samos, Greece, 2010.

[31] Honeywell. *Building Automation Systems Catalog*. Available: customer.honeywell.com/resources/techlit/TechLitDocuments/70-0000s/70-6927.pdf, Access date: 12/02/2015.

[32] M. A. Hanson, H. C. Powell, A. T. Barth, K. Ringgenberg, B. H. Calhoun, J. H. Aylor, and J. Lach, "Body Area Sensor Networks: Challenges and Opportunities," *Computer,* vol. 42, pp. 58-65, 2009.

[33] M. Chen, S. Gonzalez, A. Vasilakos, H. Cao, and V. M. Leung, "Body Area Networks: A Survey," *Mobile Networks and Applications,* vol. 16, pp. 171-193, 2011/04/01 2011.

[34] P. Calvert, D. Duggal, P. Patra, A. Agrawal, and A. Sawhney, "Conducting Polymer and Conducting Composite Strain Sensors on Textiles," *Molecular Crystals and Liquid Crystals,* vol. 484, pp. 291-302, 17/04 2008.

[35] S. Bielska, M. Sibinski, and A. Lukasik, "Polymer temperature sensor for textronic applications," *Materials Science and Engineering: B,* vol. 165, pp. 50-52, 2009.

[36] H. Jie, G. Yishuang, and K. Pahlavan, "Modeling indoor TOA ranging error for body mounted sensors," in *2012 IEEE 23rd International Symposium on Personal Indoor and Mobile Radio Communications (PIMRC)*, 2012, pp. 682-686.

[37] M. R. Yuce, "Recent wireless body sensors: Design and implementation," in *2013 IEEE MTT-S International Microwave Workshop Series on RF and Wireless Technologies for Biomedical and Healthcare Applications (IMWS-BIO)*, 2013.

[38] T. H. Kang, C. R. Merritt, E. Grant, B. Pourdeyhimi, and H. T. Nagle, "Nonwoven Fabric Active Electrodes for Biopotential Measurement During Normal Daily Activity," *Biomedical Engineering, IEEE Transactions on,* vol. 55, pp. 188-195, 2008.

[39] J. Rius, S. Manich, R. Rodríguez, and M. Ridao, "Electrical Characterization of Conductive Ink Layers on Textile Fabrics: Model and Experimental Results," *Universitat Politecnica de Catalunya,* 2007.

[40] P. K. Baheti and H. Garudadri, "An Ultra Low Power Pulse Oximeter Sensor Based on Compressed Sensing," in *Sixth International Workshop on Wearable and Implantable Body Sensor Networks, 2009. BSN 2009.* , 2009, pp. 144-148.

[41] D. C. Ng, C. Boyd, B. Shun, G. Felic, M. Halpern, and E. Skafidas, "High-Q flexible spiral inductive coils," in *Electromagnetic Compatibility Symposium - Melbourne (EMC Melbourne)*, 2010, pp. 1-4.

[42] P. Wojtczuk, A. Armitage, T. D. Binnie, and T. Chamberlain, "PIR sensor array for hand motion recognition," in *The Second International Conference on Sensor Device Technologies and Applications SENSORDEVICES*, 2011, pp. 99-102.

[43] A. Rahimi, O. Zorlu, A. Muhtaroglu, and H. Kulah, "Fully Self-Powered Electromagnetic Energy Harvesting System With Highly Efficient Dual Rail Output," *Sensors Journal, IEEE,* vol. 12, pp. 2287-2298, 2012.

[44] O. Omeni, A. Wong, A. J. Burdett, and C. Toumazou, "Energy Efficient Medium Access Protocol for Wireless Medical Body Area Sensor Networks," *Biomedical Circuits and Systems, IEEE Transactions on,* vol. 2, pp. 251-259, 2008.

[45] A. Cabuk, A. V. T. Do, B. Chirn Chye, Y. Kiat-Seng, and D. Manh Anh, "A fully integrated 2.4-GHz receiver in a 0.18-μm CMOS process for low-power body-area-network applications," in *Biomedical Circuits and Systems Conference, 2007. BIOCAS 2007. IEEE*, 2007, pp. 171-174.

[46] R. Chavez-Santiago, K. E. Nolan, O. Holland, L. De Nardis, J. M. Ferro, N. Barroca, L. M. Borges, F. J. Velez, V. Goncalves, and I. Balasingham, "Cognitive radio for medical body area networks using ultra wideband," *Wireless Communications, IEEE,* vol. 19, pp. 74-81, 2012.

[47] K. O'Brien, G. Scheible, and H. Gueldner, "Analysis of wireless power supplies for industrial automation systems," in *The 29th Annual Conference of the IEEE Industrial Electronics Society*, 2003, pp. 367-372 vol.1.

[48] T. A. Nguyen and M. Aiello, "Energy intelligent buildings based on user activity: A survey," *Energy and Buildings,* vol. 56, pp. 244-257, January 2013.

[49] F. M. Miezin, L. Maccotta, J. M. Ollinger, S. E. Petersen, and R. L. Buckner, "Characterizing the Hemodynamic Response: Effects of Presentation Rate, Sampling Procedure, and the Possibility of Ordering Brain Activity Based on Relative Timing," *NeuroImage,* vol. 11, pp. 735-759, 2000.

[50] Texas Instruments. *ez430-rf2500 Development Tool User's Guide*. Available: www.ti.com/lit/ug/slau227e/slau227e.pdf, Access date: 12/02/2015.

[51] S. P. Beeby and N. M. White, *Energy Harvesting for Autonomous Systems*: Artech House Publishers, 2010.

[52] L. Quartararo, K. W. Roth, D. Westphalen, and J. Brodrick, "Wireless systems for building controls," *Ashrae Journal,* vol. 47, pp. 66-67, Feb 2005.

[53] L. Galeottei, M. Paoletti, and C. Marchesi, "Development of a low cost wearable prototype for long-term vital signs monitoring based on embedded integrated wireless module," in *Computers in Cardiology*, 2008, pp. 905-908.

[54] R. Jafari, F. Dabiri, P. Brisk, and M. Sarrafzadeh, "Adaptive and fault tolerant medical vest for life-critical medical monitoring," presented at the Proceedings of the 2005 ACM symposium on Applied computing, Santa Fe, New Mexico, 2005.

[55] S. Roundy, D. Steingart, L. Frechette, P. Wright, and J. Rabaey, "Power sources for wireless sensor networks," in *Wireless Sensor Networks, Proceedings*. vol. 2920, H. Karl, A. Willig, and A. Wolisz, Eds., ed Berlin: Springer-Verlag Berlin, 2004, pp. 1-17.

[56] J. M. Rabaey, M. J. Ammer, J. L. da Silva, Jr., D. Patel, and S. Roundy, "PicoRadio supports ad hoc ultra-low power wireless networking," *Computer,* vol. 33, pp. 42-48, Jul 2000.

[57] G. Anastasi, M. Conti, M. Di Francesco, and A. Passarella, "Energy conservation in wireless sensor networks: A survey," *Ad Hoc Networks,* vol. 7, pp. 537-568, 2009.

[58] T. Cheng-Hung, B. Ying-Wen, W. Hao-Yuan, and L. Ming-Bo, "Design and implementation of a socket with low standby power," *Consumer Electronics, IEEE Transactions on,* vol. 55, pp. 1558-1565, 2009.

[59] R. K. Dokania, X. Y. Wang, S. G. Tallur, and A. B. Apsel, "A Low Power Impulse Radio Design for Body-Area-Networks," *Circuits and Systems I: Regular Papers, IEEE Transactions on,* vol. 58, pp. 1458-1469, 2011.

[60] N. E. Toit, "Modeling and design of a MEMS piezoelectric vibration energy harvester," Massachusetts Institute of Technology, 2005.

[61] J. A. Paradiso and T. Starner, "Energy scavenging for mobile and wireless electronics," *Pervasive Computing, IEEE,* vol. 4, pp. 18-27, 2005.

[62] J. W. Matiko, N. J. Grabham, S. P. Beeby, and M. J. Tudor, "Review of the application of energy harvesting in buildings," *Measurement Science and Technology,* vol. 25, p. 25, 2014.

[63] E. E. Richman. *Requirements for Lighting Levels*. Available: www.wbdg.org/pdfs/usace_lightinglevels.pdf, Access date: 12/02/2015.

[64] L. Halonen, E. Tetri, and P. Bhusal, *Guidebook on Energy Efficient Electric Lighting for Buildings*. Espoo, Finland: International Energy Agency, 2010.

[65] Y. K. Cheng and K. W. E. Cheng, "General Study for using LED to replace traditional lighting devices," in *ICPESA '06. 2nd International Conference on Power Electronics Systems and Applications*, 2006, pp. 173-177.

[66] B. Howard, S. Leitman, and W. Brinsky, *Green Lighting*. USA: McGraw-Hill Professional Publishing, 2012.

[67] M. A. Green, K. Emery, Y. Hishikawa, W. Warta, and E. D. Dunlop, "Solar Cell Efficiency Tables (version 39)," *Progress in Photovoltaics: Research and Applications,* vol. 20, pp. 12-20, 2012.

[68] Panasonic Eco Solutions Amorton Co. Ltd. *Amorphous Silicon Solar Cells / Amorphous Photosensors*. Available: us.sanyo.com/Dynamic/customPages/docs/solarPower_Amorphous_PV_Product_Brochure%20_EP120B.pdf, Access date: 12/02/2015.

[69] M. T. Penella and M. Gasulla, "A Review of Commercial Energy Harvesters for Autonomous Sensors," in *24th IEEE Instrumentation and Measurement Technology Conference*, Warsaw, Poland, 2007, pp. 1807-1811.

[70] R. Missaoui, G. Warkozek, S. Bacha, and S. Ploix, "PV integration by building Energy Management System," in *2011 International Conference on Power Engineering, Energy and Electrical Drives (POWERENG)*, 2011, pp. 1-8.

[71] EnOcean. *Self-powered Wireless Switches & Sensors and Controls*. Available: www.enocean.com/en/product-finder/, Access date: 12/02/2015.

[72] EnOcean. *Torre Espacio Madrid (Spain)*. Available: www.enocean.com/en/torre-espacio-madrid-spain/, Access date: 12/02/2015.

[73] D. Masotti, A. Costanzo, and S. Adami, "Design and realization of a wearable multi-frequency RF energy harvesting system," in *5th European Conference on Antennas and Propagation (EUCAP)*, 2011, pp. 517-520.

[74] Z. Fan, Z. Yanqing, J. Silver, Y. Shakhsheer, M. Nagaraju, A. Klinefelter, J. Pandey, J. Boley, E. Carlson, A. Shrivastava, B. Otis, and B. Calhoun, "A batteryless 19uW MICS/ISM-band energy harvesting body area sensor node SoC," in *2012 IEEE International Solid-State Circuits Conference Digest of Technical Papers (ISSCC)*, 2012, pp. 298-300.

[75] P. Rashidi and A. Mihailidis, "A survey on ambient-assisted living tools for older adults," *IEEE journal of biomedical and health informatics,* vol. 17, pp. 579-590, 2013.

[76] L. Xun, W. M. Ng, C. K. Lee, and S. Y. Hui, "Optimal operation of contactless transformers with resonance in secondary circuits," in *Twenty-Third Annual IEEE Applied Power Electronics Conference and Exposition*, 2008, pp. 645-650.

[77] C. Byungcho, N. Jaehyun, C. Honnyong, A. Taeyoung, and C. Seungwon, "Design and implementation of low-profile contactless battery charger using planar printed circuit board windings as energy transfer device," *Industrial Electronics, IEEE Transactions on,* vol. 51, pp. 140-147, 2004.

[78] T. Bieler, M. Perrottet, V. Nguyen, and Y. Perriard, "Contactless power and information transmission," *Industry Applications, IEEE Transactions on,* vol. 38, pp. 1266-1272, 2002.

[79] A. T. Barker, "Applied Bioelectricity: from Electrical Stimulation to Electropathology," *Physiological Measurement,* vol. 20, p. 215, 1999.

[80] K. Jingook and F. Bien, "Electric field coupling technique of wireless power transfer for electric vehicles," in *2013 IEEE TENCON Spring Conference*, 2013, pp. 267-271.

[81] M. Kline, I. Izyumin, B. Boser, and S. Sanders, "Capacitive power transfer for contactless charging," in *2011 Twenty-Sixth Annual IEEE Applied Power Electronics Conference and Exposition (APEC)*, 2011, pp. 1398-1404.

[82] G. Yilmaz and C. Dehollain, "An efficient wireless power link for implanted biomedical devices via resonant inductive coupling," in *2012 IEEE Radio and Wireless Symposium (RWS)*, 2012, pp. 235-238.

[83] S. Bhuyan, S. K. Panda, K. Sivanand, and R. Kumar, "A compact resonace-based wireless energy transfer system for implanted electronic devices," in *2011 International Conference on Energy, Automation, and Signal (ICEAS)*, 2011, pp. 1-3.

[84] K. Sohee, R. R. Harrison, and F. Solzbacher, "Influence of System Integration and Packaging on Its Inductive Power Link for an Integrated Wireless Neural Interface," *Biomedical Engineering, IEEE Transactions on,* vol. 56, pp. 2927-2936, 2009.

[85] W. Wei and F. Qiang, "Design and simulation of printed spiral coil used in wireless power transmission systems for implant medical devices," in *2011 Annual International Conference of the IEEE Engineering in Medicine and Biology Society*, 2011, pp. 4018-4021.

[86] R. Wu, S. Raju, C. Mansun, J. K. O. Sin, and C. P. Yue, "Wireless power link design using silicon-embedded inductors for brain-machine interface," in *2012 International Symposium on VLSI Design, Automation, and Test (VLSI-DAT)*, 2012, pp. 1-4.

[87] Y. Xuehong, F. Herrault, J. Chang-Hyeon, K. Seong-Hyok, M. G. Allen, G. Lisi, N. Luu, and D. I. Anderson, "Watt-level wireless power transfer based on stacked flex circuit technology," in *Electronic Components and Technology Conference (ECTC), 2011 IEEE 61st*, 2011, pp. 2185-2191.

[88] Z. N. Low, R. A. Chinga, R. Tseng, and L. Jenshan, "Design and Test of a High-Power High-Efficiency Loosely Coupled Planar Wireless Power Transfer System," *Industrial Electronics, IEEE Transactions on,* vol. 56, pp. 1801-1812, 2009.

[89] WiTricity Corporation. *Witricity Technology: The Basics*. Available: www.radford.edu/nsrl/creu1011/PowerPoints/KhamphavongPowerPoint1.pdf, Access date: 12/02/2015.

[90] T. Instruments. *bqTESLA Portfolio of Wireless Power Solutions*. Available: www.ti.com/lit/ml/slpt021a/slpt021a.pdf, Access date: 15/06/2015.

[91] M. Kesler. *Highly Resonant Wireless Power Transfer: Safe, Efficient, and over Distance*. Available: www.witricity.com/assets/highly-resonant-power-transfer-kesler-witricity-2013.pdf, Access date: 14/12/2014/2013.

[92] W. Chwei-Sen, G. A. Covic, and O. H. Stielau, "Power transfer capability and bifurcation phenomena of loosely coupled inductive power transfer systems," *Industrial Electronics, IEEE Transactions on,* vol. 51, pp. 148-157, 2004.

[93] X. W. Chen, Z. H. Wu, M. J. Zhao, and B. Li, "An adaptive feedback for implantable wireless power transmission system," in *2013 IEEE International Conference of Electron Devices and Solid-State Circuits (EDSSC)*, 2013, pp. 1-2.

[94] HSAS. *Electromagnetic Fields Directive and the AURPO Guidance*. Access date: 16/06/2014.

[95] HM Government, "Government response to the Stakeholder Advisory Group on extremely low frequency electric and magnetic fields recommendations." Available: www.gov.uk/government/uploads/system/uploads/attachment_data/file/215380/dh_130702.pdf, 2015.

[96] R. Matthes, J. H. Bernhardt, and A. F. McKinlay, *A Guidelines on Limiting Exposure to Non-ionizing Radiation*. Munich: International Commission on Non-Ionizing Radiation Protection, 1999.

[97] European Parliament, "Directive of The European Parliament and of the Council on the minimum health and safety requirements regarding the exposure of workers to the risks arising from physical agents," European Commission, Brussels. Available: ec.europa.eu/commission_2010-2014, 2011.

[98] "IEEE Standard for Safety Levels With Respect to Human Exposure to Radio Frequency Electromagnetic Fields, 3 kHz to 300 GHz," *IEEE Std C95.1-2005 (Revision of IEEE Std C95.1-1991),* pp. 0_1-238, 2006.

[99] D. E. Hintenlang, "Synergistic effects of ionizing radiation and 60 Hz magnetic fields," *Bioelectromagnetics,* vol. 14, pp. 545-551, 1993.

[100] M. de Rooij and J. Strydom. (2012, 6/27/2012) eGaN® FET-Silicon Shoot-Out Vol. 9: Wireless Power Converters. *Power Electronics Technology*. 3-8.

[101] Qi Wireless Power Consortium. *Qi Low Power Specifications*. Available: www.wirelesspowerconsortium.com/developers/specification.html, Access date: 12/02/2015.

[102] W. Lihsien, Y. Zhi, E. Basham, and L. Wentai, "An efficient wireless power link for high voltage retinal implant," in *Biomedical Circuits and Systems Conference,*, 2008, pp. 101-104.

[103] W. G. Hurley, W. H. Wolfle, and J. G. Breslin, "Optimized transformer design: inclusive of high-frequency effects," *Power Electronics, IEEE Transactions on,* vol. 13, pp. 651-659, 1998.

[104] M. K. Kazimierczuk and D. Czarkowski, *Resonant power converters*: John Wiley & Sons, 2012.

[105] Z. Kaczmarczyk, "A high-efficiency Class E inverter–computer model, laboratory measurements and SPICE simulation," *Bulletin of the Polish Academy of Sciences: Technical Sciences,* vol. 55, 2007.

[106] N. O. Sokal and A. D. Sokal, "Class E-A new class of high-efficiency tuned single-ended switching power amplifiers," *Solid-State Circuits, IEEE Journal of,* vol. 10, pp. 168-176, 1975.

[107] M. K. Kazimierczuk and D. Czarkowski, *Resonant Power Converters, Solutions Manual*: Wiley-Interscience, 1995.

[108] B. Gu, J. Dominic, J. Lai, C. Chen, T. LaBella, and B. Chen, "High Reliability and Efficiency Single-Phase Transformerless Inverter for Grid-Connected Photovoltaic Systems," *Power Electronics, IEEE Transactions on,* vol. 28, pp. 2235-2245, 2013.

[109] M. Pinuela, D. C. Yates, S. Lucyszyn, and P. D. Mitcheson, "Maximizing DC-to-Load Efficiency for Inductive Power Transfer," *Power Electronics, IEEE Transactions on,* vol. 28, pp. 2437-2447, 2013.

[110] A. Grebennikov, "Load network design techniques for class E RF and microwave amplifiers," *High Frequency Electronics,* vol. 3, pp. 18-32, 2004.

[111] J. R. Warren, K. A. Rosowski, and D. J. Perreault, "Transistor Selection and Design of a VHF DC-DC Power Converter," *Power Electronics, IEEE Transactions on,* vol. 23, pp. 27-37, 2008.

[112] R. Senani, "Realization of a Class Of Analog Signal Processing / Signal Generation Circuits: Novel Configurations Using Current Feedback Op-Amps," *Frequenz,* vol. 52, pp. 196-206, September 1998.

[113] C. Peters, D. Spreemann, M. Ortmanns, and Y. Manoli, "A CMOS integrated voltage and power efficient AC/DC converter for energy harvesting applications," *Journal of Micromechanics and Microengineering,* vol. 18, p. 104005, 2008.

[114] B. Lenaerts and R. Puers, "Automatic inductance compensation for class E driven flexible coils," *Sensors and Actuators A: Physical,* vol. 145–146, pp. 154-160, 2008.

[115] H. Hyeonseok, M. Junil, L. Bumsoo, J. Chan-hui, and K. Soo-won, "An analysis of magnetic resonance coupling effects on wireless power transfer by coil inductance and placement," *Consumer Electronics, IEEE Transactions on,* vol. 60, pp. 203-209, 2014.

[116] S. Jung, C. Lauterbach, M. Strasser, and W. Weber, "Enabling technologies for disappearing electronics in smart textiles," in *2003 IEEE International Solid-State Circuits Conference*, 2003, pp. 386-387 vol.1.

[117] D. Zhu, P. Glenne-Jones, N. M. White, N. Harris, M. J. Tudor, R. N. Torah, A. Almusallam, and S. P. Beeby, "Screen printed piezoelectric films for energy harvesting," 2012.

[118] B. H. Waters, B. J. Mahoney, L. Gunbok, and J. R. Smith, "Optimal coil size ratios for wireless power transfer applications," in *2014 IEEE International Symposium on Circuits and Systems (ISCAS)*, 2014, pp. 2045-2048.

[119] M. Zolog, D. Pitica, and O. Pop, "Characterization of Spiral Planar Inductors Built on Printed Circuit Boards," in *30th International Spring Seminar on Electronics Technology*, 2007, pp. 308-313.

[120] WIRELESS POWER CONSORTIUM. *Wireless Power Specification*. Available: www.wirelesspowerconsortium.com/downloads/wireless-power-specification-part-1.html, Access date: 06/06/2015.

[121] R. Paradiso and D. De Rossi, "Advances in textile sensing and actuation for e-textile applications," in *30th Annual International Conference of the IEEE Engineering in Medicine and Biology Society*, 2008, pp. 3629-3629.

[122] J. J. Liu, M. C. Huang, W. Xu, X. Zhang, L. Stevens, N. Alshurafa, and M. Sarrafzadeh, "BreathSens: A Continuous On-Bed Respiratory Monitoring System with Torso Localization using an Unobtrusive Pressure Sensing Array," *Biomedical and Health Informatics, IEEE Journal of,* vol. PP, pp. 1-1, 2014.

[123] G. Valenza, L. Citi, C. Gentili, A. Lanata, E. P. Scilingo, and R. Barbieri, "Characterization of Depressive States in Bipolar Patients Using Wearable Textile Technology and Instantaneous Heart Rate Variability Assessment," *Biomedical and Health Informatics, IEEE Journal of,* vol. 19, pp. 263-274, 2015.

[124] C. Kallmayer and E. Simon, "Large area sensor integration in textiles," in *2012 9th International Multi-Conference on Systems, Signals and Devices (SSD)*, 2012, pp. 1-5.

[125] P. J. Holmes and R. G. Loasby, *Handbook of thick film technology*: Electrochemical Publications, 1976.

[126] C. Jung-Chuan, T. Ya-Li, C. Tsung-Yi, L. Yi-Hung, Y. Guan-Chen, and Y. Shu-Ying, "Fabrication of Arrayed Flexible Screen-Printed Glucose Biosensor Based on Microfluidic Framework," *Sensors Journal, IEEE,* vol. 14, pp. 178-183, 2014.

[127] K. J. Noh, Y. K. Son, B. S. Kim, and I. Cho, "Wearable network using Optical e-Textile Antenna for NLOS," in *2012 IEEE International Conference on Consumer Electronics (ICCE)*, 2012, pp. 556-557.

[128] DuPont. *DuPont 5000 Silver Conductor Datasheet*. Available: www2.dupont.com/MCM/en_US/assets/downloads/prodinfo/5000.pdf, Access date: 12/02/2015.

[129] Smart Fabric Inks Ltd. *Conductive pastes for use on textiles: Fabink-TC-AG4002 Datasheet*. Available: www.fabinks.com, Access date: 12/02/2015.

[130] DuPont. *DuPont 5018 UV Curable Dielectric Datasheet*. Available: www2.dupont.com/MCM/en_US/assets/downloads/prodinfo/5018.pdf, Access date: 12/02/2015.

[131] J. Pan, G. L. Tonkay, and A. Quintero, "Screen Printing Process Design of Experiments for Fine Line Printing of Thick Film Ceramic Substrates," *Journal of Electronics Manufacturing,* vol. 09, pp. 203-213, 1999.

[132] S. Sepeur, N. Kunze, B. Werner, and H. Schmidt, "UV curable hard coatings on plastics," *Thin Solid Films,* vol. 351, pp. 216-219, 1999.

[133] P. Lennie, J. Pokorny, and V. C. Smith, "Luminance," *J. Opt. Soc. Am. A,* vol. 10, pp. 1283-1293, 06/01 1993.

[134] G24i. *Dye Sensitised Indoor Photovoltaic Module*. Available: datasheet.eeworld.com.cn/pdf/G24I/375497_INDY4050.pdf, Access date: 12/02/2015.

[135] National Center for Photovoltaics. *Best Research-Cell Efficiencies (Rev. 08-2013)*. Available: www.nrel.gov/ncpv/images/efficiency_chart.jpg, Access date: 12/02/2015.

[136] G24 Innovations. *Indy4100 Datasheet*. Available: pdf1.alldatasheet.com/datasheet-pdf/view/418513/G24I/INDY4100/+31J535VEJ-pbKRHdzNNY+/datasheet.pdf, Access date: 18/02/2010.

[137] V. Salas, E. Olías, A. Barrado, and A. Lázaro, "Review of the Maximum Power Point Tracking Algorithms for Stand-alone Photovoltaic Systems," *Solar Energy Materials and Solar Cells,* vol. 90, pp. 1555-1578, 2006.

[138] N. Van Helleputte, J. M. Tomasik, W. Galjan, A. Mora-Sanchez, D. Schroeder, W. H. Krautschneider, and R. Puers, "A flexible system-on-chip (SoC) for biomedical signal acquisition and processing," *Sensors and Actuators A: Physical,* vol. 142, pp. 361-368, 2008.

[139] Texas Instruments. *CC2500 Datasheet*. Available: www.ti.com/lit/ds/symlink/cc2500.pdf, Access date: 12/02/2015.

[140] Texas Instruments. *CC2430 Datasheet*. Available: www.ti.com/lit/ds/symlink/cc2430.pdf, Access date: 12/02/2015.

[141] Microchip Technology Inc. *MRF24J40MC Datasheet*. Available: ww1.microchip.com/downloads/en/DeviceDoc/75002A.pdf, Access date: 12/02/2015.

[142] ATMEL. *AT86RF231 Datasheet*. Available: www.atmel.com/Images/doc8111.pdf, Access date: 12/02/2015.

[143] ATMEL. *ATmega128RFA1 Datasheet*. Available: www.atmel.com/Images/Atmel-8266-MCU_Wireless-ATmega128RFA1_Datasheet.pdf, Access date: 12/02/2015.

[144] O. Songhwai, L. Schenato, P. Chen, and S. Sastry, "Tracking and Coordination of Multiple Agents Using Sensor Networks: System Design, Algorithms and Experiments," *Proceedings of the IEEE,* vol. 95, pp. 234-254, 2007.

[145] Texas Instruments. *TPS61221 Datasheet*. Available: www.ti.com/lit/ds/symlink/tps61220.pdf, Access date: 12/02/2015.

[146] T. Markvart and L. Castaņer, *Practical handbook of photovoltaics: fundamentals and applications*: Elsevier Science, 2003.

[147] H. A. Haus and W. Huang, "Coupled-mode theory," *Proceedings of the IEEE,* vol. 79, pp. 1505-1518, 1991.

[148] W. Ko, S. Liang, and C. Fung, "Design of radio-frequency powered coils for implant instruments," *Medical and Biological Engineering and Computing,* vol. 15, pp. 634-640, 1977.

[149] M. Ghovanloo and G. Lazzi, "Transcutaneous Magnetic Coupling of Power and Data," in *Wiley Encyclopedia of Biomedical Engineering*, ed: John Wiley & Sons, Inc., 2006.

[150] L. Green. *RF-inductor modeling for the 21st century*. Available: m.eet.com/media/1142818/19256-159688.pdf, Access date: 12/02/2015.

[151] F. E. Terman, *Radio engineers' handbook* vol. 2: McGraw-Hill New York, 1943.

[152] C. S. Walker, *Capacitance, inductance, and crosstalk analysis*: Artech House, 1990.

[153] C. M. Zierhofer and E. S. Hochmair, "Geometric approach for coupling enhancement of magnetically coupled coils," *Biomedical Engineering, IEEE Transactions on,* vol. 43, pp. 708-714, 1996.

[154] H. Nagaoka, "The inductance coefficients of solenoids," *Journal of the College of Science,* vol. 27, pp. 18-33, 1909.

[155] N. Vittal, R. C. Aiyer, C. R. Aiyer, M. S. Setty, and S. D. Phadke R.N, "Formulation of silver loaded manganite based thermistor paste and application of percolation theory for sudden transition in conductance," *Journal of Applied Physics,* vol. 64, pp. 5244-5247, 1988.

[156] M. Greconici, G. Madescu, and M. Mot, "Skin effect analysis in a free space conductor," vol. 23, p. 215, 2010.

[157] Z. Song, W. Yahyaoui, F. Duval, D. Su, and A. Louis, "Capturing skin effect with an effective nonuniform mesh and coupled R-L circuits," *Electronics Letters,* vol. 47, pp. 94-95, 2011.

[158] W. B. Kuhn and N. M. Ibrahim, "Analysis of current crowding effects in multiturn spiral inductors," *Microwave Theory and Techniques, IEEE Transactions on,* vol. 49, pp. 31-38, 2001.

[159] E. Ashoori, F. Asgarian, A. M. Sodagar, and Y. Euisik, "Design of double layer printed spiral coils for wirelessly-powered biomedical implants," in *Engineering in Medicine and Biology Society,EMBC, 2011 Annual International Conference of the IEEE*, 2011, pp. 2882-2885.

[160] L. Jianyu, T. Houjun, and G. Xin, "Frequency Splitting Analysis of Wireless Power Transfer System Based on T-type Transformer Model," *Electronics and Electrical Engineering,* vol. 19, pp. 109-113, 2013.

[161] U. M. Jow and M. Ghovanloo, "Modeling and Optimization of Printed Spiral Coils in Air, Saline, and Muscle Tissue Environments," *Biomedical Circuits and Systems, IEEE Transactions on,* vol. 3, pp. 339-347, 2009.

[162] S. Gevorgian, H. Berg, H. Jacobsson, and T. Lewin, "Application notes - basic parameters of coplanar-strip waveguides on multilayer dielectric/semiconductor substrates, Part 1: high permittivity superstrates," *Microwave Magazine, IEEE,* vol. 4, pp. 60-70, 2003.

[163] M. Schroeder, S. Anupama, and R. Nelson, "An analysis on the role of water content and state on effective permittivity using mixing formulas," *Journal of Biomechanics, Biomdical, and Biophysical Engineering,* vol. 2, pp. 193-204, 2008.

[164] S. Musunuri and P. L. Chapman, "Multi-layer spiral inductor design for monolithic DC-DC converters," in *38th IAS Annual Meeting, Industry Applications Conference*, 2003, pp. 1270-1275 vol.2.

[165] F. A. Kolster, "The Effects of Distributed Capacity of Coils Used in Radio-Telegraphic Circuits," *Proceedings of the Institute of Radio Engineers,* vol. 1, pp. 19-27, 1913.

[166] J. A. Stratton, *Electromagnetic theory* vol. 33: John Wiley & Sons, 2007.

[167] M. Kiani, U. M. Jow, and M. Ghovanloo, "Design and Optimization of a 3-Coil Inductive Link for Efficient Wireless Power Transmission," *Biomedical Circuits and Systems, IEEE Transactions on,* vol. 5, pp. 579-591, 2011.

[168] Y. P. Su, L. Xun, and S. Y. R. Hui, "Mutual Inductance Calculation of Movable Planar Coils on Parallel Surfaces," *Power Electronics, IEEE Transactions on,* vol. 24, pp. 1115-1123, 2009.

[169] S. Atluri and M. Ghovanloo, "Design of a Wideband Power-Efficient Inductive Wireless Link for Implantable Biomedical Devices Using Multiple Carriers," in *2nd International IEEE EMBS Conference on Neural Engineering, 2005.*, 2005, pp. 533-537.

[170] K. Finkenzeller, *RFID Handbook: Fundamentals and Applications in Contactless Smart Cards and Identification*: Wiley, 2003.

[171] R. F. Xue, K. W. Cheng, and M. Je, "High-Efficiency Wireless Power Transfer for Biomedical Implants by Optimal Resonant Load Transformation," *Circuits and Systems I: Regular Papers, IEEE Transactions on,* vol. 60, pp. 867-874, 2013.

[172] G. Paul, T. Russel, Y. Kai, B. Steve, and T. John, "An investigation into the durability of screen-printed conductive tracks on textiles," *Measurement Science and Technology,* vol. 25, p. 025006, 2014.

[173] Y. M. Chow, W. M. Lau, R. E. Schetty, and Z. S. Karim, "Feasibility and reliability study on the electroless nickel bumping and stencil solder printing for low-cost flip chip electronic packaging," in *International Symposium on Electronic Materials and Packaging, 2000. (EMAP 2000).* , 2000, pp. 79-85.

[174] S. K. So, W. K. Choi, C. H. Cheng, L. M. Leung, and C. F. Kwong, "Surface preparation and characterization of indium tin oxide substrates for organic electroluminescent devices," *Applied Physics A,* vol. 68, pp. 447-450, 1999/04/01 1999.

[175] DuPont. *Kapton polyimide film*. Available: www.dupont.com/content/dam/assets/products-and-services/membranes-films/assets/DEC-Kapton-HN-datasheet.pdf, Access date: 12/02/2015.

[176] Y. Li, R. Torah, S. Beeby, and J. Tudor, "Inkjet printed flexible antenna on textile for wearable applications," 2012.

[177] B. Karaguzel, C. Merritt, T. Kang, J. Wilson, P. Franzon, H. Nagle, E. Grant, and B. Pourdeyhimi, "Using conductive inks and non-woven textiles for wearable computing," in *the 2005 Textile Institute Worlsd Conference*, 2005.

[178] L. Yi, R. Torah, S. Beeby, and J. Tudor, "An all-inkjet printed flexible capacitor for wearable applications," in *2012 Symposium on Design, Test, Integration and Packaging of MEMS/MOEMS (DTIP)*, 2012, pp. 192-195.

[179] Y. Wei, R. Torah, S. Beeby, and J. Tudor, "Screen printed capacitive free-standing cantilever beams used as a motion detector for wearable sensors," *Procedia Engineering,* vol. 47, pp. 465-469, 2012.

[180] Smart Fabric Inks Ltd. *Smooth interface layer paste for printing on fabrics*. Available: www.fabinks.com, Access date: 12/02/2015.

[181] J. Panero and M. Zelnik, *Human dimension and interior space: a source book of design reference standards*: Random House LLC, 2014.

[182] A. O. Komolafe, R. Torah, K. Yang, J. Tudor, and S. P. Beeby, "Durability of screen printed electrical interconnections on woven textiles," presented at the Electronic Components and Technology Conference (ECTC), 2015 IEEE 65th, CA, USA, 2015.

[183] G. L. Skibinski, R. J. Kerkman, and D. Schlegel, "EMI emissions of modern PWM AC drives," *Industry Applications Magazine, IEEE,* vol. 5, pp. 47-80, 1999.

[184] SAGAMI ELEC. *Tips for Coil Users*. Available: www.sagami-elec.co.jp/file/tech/coil_doc_06e.pdf, Access date: 12/02/2015.

[185] S. Y. R. Hui, Z. Wenxing, and C. K. Lee, "A Critical Review of Recent Progress in Mid-Range Wireless Power Transfer," *Power Electronics, IEEE Transactions on,* vol. 29, pp. 4500-4511, 2014.

[186] Texas Instruments. *bq500211 bqTESLA Wireless Power TX EVM*. Available: www.ti.com/lit/ug/slvu536a/slvu536a.pdf, Access date: 17/08/2013.

[187] Texas Instruments. *bq51013AEVM-765 Evaluation Module*. Available: www.ti.com/lit/ug/sluu911a/sluu911a.pdf, Access date: 17/08/2013.

[188] Tektronix. *Passive Voltage Probes P6139A Datasheet*. Available: datasheet.octopart.com/P6136-Tektronix-datasheet-43440.pdf, Access date: 10/02/2015.

[189] G. Skutt, F. C. Lee, R. Ridley, and D. Nicol, "Leakage inductance and termination effects in a high-power planar magnetic structure," in *Ninth Annual Applied Power Electronics Conference and Exposition*, 1994, pp. 295-301 vol.1.

[190] B. Bogin and M. I. Varela-Silva, "Leg length, body proportion, and health: a review with a note on beauty," *International journal of environmental research and public health,* vol. 7, pp. 1047-1075, 2010.